THE β SPECTRUM FOLLOWING FISSION FROM ^{252}Cf

Thesis by

David Lee Wark

In Partial Fulfillment of the Requirements

for the Degree of

Doctor of Philosophy

California Institute of Technology

Pasadena, California

1987

(Submitted January 23, 1987)

To Mom and Dad

ACKNOWLEDGEMENTS

I would like to thank my advisor, Prof. Felix Boehm, for his support over the last five years. His confidence and patience, especially during the trying times of candidacy exams, are greatly appreciated. I would like to thank Jordan Camp for his endless work on our experiments, I have never found anyone with whom I could work as closely or for as long and still remain good friends. I would like to thank Dr. Petr Vogel for his help on the calculations in this thesis and for his many helpful comments on the rest of the work. I am also indebted to my "advisor" at ANL, Dr. Gerry Garvey, for his hard work and quick insight.

I gratefully acknowledge the help of the other members of Physics 34, especially Elsa Garcia (for her help shielding me from the hideous paperwork of travel) and Herb Hendrickson (for his sage advice along the way). There were many people at ANL who helped with this thesis, I would especially like to mention the contributions of Stuart Freedman, Jim Napolitano, Jim Nelson, and Boze Orzula. Last but not least, I would like to thank all my friends and housemates, especially Mark Muldoon and Geoff Blewitt, for making the last five years the most enjoyable of my life.

ABSTRACT

The β spectrum from the fission products of ^{252}Cf has been measured using a flat-field magnetic spectrometer. The active entrance aperture to the magnetic field region consisted of an annular plastic scintillator to veto slit scattering and a thin wire chamber to signal electrons on a good trajectory. The electrons exited the magnetic field through a position sensitive wire chamber capable of three dimensional track reconstruction. The energy calibration and relative efficiency of the spectrometer were determined using the β decays of ^{12}B, ^{20}F, and ^{90}Sr. The shape of the β spectrum from ^{252}Cf was measured at 5 field settings and the results combined to form a complete spectrum from 2.0 to 9.0 MeV (β total energy) with a total error of 3% at 3 MeV, rising to 6% at 5 MeV, 9% at 7 MeV, 15% at 8 MeV and 25% at 9 MeV. This experiment was motivated by the need to know the $\overline{\nu}_e$ spectrum from the β decays of fission products in order to interpret the results of reactor based neutrino oscillation experiments. The $\overline{\nu}_e$ spectrum can be calculated directly or converted from a measured β spectrum. This experiment is an additional check of these calculations and constitutes a complementary check of previous measurements of the β spectrum from other fissioning nuclei ^{235}U, ^{239}Pu, and ^{241}Pu. We find a softer spectrum (fewer β's at high momenta) than predicted by the calculations, in agreement with earlier measurements in other nuclei by Schreckenbach et al., but in disagreement with earlier measurements by Borovoi et al. in ^{252}Cf. Possible sources of the disagreement with the calculations and the earlier experiment and possible improvements to the experiment are discussed.

CONTENTS

CHAPTER 1

INTRODUCTION

1.1 OVERVIEW

This thesis is concerned with an experimental study of the β spectrum from the fission products of ^{252}Cf (hereafter abbreviated as 'the ^{252}Cf spectrum'). This work is motivated by the vital role that post-fission neutrino spectra play in the interpretation of reactor-based neutrino oscillation experiments. Chapter 1 will therefore be a short introduction to neutrino oscillations, including a summary of the current experiments and the role of post-fission β and ν spectra and their interpretation. Chapter 2 will look at the 180° flat-field β spectrograph constructed at the Argonne National Laboratory to measure the ^{252}Cf spectrum and the β spectra of ^{12}B, ^{20}F, and ^{90}Sr. Chapter 3 covers the data analysis and results, and Chapter 4 contains a comparison of the results of this work to earlier work and the conclusions.

A complete study of the theory and phenomenology of neutrino oscillations is beyond the scope of this thesis. We will therefore consider only the very basics needed to discuss the results. Several reviews of the subject can be found in references 1-5. This chapter is based on these papers, particularly the paper by Frampton and Vogel.[1] We also mention the comprehensive overview of the current understanding of electroweak interactions found in Fritzsch and Minkowski[6].

1.2 BEYOND THE STANDARD MODEL

In the Standard Model of electroweak interactions neutrinos are massless Dirac particles. (Dirac particles, as opposed to Majorana particles, are described by spinors with four independent components, i.e., particle and anti-particle are distinct. In the case of Majorana particles this distinction is not made, i.e., $\nu_R = \overline{\nu_L}$ where L,R are helicity states, and the spinor has only two independent components.) The left-handed helicity states of the neutrino and the charged lepton of the same flavor form a weak isospin doublet, and the right-handed component of the charged lepton forms a singlet. Neutrino couplings are therefore purely left-handed, and since helicity is conserved for a massless particle right-handed neutrinos are entirely absent. In this model additive lepton numbers assigned to each flavor are independently conserved.

While this model has had great success in explaining many phenomena seen in experiments, there are many reasons to believe that it is not the most fundamental theory of the interactions of leptons. The chiral nature of the theory is added in a purely ad hoc manner, and no reason is given for the existence of different families. The lepton masses are not predicted, nor is the mass of the Higgs boson. Also, of course, there is the on-going effort to unify the electroweak interaction with the strong and gravitational forces. These Grand Unified Theories (GUTs) generally predict different properties for the neutrino than the ones listed above, including in most cases a non-zero Majorana rest mass. Majorana mass terms are attractive because they can explain the large difference in masses between charged and neutral leptons (charged leptons cannot have Majorana masses without violating charge conservation, thus the mass terms would have to arise from different sources), and because such terms arise naturally in these theories. For example, one such GUT based on the group O(10) predicts a Majorana mass of order 10 eV for the heaviest neutrino[1]. One exception to this is the minimal SU(5) theory, which predicts $m_\nu = 0$.

However, the lifetime for proton decay predicted by this theory seems to be too short by at least an order of magnitude compared with the current experimental limit[7], casting doubt on its other predictions as well. Superstring theories also predict $m_\nu \neq 0$, although quantitative predictions are difficult to make.

There are also indications from astrophysics that the Standard Model is incomplete. Observations of the radial velocity profile in galaxies indicate that the visible mass accounts for only about 10 percent of the total mass present. Observations of clusters of galaxies give an even larger fraction for dark matter[8]. Likewise, the observed density of baryonic matter in the universe accounts for only about one-tenth of the closure density. There are various theoretical reasons for believing that $\Omega = \rho_{univ} / \rho_c = 1$. Thus, up to 90 percent of the mass in the universe might be present in non-luminous form. While there is no compelling reasons to believe that neutrinos make up this missing mass, estimates of the number density of neutrinos left over from the big bang combined with the requirement that $\Omega = 1$ give estimates of $m_\nu \approx 10$ eV[1], which is close enough to current experimental limits and theoretical predictions to be intriguing.

There is also experimental evidence for deviations from the Standard Model. The ITEP group in Moscow has measured deviations from an allowed shape of the β spectrum of ^{3}H that are consistent with a rest mass for the electron anti-neutrino in the range $17 < m_\nu < 40$ eV[9]. This experiment is not confirmed and is being repeated by many different laboratories. Other evidence for new neutrino physics comes from the solar neutrino experiment conducted by Ray Davis and collaborators[10]. In this experiment neutrinos coming primarily from ^{8}B decay in the sun are detected by counting the radioactive ^{37}Ar created in the reaction $\nu_e + {}^{37}\mathrm{Cl} \rightarrow {}^{37}\mathrm{Ar} + e^-$. Their latest results for the capture rate and the latest prediction calculated from the standard solar model[11] are:

$$<\sigma\phi>_{exp} = 2.1 \pm 0.3 \text{ SNU}$$

$$<\sigma\phi>_{calc} = 5.8 \pm 2.2 \text{ SNU}$$

Here σ is the cross section for the above reaction, ϕ is the solar neutrino flux, one Solar Neutrino Unit (SNU) $\equiv 10^{-36}$ captures per target nucleus per second, and the quoted theoretical (experimental) error is 3σ (1σ). While it is possible that the predicted solar neutrino flux is in error, as yet no problem with the standard solar model capable of explaining this discrepancy has been found. Another possibility is that the electron neutrinos created in the sun oscillate into another flavor of neutrino (perhaps amplified by the material in the sun[12]) before they reach the earth and are therefore incapable of capture on ^{37}Cl.

Neutrino oscillations are one of a number of phenomena which might offer a glimpse of the next level of physics beyond the Standard Model. Effects like neutrinoless double-β decay, proton decay, rare decays of the muon, and sensitive measurements of β shapes as a search for neutrino mass may make it possible to observe GUT's scale interactions with a relatively modest size experiment. This has motivated a number of searches for neutrino oscillations, which we will now consider in greater detail.

1.3 NEUTRINO OSCILLATIONS

The subject of neutrino oscillations and the current state of neutrino oscillation experiments are covered in more detail in the appendix. In brief, neutrino oscillations refers to a possible process whereby neutrinos of one leptonic flavor, say ν_e, would change into another flavor, say ν_μ. For this process to occur both Δm^2, the difference in squared masses of the neutrinos representing the mass eigenstates, and $\sin^2 2\theta$, where θ is the leptonic analog of the Cabibbo angle, must be nonzero. Experimental searches for this phenomenon are done by preparing as pure a beam of one

flavor of neutrino as possible and then looking either for the disappearance of these neutrinos or the appearance of neutrinos of another flavor.

Nuclear reactors are one useful source of neutrinos. Nuclear reactors obtain power from the fission of heavy elements, primarily ^{235}U and ^{239}Pu. The fission normally produces two fragments whose mass distribution is given by a double peaked function as shown in fig. 1. The great majority of these fragments are neutron rich and thus decay by β^- decay, a small fraction will decay by β^+ [13]. These β^- decays provide a large flux of $\overline{\nu}_e$ ($\approx 10^{20}$/sec) which can be observed by using the inverse β decay reaction $\overline{\nu}_e + p \rightarrow e^+ + n$. From the energy spectrum of the positrons one can obtain an energy spectrum of the $\overline{\nu}_e$. Variation of this spectrum with distance from the reactor is then the signal for neutrino oscillations. For reasons discussed in the appendix it is important in practice to know the $\overline{\nu}_e$ spectrum leaving the reactor; this spectrum is obtained by summing the $\overline{\nu}_e$ spectra from the various fissioning nuclei in the reactor. We will now discuss how these $\overline{\nu}_e$ spectra are obtained, and how the measurement of the ^{252}Cf spectrum can contribute towards their understanding.

1.4 POST FISSION ν AND β SPECTRA

The current literature contains two prescriptions for obtaining the energy spectrum of $\overline{\nu}_e$ (and the corresponding β spectrum) from the β decay of the fission fragments from a particular fissioning nucleus. The first method involves summing all the individual β decay branches explicitly, using some approximation scheme to make up for the lack of experimental knowledge of the details of Q-values and branching ratios for all of the nuclei involved. In the second method the β spectrum is experimentally determined and then converted into the corresponding $\overline{\nu}_e$ spectrum. The two methods are in fact closely related, as the β spectra measured in the second

provide a check on the first, which is then used to predict $\overline{\nu}_e$-spectra for those fissioning nuclei which have not had their β spectra measured. We shall present the results of each method in turn, including in the second method measurements of β spectra which have not been converted, and then discuss what these results mean.

1.4.1 Predictions by the Summation Method

To calculate the neutrino spectrum from a given fissioning isotope by the summation method one evaluates[14]:

$$N_{\overline{\nu}_e}(E_{\overline{\nu}}) = \sum_n Y_n(Z,A,t) \sum_i b_{n,i}(E_o^i) P(E_{\overline{\nu}}, E_o^i, Z) \tag{1}$$

where $Y_n(Z,A,t)$ is the number of β decays per unit time of the fragment Z,A after the fissioning nucleus has been in the neutron flux for a time t. For exposure times longer than the fragment lifetime this converges to the cumulative fission yield and is independent of t. $b_{n,i}(E_o^i)$ is the branching ratio for the i th β decay branch (to an excited (or ground) state in the daughter) of the fragment n with endpoint energy $E_o^i = Q_n + m_e c^2 - E_{exc}^i$, where Q_n is the Q-value for the fragment n and E_{exc}^i is the excitation energy in the daughter nucleus for this particular branch. $P(E_{\overline{\nu}}, E_o^i, Z)$ is the normalized Coulomb corrected spectrum shape factor, which for these calculations is assumed to have an allowed shape. To calculate the corresponding electron shape one only has to replace $P(E_{\overline{\nu}}, E_o^i, Z)$ with the correct shape factor for electrons.

The Y_n values can be found in standard tabulations[15], at least for the case of $t \to \infty$. For finite t one must also consider β decay lifetimes, delayed neutron emission and neutron capture on the fission fragments, but this does not seem to present serious difficulties. The neutrino shape factor for an individual β spectrum is exactly calculable in the allowed approximation, and calculations have shown that this

approximation contributes to the error at most a few percent[16]. The problem lies with getting values for the branching ratios and Q-values, for which firm experimental data exist in the case of ^{235}U for less than 1/4 of the ~700 known fission fragments. For the rest the Q-values and branching ratios must be obtained from some semi-empirical model.

The different methods used to obtain the branching ratios for these unknown nuclei are the major source of the disagreement between the published calculations using the basic method of (1)[1]. While the unknown nuclei contribute relatively little to the total yield of $\overline{\nu}_e$, they contribute a sizable fraction of the $\overline{\nu}_e$ at high energies (fig. 2); thus differences in their branching ratios produce significant changes in the predicted spectra. The more branching one assumes to highly excited states in the daughter, the fewer high energy neutrinos one predicts. The calculations of Kopeikin[17] assume a single excited state in the daughter which is given an energy and branching ratio extrapolated from the averages in selected nuclei with known decay schemes. Three different values were used for these quantities depending on whether the daughter was even-even, odd-odd, or either even-odd or odd-even. The criteria for selecting known nuclei to be averaged are not given in the publications. The predicted $\overline{\nu}_e$ spectra for this and all the other calculations discussed in this section for ^{235}U are in fig. 3. For clarity and to emphasize the differences the spectra are shown divided by the $\overline{\nu}_e$ spectrum derived from the measured β spectrum in reference 18 in fig. 4.

A scheme similar to Kopeikin's[17] was initially used by Avignone[19], producing still harder spectra (harder meaning more high energy $\overline{\nu}_e$). In subsequent publications he modified this scheme, and eventually included excited states in the daughter analogous to all known excited states in nuclei of the same Z with A differing by an even number of units[20]. This produced softer spectra, but they were still harder

than the ones discussed below. The calculations of Davis et al.[14] and of Vogel et al.[21] use a more complicated set of branching ratios derived from the work of Aleklett and Nyman[22]. Here the β strength was divided into a part α' which feeds levels above and a part $\alpha = 1-\alpha'$ which feeds levels below the pairing energy P in the daughter. The strength below P was divided equally into three levels with energies 0, $P/3$, and $2P/3$. Above P Fermi gas level densities were used and the average reduced transition rate was assumed to be constant independent of the excitation energy in the daughter nucleus. The quantity α was taken from the data in reference 22. A still more complex scheme using a microscopic calculation of the branching ratios was employed by Klapdor and Metzinger[16]; it produced the softest spectra.

It should be pointed out that the values of $b_{n,i}(E_o^i)$ are not the only source of error. References 14 and 21 use the same model for the unknown decays; the differences in the predicted spectra come mainly from changes in the ground state branching ratios in just 4 nuclei that were remeasured between the calculations. The error induced in the calculation by using a semi-empirical mass formula to predict the β decay Q values is estimated in reference 21, it grows with energy and is on the order of 20% at 7 MeV. Davis et al. also calculated a spectrum using the values of reference 19 for $b_{n,i}(E_o^i)$ and their own values for everything else; the resulting spectrum differs markedly from the results of reference 19 at high energies, presumably because of differences in the input data. Given these large uncertainties in the calculations, and the different methods of estimating $b_{n,i}(E_o^i)$, it is crucial to obtain some experimental test. This is provided by comparing the β spectra predicted by the above authors with the measurements we will now describe.

1.4.2 Measurements of the Post Fission β Spectrum of ^{235}U

Early measurements of the post fission β spectrum from ^{235}U were made by Muehlhause and Oleksa[23], Carter et al.[24], and Kutcher and Wyman[25]. The data of

Kutcher and Wyman were combined with a measurement of the low energy end of the distribution (E_β< 750keV) in a paper by Tsoulfanidis[26]. All of these experiments used plastic scintillators as the primary detector, and therefore suffered from very poor energy resolution, with brehmsstrahlung and scattering adding a large tail on the low-energy side of the response function. The rapidly falling ^{235}U spectrum will therefore be badly distorted if no correction is made for detector response. This correction is complicated by the fact that there is no convenient source of mono-energetic electrons available above a few MeV. Thus the response function of the detector must be extrapolated from low-energy measurements or obtained by estimation or Monte Carlo methods. The experiment of Muehlhause and Oleksa[23] makes no such correction, so their results are not comparable to later work.

Carter[24] and Kutcher[25] do make corrections to their data, but using estimated response functions that seem rather crude. In other respects the experiments are similar. Both use a gas proportional counter in front of the scintillator to suppress γ backgrounds, and both subtract background using a graphite block placed to stop the "correct" electrons from hitting the counter. Despite their similar technique, however, the experiments measure very different shapes for the spectrum. Carter's data are shown in fig. 5 , and values derived from the empirical fit given in their paper are shown in fig. 6 along with the Kutcher data (taken from reference 26) and the results of the other experiments discussed below. The ratio of all of these spectra to the results of reference 18 are shown in fig. 7.

A plastic scintillator system was also used in the experiment of Borovoi et al.[27]. We shall discuss this experiment in some detail because of its relevance to our later discussion of ^{252}Cf. A schematic of the apparatus and a detail of the detector are shown in fig. 8. The β detector and a neutron source were separated by borated polyethylene shielding and set up in front of a disc upon which were mounted

targets of ^{235}U, ^{239}Pu, and blank targets for background subtraction. The disc was rotated at 800 rpm so that the targets alternately passed in front of the neutron source and the detector. Spectra were simultaneously acquired for the ^{235}U, ^{239}Pu, and blanks. The neutron source consisted of a ^{252}Cf source in a paraffin block moderator, the total flux was 10^7 n/sec. The variation in the β spectrum from non-thermal neutrons was shown to be < 1%. The targets were 20 x 20 mm x 39 mg/cm^2 foils of the fissioning isotopes surrounded by 5.4 mg/cm^2 Al foil and 4.27 mg/cm^2 polyethylene film to contain the fission products. Background was also measured by blocking the electrons from the source with 2.7 g/cm^2 Al or graphite; this was found to agree with the continuously measured background.

The β detector was a ΔExE plastic scintillator telescope. The main detector was a 50 x 50 mm stilbene crystal and the ΔE detector was a 30 mm in diameter by 0.18 mm thick plastic scintillator viewed by two phototubes in coincidence to reduce noise. Requiring the ΔE-E coincidence reduced the background in the E detector by $\approx$200. Some protection from cosmic rays was obtained from a 40 x 40 x 20 cm scintillator veto panel located over the detector. Calibration measurements were made of conversion electrons from ^{207}Bi (E_{e^-} = 0.991,0.482 MeV) and of electrons from the β decays of ^{144}Pr (E_o = 2.996 MeV), ^{42}K (E_o = 3.519 MeV), and ^{38}Cl (E_o = 4.91 MeV). The response of the detector to ^{207}Bi is shown in fig. 9, the measured resolution was 11% at 1 MeV. Measurements were made with thin and thick sources to subtract out the effects of the cover foils, the correction is shown in figure 19.

A total of more than 10^6 sec of data was then collected for ^{235}U, ^{239}Pu, and the background. A comparison of one run's data and background is shown in fig. 11. The signal/noise drops to ~1 at 5 MeV and ~1/10 at 7 MeV. The raw spectra - background is first corrected for losses in the source and detector covers, it is then corrected for the response function of the detector as discussed above. Figure 9

demonstrates the detector response to mono-energetic electrons; the low energy tail contains ≈12% of the counts. The adopted resolution function is shown in fig. 12. This response is de-convolved from the measured spectra producing the final experimental spectra shown in fig. 13; the ratio of the measured ^{235}U spectrum to the results of reference 18 is shown in fig. 7. This experiment measured only the spectral shape, the absolute rate/fission was set at 2 MeV by averaging the other available calculations and experiments. The errors claimed were 1% in the linearity of the energy scale producing a 4% error in the rate at 5 MeV and 10% at 7 MeV, a 5% (7%) error for ^{235}U (^{239}Pu) from the procedure for getting the absolute rate, 1% for E > 3 MeV from the de-convolution of the detector response, 3-5% error for e > 1 MeV from the source thickness corrections, and statistical errors in the raw counts and in the background. The total claimed errors can be seen in fig. 13; they are roughly ± 6% at 2 MeV and 4 MeV, 9% at 7 MeV, and 30% at 8 MeV.

While it is difficult to analyze an experiment on incomplete information, several criticisms can be made just on the basis of reference 27. The first concerns the method used to establish the energy calibration. The spectra used are shown in fig. 14, these β spectra are not corrected for detector response. They therefore show systematic deviations from straight Kurie plots in the 4-5% range. This will produce an offset in the fitted endpoints (which will not appear in a linearity check) which can be in excess of the 1% quoted. This can be seen in fig. 15, which shows the measured ^{144}Pr spectrum, the theoretical β shape and the shape predicted by their method of removing the detector resolution. Inspection of the figure shows that the endpoint predicted from a fit to the measured shape is ≈2.5% lower than the true endpoint. The steeply falling spectrum will magnify this error at high energies, producing an overestimate of the β rate at 7 MeV of ≳25%. It is also interesting to note that the fitted spectrum shows systematic deviations from the measured points near the

endpoint which are consistent with an under-compensation for detector resolution. This could also lead to an overestimate of the rate at high energy, and in any case casts doubt on the claimed 1% error in de-convolution. Another possible source of error comes from electrons escaping the detector at the higher energies. From the drawing of the detector given it appears that electrons can hit the E scintillator near the edge, and some presumably escape without depositing their full energy. This effect should increase with energy and no data at all are available to check for it above 4.5 MeV. Below 4.5 MeV this effect could be combined with or masked by the 4-5% systematic deviations discussed above. There is also no mention of possible source related backgrounds such as scattering off the collimators which would not be included in their background subtraction.

The only measurements of the β spectra of ^{235}U, ^{239}Pu, and ^{241}Pu using a magnetic spectrometer were done by Schreckenbach et al.[18,28,29,30] using the BILL spectrometer[31] at ILL. The BILL spectrometer is a unique device with the target located within the reactor core. Electrons from the target exit the reactor through a 14 m beam tube and are focused onto the detector (a multiwire proportional counter) by two double-focusing iron-core magnets. The momentum resolution was set at $\Delta p/p = 3.5 \times 10^{-4}$, making a de-convolution of the measurement for detector resolution unnecessary. The energy calibration, absolute efficiency and the variation of the spectrometer efficiency with energy were measured using internal conversion electrons from (n,γ) reactions on various targets. Correcting for the latter effect (~10% change for 1 to 9 MeV) produced a ~3% error in the final spectrum. Since the energy calibration is done with line sources of well known energy the error is presumably negligible (no value is given in the publications). The targets consisted of 1 mg/cm^2 of the fissioning isotope sandwiched between two 7 mg/cm^2 nickel foils. Background was determined using a non-fissile isotope target of the same

construction. For the latest ^{235}U run the signal/background was 6, 2.5, 0.5, and 0.12 at 3, 6, 8, and 9 MeV, respectively. Scattering in the target and spectrometer were shown to be negligible.

The measured β spectra are shown in fig. 6. The claimed total error in the ^{235}U spectrum is 3% for E < ~7.5 MeV, rising to ~6% at 8 MeV and ~30% at 9 MeV. The $\overline{\nu}_e$ spectra were constructed from the measured β spectra by assuming that the measured spectrum for the ^{235}U (^{239}Pu) is the superposition of 30 (25) allowed β decays P_i with endpoints E_o^i. The relative normalizations of these hypothetical branches were then fitted to reproduce the measured β spectra. A $\overline{\nu}_e$ spectrum corresponding to each branch was then constructed taking into account the proper kinematics and radiative corrections for neutrinos, the final $\overline{\nu}_e$ spectra are then just the sum with the same relative normalization as the β spectra. Numerical tests indicate that this conversion procedure adds $\lesssim$1% to the errors given above. The resulting $\overline{\nu}_e$ spectra are shown in fig. 3.

The ^{235}U and ^{239}Pu β spectra were also measured with a plastic scintillator telescope by Kayser[32] at ILL. This experiment used the same basic technique as the scintillator experiments above, with the exception that an attempt was made to actually measure the detector response to mono-energetic electrons obtained from the BILL spectrometer. Unfortunately little information is available about this experiment besides the results, which are shown in fig. 16. These spectra seem to agree with the softer predictions at low energies and the harder predictions at high energies (under-compensation for detector response?). However without more hard data it is difficult to put much weight on these results.

1.4.3 Summary

What then is our current understanding of post-fission $\overline{\nu}_e$ and β spectra? The results tend to fall into two rough groups, the harder spectra (the predictions of

Avignone[28,29] and Kopeikin[27], the experiments of Borovoi et al.[27], Tsoulfanidis et al.[26], and Kayser[32]) and the softer spectra (the predictions of Davis et al.[14], Vogel et al.[21], and Klapdor and Metzinger[16], and the measurements of Schreckenbach et al[18,28,29,20]. and Carter et al.[24]). Given the superior experimental method used by Schreckenbach and the physically more reasonable assumptions that go into the calculations which produce the softer spectra it is tempting (and not unreasonable) to simply take these as correct. That view, however, is not universally held (the Rovno group (see appendix) continues to use the spectra of Kopeikin). Considering the importance of these spectra in oscillation experiments as outlined in the appendix, especially in regard to the Gösgen-Bugey disagreement, it is important to seek an independent way to test them.

1.5 ^{252}Cf AS A TEST CASE

^{252}Cf decays with a 3.09% branch by spontaneous fission, the total half-life is 2.64 y. The remaining 96.91% of the decays are α decays to ^{248}Cm, which has a half life of 3.5×10^5 y, preventing particles from subsequent decays from contaminating the ^{252}Cf fission products. The spontaneous fission of ^{252}Cf produces experimental advantages over the neutron induced fission of ^{235}U and ^{239}Pu. The ^{252}Cf can be encapsulated and placed directly in a spectrometer, avoiding the technical problems of having the source in a reactor and also the attendant reactor related backgrounds. The backgrounds are large in all of the experiments discussed above; in the ^{252}Cf experiment we performed they were negligible. Comparison of the measured electron spectrum from the β decays of the fission products with predictions made by the methods described in section 1.4.2 then produces a direct test of these methods. In subsequent chapters we will discuss our measurement and prediction; we shall now discuss what has been done by others prior to this work.

The β spectrum from ^{252}Cf was calculated by Kopeikin[33] and measured by Knief et al.[34] and Borovoi et al.[35] Kopeikin used the same method as discussed above. The calculated electron spectrum is shown in fig. 17; the total predicted β yield is 5.8± 0.2/fission. The predicted spectrum is much softer than the ^{235}U spectrum. The explanation of this can be seen in fig. 1, taken from Kopeikin's[33] paper. This figure shows the fission yields as a function of A for ^{235}U and ^{239}Pu thermal neutron induced fission and ^{252}Cf spontaneous fission. It also shows the average ground state-ground state Q-value as a function of A. As one goes from ^{235}U to ^{239}Pu to ^{252}Cf the lower hump in the yield curve moves to higher A, reducing the average Q-value for the low A decays and thus softening the spectrum.

The experiment of Knief et al.[34] was done using the apparatus of Kutcher and Wyman[25] for energies above 1 MeV and Tsoulfanidis[26] for energies below 1 MeV. Measurements were made of the time evolution of the β spectrum and of the equilibrium value, only the latter is of interest here. The source consisted of ^{252}Cf (~1000 fissions/sec.) sandwiched between two 25 μm thick Mylar foils. Background was subtracted by blocking the electrons from the source with a 2.5 cm thick graphite block. Absolute yields were obtained by measuring the α particles from the source and the detector solid angle. Fig. 18 shows the raw spectrum, the spectrum after unfolding for detector response, and an empirical fit to the data $N_\beta(E) = \exp(1.52 + 0.0519\ E - 0.403\ E^2)$. The total β yield measured is 6.7 ± 0.3 e^-/fission. The error on the individual points in fig. 18 was estimated to be $\lesssim$10%.

The experiment of Borovoi et al.[35] used the same detector as his above mentioned work on ^{235}U. No details are given in their paper about the source construction. Sources ranging in strength between 850 and 1.8 x 10^5 fissions/sec. were used to reject pileup. Background was measured by blocking the electrons with 2.7-3 g/cm^2 carbon or aluminum, the signal/background was ~100 at 2 MeV, ~10 at 6.5

MeV, and ~1 at 8 MeV. Only the shape of the spectrum was measured, no attempt was made to obtain an absolute rate. The measured spectrum was compared to the prediction of Kopeikin[33] by normalizing the measurement to the predicted rate at 920 and 1486 keV. The results are shown in fig. 17; the agreement with the prediction is difficult to give quantitatively, but appears to be within errors. The criticisms of their earlier experiment are presumably as valid here, although they do in this paper specifically mention taking account of electrons escaping from the scintillator.

CHAPTER 2

Experimental Set-Up

2.1 Overview

We will discuss the general set-up of the experiment in this section, the succeeding sections will then cover each piece of the apparatus in more detail. An earlier incarnation of the device is described in reference 36, however the vacuum chamber and magnet are about the only substantive pieces of apparatus that were not modified or replaced in the current experiment. An overview of the experimental set-up is shown in fig. 19. Electrons emitted from the source (^{252}Cf,^{90}Sr) or target (^{12}B,^{20}F) first pass through the active entrance aperture. This consists of an annular plastic scintillator detector (hereafter called the slit) which determines the spectrometer acceptance and a thin wire chamber (hereafter called the coincidence counter) for background rejection. The electrons are then bent 180° by the flat-field electromagnet and exit through a 3-wire chamber capable of track reconstruction. The wires run parallel to the magnet pole tips and perpendicular to the magnetic field direction (vertical in the figure), the wire distance from the magnet determines one component of the electron's position. The electron position perpendicular to the wire direction is determined by the drift time of the deposited charge to the wire, while position along the wire is determined by charge division. After exiting the wire chamber the electrons hit a backing scintillator used for further background rejection and as a start signal for the wire chamber timing.

The momentum of an electron p_e and its radius of curvature ρ in a uniform magnetic field B are related by (see Jackson, eq. 12.42)[37]:

$$p_e = \frac{e}{c} B\rho = 0.300 B\rho \tag{2}$$

for p_e in MeV/c, B in kilogauss and ρ in centimeters. Therefore a position spectrum along the wire (ignoring fringing fields) is also a momentum spectrum of the incident electrons. The geometrical momentum resolution of the spectrometer is set by the acceptance through the relation:

$$\frac{\Delta p_e}{p_e} = \frac{\Delta \rho}{\rho} \tag{3}$$

where $\Delta\rho$ is the size of the hole in the slit and by the position resolution in the wire chamber; it is typically ≈1%. At a given field setting the spectrometer measures the momentum spectrum over a range of momenta given by $p_{max}/p_{min} \approx 2$.

2.1.1 Source and Target Construction and Alignment

The design of the spectrometer requires that the source or target be confined to a 2 mm spot aligned perpendicular to a line through the center of the slit/coincidence counter. Localizing the source is particularly difficult in the case of ^{252}Cf. Self-sputtering by the fission fragments will cause ^{252}Cf to creep, thus it must be completely contained. The final design of the ^{252}Cf source is shown in fig. 20. The ^{252}Cf (181 μC total activity) was deposited by evaporation from solution onto the end of a 2 mm diameter Be rod and ~200 $\mu g/cm^2$ Au was sputtered on to it to keep the ^{252}Cf from creeping. The rod was then placed in a Be cylinder with a 0.025 mm (4.7 mg/cm^2) thick front window and fixed in place with epoxy. Beryllium was used for the source capsule so that backscattering would be negligible[38]. The ^{90}Sr source (15.3 μC) was prepared in an identical capsule. Both of these sources were made to our specifications by Isotope Products of Burbank, Ca. ^{20}F and ^{12}B were produced by (d,p) reactions on ^{19}F and ^{11}B using 2.2 MeV deuterons from the 4 MeV Dynamitron accelerator at ANL. The targets were 2 mm diameter spots centered on 2.5 cm^2 x

0.025 mm Be backing. The ^{19}F target was made by evaporating LiF from aqueous solution a drop at a time to form a few mg/cm^2 thick deposit, the ^{11}B was vapor deposited through a mask to a thickness of ~2mg/cm^2. We used LiF enriched to >99% ^6Li to reduce background from the β decay of ^8Li.

The position of the source/target/slit/beam directly affected the energy calibration, a 1 mm error in the position would produce a 1.25% error in the energy calibration. The positioning and alignment were done using a system of three telescopes as shown in fig. 21. First, telescope 1 was aligned with the center of the beam pipe. The tantalum beam collimators were then aligned to give a properly positioned beam. Telescope 2 was aligned to the center of the magnet pole pieces, and a wire cross-hair target was used to position the target holder so that the center of the target was at the intersection of telescopes 1 and 2. The target holder was then fixed in position and the slit and coincidence counter installed so that they were centered on telescope 2. The light produced by a low-energy proton beam on a quartz target was used to verify the beam spot/slit/coincidence counter alignment. Telescope 3 was then used to verify that the target spots were in the correct position and to position the ^{252}Cf and ^{90}Sr sources. Using this method the positions of the various components could be set to ≈0.1 mm.

2.1.2 Slit Scintillator and Coincidence Counter

Passive collimation of ~10 MeV electrons is inherently very difficult. Scattered electrons would seriously distort the measured spectral shape if it were not possible to veto those electrons which scatter off the slit. Therefore we used an annular plastic scintillator to define the entrance aperture (fig. 22). The slit scintillator is a piece of NE102 measuring 1.91 cm x 1.27 cm x 0.08 cm thick with a 2 mm hole. It was counterset into a tapered light guide which was coupled to a Hamamatsu R1213 1.91 cm photomultiplier tube with optical epoxy. This removed the photo-tube from the

strong fields in the region near the pole tips; it was also shielded from stray fields by wrapping it in mu-metal. Fig. 23 shows a typical pulse height distribution in the slit for recorded events in coincidence with the backing scintillator.

A diagram of the coincidence counter is shown in fig. 24. The windows are 2.5 x 10^{-4} cm mylar, the fill gas was high purity 80% Argon/ 20% CO_2 at 400 Torr, for a total thickness of ~1mg/cm^2. The pressure was maintained by a Hg manostatt to ≈ 1 part in 10^3 at a low flow rate ($\lesssim$ 1 liter/min). The tantalum shield was installed to reduce the singles rate from electrons passing through the front cover rather than the hole. The drift electrode was added to produce a more uniform drift field in the active volume. The counter was operated in the Geiger region with typical operating voltages of -420 V for the drift field and +1350 V for the wire. A pulse height spectrum is shown in fig. 25, the signal is well separated from the noise. Adding this counter largely eliminated the backgrounds due to scattering from the front of the spectrometer allowing accurate determination of the endpoints of the calibration β spectra. It also reduced backgrounds due to neutrons and gammas from the ^{252}Cf, allowing an accurate determination of the spectrum at high momenta were the rate is low.

2.1.3 Position Sensitive Wire Chamber

A diagram of the wire chamber is shown in fig. 26. Electrons exiting the magnet traverse the uniform field region of the counter. The charge they deposit is then drifted to the wires, which are operated in the proportional mode. The gas was the same as above at atmospheric pressure with a similar flow rate. The drift speed of the deposited electrons was ≈1.4 cm/μs. The energy deposited in the active region of each wire was only ~1 keV, thus the resulting pulse height distribution for the total energy deposit was a Landau distribution (fig. 27). The anode wires were 13 μm diameter, high-resistance Moleculoy (180 Ω/cm). They were measured to be 13.39 ±

0.05 cm long, the error coming primarily from determining the exact location of the solder joint. The wire chamber resolution achieved was 0.4 mm in the drift direction and 1.5 mm along the wire (these indicate the ability of the wire chamber to locate an electron, they should not be confused with the spectrometer resolution which includes geometrical effects from the slit size).

2.1.4 Magnet and Other Apparatus

The magnet was a 180° flat-field (dipole) design. The pole tips were made of soft iron and were semicircular in shape. The gap was 1.905 cm with a few mm lip at the edges to increase the area of field uniformity. Extensive field maps were carried out prior to the work mentioned in reference 36 to verify that inhomogeneities and fringe fields were at an acceptable level. Our approach was to double check this using calibration spectra over the whole momentum range of interest. The fields used in this experiment ranged from 0.98 to 4.9 kilogauss. These were set directly on the magnet power supply, which was a specially constructed unit with a Hall probe feedback system to compensate for hysteresis. The accuracy and reproducibility of the dial settings were verified with an NMR gaussmeter to better than 1 part in 10^3.

The backing scintillator was a single piece of NE102 measuring 5.08 cm wide x 20.3 cm long x 0.317 cm thick attached to a light guide couple to a Amperex XP2230 PMT. It was located ~20 cm behind the wire chamber. A typical pulse height spectrum from this detector is shown in fig. 28. A few percent of the events are lost below the discriminator level. While this loss is momentum dependent it does not introduce significant error at the level of accuracy of this experiment. The entire apparatus was located in a ~0.8m^3 stainless steel vacuum chamber which was maintained at a pressure of $< 10^{-3}$ Torr by a diffusion pump.

2.2 Electronics and Data Acquisition

Considerable effort was put into optimizing the electronics for this experiment, a block diagram of the final setup is shown in fig. 29. They divided roughly into two parts; the analog electronics which measured and digitized the pulse height from each of the detectors for each event, and the timing/logic electronics which determined event timing and decided which events to record. These were in turn controlled by a PDP-11/45 computer. The following sections will discuss in more detail those parts of the electronics not obvious from the diagram.

2.2.1 Analog Electronics

The position P of an event along a resistive wire of length L is given by:

$$P = L \frac{Q_L}{Q_L + Q_H} \tag{4}$$

where Q_L and Q_H are the charges collected at the low momentum and high momentum ends of the wire. For this apparatus this requires that the electronics convert charge to pulse height (and then digitize the results) accurately and linearly for pulse heights that vary by a factor of ~200 (the energy deposition for a given electron varies by a factor of ~20, and and the difference in pulse heights at one end of the wire for an electron hitting at that end versus the other is ~10). The electronics responsible for this are shown in fig. 29. Each end of the wire was connected through 30 cm of RG/58 cable to a specially modified Ortec 142IH pre-amplifier. The modifications were necessary to minimize a nonlinearity introduced by having a pre-amp at each end of the wire. After charge was deposited at a point on the wire the signal in each pre-amp would show a fast rise followed by a slower pulse caused by the redistribution of the charge on the two input capacitors through the resistive wire connecting them. These unwanted slower pulses would cause the measured

position to move closer to the center of the wire relative to the true position. This was corrected by increasing the size of the input capacitors to 5000 pF (which increased the RC time of the slow pulses) and using fast clipping (100 ns differentiation) on the amplifiers. These steps, however, increased the noise (to ~10 mV peak to peak on the amplifier output), producing the resolution per wire limit already quoted. The amplifier used on the wire chamber signals was built for this experiment, it had the 100 ns differentiation mentioned above, linearity to < 1% and a 0-2 V output range matched to the ADC.

The above method requires that the pre-amp/amplifier gain at each end of the wires be matched to better than 1%, which proved to be difficult to maintain over the long running periods of the experiment. A pulser system which periodically injected pulses into alternate ends of the wire and tagged them with a pulse to the ADC was therefore used to keep track of gain drifts and remove them in later analysis. After the amplifier the signals were fed into an Ortec AD811 8-channel ADC. Linearity and offset corrections were obtained for each channel of the ADC by using a precision voltage source and by a method of creating artificial events by using calibrated resistors to divide a pulser signal between the ends of the wire. An offset in the ADC showed up as a change in the measured position as a function of the pulser gain. This was minimized by adding an offsetting amount to each channel in the analysis, however it was still necessary to place a lower limit on the total event pulse height in a given wire to prevent this from affecting the per wire resolution at greater than the 1% level.

2.2.2 Timing/Logic Electronics

The timing/logic electronics are shown in fig. 29. The requirements are that the system generate a strobe signal to the ADC's whenever there was a coincidence between the backing scintillator, the coincidence counter, and one of the three wires

in the wire chamber. Because of the delay due to the drift time in the wire chamber these coincidences are spread over ~ 1 μs. The system also measures the time of each detector signal relative to the scintillator. The system is started when the scintillator discriminator fires. This signal triggers two gate and delay generators (GDG) which produce a gate of preset length and a logic pulse delayed by the same amount (fig. 30). The gate from the first of these GDG's, set to 2 μs, is used to strobe the ADC's. Thus the digitization process is begun for any signal which occurs within 2 μs after a scintillator pulse. The delayed pulse of the other GDG, set to 5 μs,is sent to the clear input of the 2 ADC's and the TDC. If the electronics described next find a valid coincidence they send a signal to the blank input of this GDG, stopping the clear signal. Otherwise the digitization is stopped and the digitizers reset.

The coincidence condition was set up as shown in fig. 30. The two ends of each wire were summed in a linear Fan In/Fan Out and the resulting signal was fed to a discriminator which in turn fired a GDG which was set to 2.2 μs. These three wire gates were then fed to a coincidence box which formed an *or* coincidence from them, the output was fed to a second coincidence box. This box formed an *and* coincidence from this signal, a 2.2 μs gate fired by the coincidence counter, and the delayed pulse from the 2.0 μs gate fired by the scintillator. When a coincidence was generated it started a gate which blanked the clear pulse for 300 μs, allowing the event to be digitized and read by the computer. The time between detector signals was determined with a TDC. The 2 μs delayed pulse from the scintillator was the start, while the delayed pulses from the GDG's fired by each wire, the coincidence counter, and by the slit formed the stops. Scalers were used to keep track of the singles rates in the scintillator, each wire, and the coincidence counter.

2.2.3 Computer/Control and CAMAC Electronics

The actual data generated for each event were read by three CAMAC modules, the 2 ADC's and the TDC discussed above. These were in a CAMAC crate controlled by the PDP 11/45 computer at the Dynamitron. This computer ran a utility data acquisition routine called SNAP which permitted the user to issue CAMAC commands to the crate, store the results in a buffer, perform some online analysis, and then write the stored data to tape. For each event the 16 integers listed in Table 1 were written to tape, these event mode data were then transferred to another computer for the further analysis which will be described in the next chapter.

The computer also controlled the beam pulser as shown in fig. 31. The high singles rates in the detectors made it impossible to take useful data for the ^{12}B and ^{20}F while the beam was on, it was therefore necessary to take data in cycles. First the electronics would be disabled and the beam permitted to hit the target (during this period the drift field of the wire chamber was turned off to protect the wires from the high rate). The beam would then be electrostatically deflected near the accelerator, and after a short time to let the wire chamber settle the electronics would be enabled and data taken. After a period set to be ~2 half-lives the electronics would be disabled and the cycle restarted.

CHAPTER 3

Data Analysis

3.1 Obtaining Momentum Spectra From Event Mode Data

In this section we will discuss the reduction of the event mode data to momentum spectra, the subsequent sections will then cover their analysis. This reduction was accomplished using a large multi-purpose data reduction and sorting routine called LISA which was available at ANL. LISA sorts data (either the integers from the tape or user defined functions of these integers) into histograms based on user defined conditions (any logical combination of windows on any number of other spectra). LISA was used on the VMS/VAX in the Physics Division at ANL and was also transported to the High Energy Physics VMS/VAX at Caltech.

3.1.1 Event Cuts

The cuts which an event had to pass to be considered a good event are listed below. The first few may appear redundant with the hard-wired 3-fold coincidence condition between the coincidence counter, the wire chamber and the backing scintillator, but they were necessitated by the way the data were taken. The time taken by the computer to digitize an event was somewhat variable but was less than the 300 μs for which the clear was blanked. Thus any scintillator pulse which occurred after the digitization was finished but before the 300 μs was up would also begin digitization, the event cuts used guaranteed that none of these events are included in the final spectra. They also tighten the coincidence condition to eliminate accidental coincidences.

A good event is defined by the condition:

$$G = T_{coin} * E_{coin} * E_{scint} * (E_{slit} + \overline{T}_{slit}) * E_{wire} \qquad (5)$$

where * indicates an *and* condition and + indicates an *or* condition. The individual conditions are:

$T_{coin} \Longrightarrow$ required a tighter time coincidence between the coincidence counter and the scintillator. The time spectrum and the cut condition are shown in fig. 32. The time resolution of the counter (FWHM) was 43 ns, mainly due to the drift time in the counter.

$E_{coin} \Longrightarrow$ required a good pulse height in the coincidence counter, this condition is essentially 100% efficient.

$E_{scint} \Longrightarrow$ required that the pulse height of the scintillator is out of the noise (the cut is shown on fig. 28). This gets $\gtrsim$96% of the events in T_{coin}, as mentioned before this cut is momentum dependent at the 1% level.

$E_{slit} \Longrightarrow$ required that the pulse height in the slit be in the noise, i.e., no energy deposit in the slit (see fig. 23).

$\overline{T}_{slit} \Longrightarrow$ required that any slit signal occurs well after the slit/scintillator coincidence peak. The time spectrum and cut are shown in fig. 33. The time resolution of the slit (FWHM) was 16 ns. This condition was needed because of the high rates in the slit, especially for ^{12}B.

$E_{wire} \Longrightarrow$ required a useful pulse height from the wire chamber. The cut as applied to an individual wire is shown in fig. 27. The lower level is set as discussed in section 2.2.1, the upper limit excludes any event which could have saturated the ADC at either end of the wire. The efficiency of this cut is ~90%. Because the wire chamber gain is somewhat position dependent, this cut is momentum dependent at the several percent level. This was removed in the final momentum spectra by using the position in wire 3 for those events that did not have a good pulse height in wire 1 (wire 2, due to its different field geometry, was systematically less efficient

(~80%)). This made the efficiency ~99%, the spectral shape was then insensitive to the exact settings of these cuts.

3.1.2 Output Spectra

A large number of histograms were produced for each run; some have already been discussed; we will now consider a few more. The most important spectra were the position spectra on the wires. First the pulse height ratios were formed by:

$$R_i = \frac{EL_i}{EL_i + EH_i} \tag{6}$$

where $EL_i(EH_i)$ is the pulse height from the low momentum (high momentum) end of wire i. The tagged events from the pulser system provided the pulse height ratios for the ends of the wires R_{iL}, R_{iH} (see fig. 39). The pulse height ratios from the electron events R_{ie} were then used to obtain the position of the event along each wire P_i using the relation:

$$P_i = 2048 \frac{R_{ie} - R_{iL}}{R_{iH} - R_{iL}} \tag{7}$$

where the length of the wire has now been divided into 2048 channels. A position spectrum for ^{252}Cf taken with B=1.33 kG is shown in fig. 35, the cut offs at low and high momentum are caused by the ends on the slots in the ground plane of the wire chamber.

Several other histograms were created from these position spectra. The most important of these has already been mentioned, the spectrum created from the P_1 if the energy deposit in wire 1 passed the cut and from P_3 otherwise (actually P_3 was offset by ~0.5 mm to counter fringe fields and perhaps a small difference in the wire positions, this made a negligible difference). This was the spectrum used as the final momentum spectrum for each run. Also of interest are two combinations of the wire

positions P_i. For example (see fig. 36)

$$P_R = 2P_2 - P_1 - P_3 . \tag{8}$$

P_R should be 0 for an electron with a straight trajectory through the wire chamber, it is therefore a measure of the resolution along the wires and of scattering in the gas in the chamber. A typical histogram of P_R is shown in fig. 37; it was remarkably constant as a function of the field setting (showing that scattering in the gas was negligible) at a value that corresponds to the per wire resolution of 1.5 mm already quoted. An analogous combination of the wire timings gives the resolution in the timing direction of 0.4 mm, unfortunately for a variety of reasons the design of the spectrometer does not take advantage of this. The main use of the timing information was in checking the alignment of the sources and targets.

The other combination of wire positions of interest is:

$$P_A = P_3 - P_1 . \tag{9}$$

P_A is related to the angle between the electron trajectory and the wires (see fig. 36). It increases as the electron momentum decreases as shown in fig. 38. This is primarily caused by scattering in the front window of the wire chamber (1 mg/cm^2 Mylar) and in the coincidence counter (while scattering in the coincidence counter does not to first order affect the position of the electron along the wire it does affect the angle). This scattering causes a decrease in the spectrometer efficiency for low momenta as electrons are scattered so that they miss the backing scintillator. We will discuss in the next section the correction for this effect using the ^{20}F decay.

3.2 Calibration Spectra

The position spectra in the wire chamber discussed in the last section were converted into momentum spectra using a relation derived from eq. (2):

$$p = 0.3B(0.00327P_i + r_0) \tag{10}$$

where p is in MeV/c, B is the magnetic field in kilogauss, P_i is the position along the wire (in 2048 channels), 0.00327 cm is the increase in the radius of curvature of the electron trajectory from a change in P_i of one channel, and the single adjustable calibration constant r_0 is just equal to half the distance from the center of the slit to the start of the wire. The calibration spectra were used to determine r_0 and to measure the detector efficiency as a function of momentum by fitting the measured spectra with r_0, the normalization, and in some cases a background as free parameters. A least-squares fitting program was written to perform the fits, it was checked using Monte Carlo generated β spectra. Deviations from these fits were then an indication of a momentum dependent efficiency.

3.2.1 β Shapes

The calibration spectra were assumed to follow a standard β decay shape given by:

$$N(p)\,dp = kp^2(E - E_0)^2 F(E,Z)\,G(E,E_0)\,S(E)\,dp \tag{11}$$

where k is the fitted normalization, p comes from eq. 9, $E^2 = p^2c^2 + m_e^2c^4$ is the square of the electron's total energy in MeV, for p in MeV/c, and E_0 is the electron end-point total energy in the same units (see Table 2). An analytical fit was made to the tabulated values for the Fermi functions $F(E,Z)$ from reference 39, the deviations from the fit (a fourth order polynomial in p) were negligible over the energy range of interest. A routine was written to evaluate the radiative corrections

$G(E,E_0) = 1 + \frac{\alpha}{2\pi} g(E,E_0)$ using the analytical expression for $g(E,E_0)$ in reference 40, this correction is of the order of 1%. The shape factor $S(E)$ for each decay is given in Table 2, for the ^{12}B and ^{20}F decays they are just the weak magnetism corrections taken from reference 41, for the ^{90}Sr it includes the kinematic shape factor for a unique first forbidden decay and a correction taken from reference 42.

3.2.2 Determining r_0

The results of two accelerator runs of the ^{12}B and ^{20}F spectra, separated by about a month, will be presented here. In between the two runs the detectors were removed from the spectrometer, the wires and windows changed on the wire chamber, and all the alignment re-done (all the ^{252}Cf and ^{90}Sr data were taken after the second run). The momentum spectra from these runs (along with the fits which will be further described below) are shown in fig. 39 (runs 94 and 98 are from the first accelerator run, runs 116 and 138 are from the second). Past the endpoints there are only a few counts/channel, a factor of ~100 less than without the coincidence counter. Source unrelated backgrounds are in fact negligible, these counts come from large angle scattering in the spectrometer. The spectra are cut off at channel 30 out of 128 to avoid edge effects in the lower momenta spectra.

The values of r_0 found from fitting these spectra are shown in Table 3. The errors are dominated by the effects of the response function of the spectrometer. Fig. 40 shows the effect of finite spectrometer resolution near the endpoint of a β spectrum. Fig.41 shows the effect of this on typical fits. This causes the fitted value of r_0 to vary depending on how much of the spectrum near the endpoint is included in the fit. This is further complicated by the background of a few counts/channel which becomes important near the endpoint, and statistical errors determined by Monte Carlo of 0.2% (± 0.008 cm). The values in Table 3 were found by averaging

the values obtained by varying the range of momenta included in the fit and the background, the errors represent the range of values obtained. The average value with a rather conservative error of $r_0 = 4.006 \pm 0.015$ cm is henceforth adopted.

The effects of the scattering mentioned in section 3.1.2 make the determination of r_0 with the ^{90}Sr more difficult. Without explicitly including the response function a reasonable fit can only be obtained by excluding the part of the spectrum near the endpoint, the fitted value of r_0 then becomes very sensitive to the efficiency function discussed in the next section (the values obtained are in the range 4.00-4.12 cm, but the errors are at least ± 0.1 cm), the ^{90}Sr is therefore not included in the determination of r_0 at this stage. An earlier determination of r_0 using 0.976 MeV conversion electrons from a ^{207}Bi source gave a value consistent with the value measured with the ^{12}B and ^{20}F at that time. While the wide response function of the spectrometer at these low energies (FWHM ~13%) produced an error in this determination of ~1.5%, and it is therefore not included in the final determination of r_0, it does show the validity of eq. 9 over a wide range of energies.

3.2.3 Spectrometer Efficiency

One can test the momentum independence of the spectrometer efficiency by fitting a β spectrum over a range of momenta $pmin \leftrightarrow pmax$ using successively lower values for $pmin$. If the relative efficiency at different momenta is not constant the fit parameters will then vary as a function of $pmin$. When this test is applied to the ^{12}B spectra the fit parameters are in fact independent of $pmin$ (variation < 0.5%). The deviations from the fit expanded to show the low momentum part are shown in fig. 42 , no evidence is seen for a systematic curvature at the 0.5%/MeV level. When the same test is applied to the ^{20}F spectra, however, both runs show changes in r_0 and the normalization consistent with the spectrometer efficiency falling by ~5% at the lowest momentum (for both runs r_0 decreases by ~0.5% and the norm by ~1-2%

when *pmin* goes from channel 50 to 30).

To measure this effect at lower energies a ^{20}F run was done at lower magnetic field (B=1.19 kG). The spectrometer efficiency ε was assumed to be of the form:

$$\varepsilon = 1 - ae^{-bp} . \tag{12}$$

(This form was selected for no reason other than it fit the data). The low field momentum spectrum was then fitted keeping r_0 fixed at 4.006 cm and allowing the normalization, a and b to vary. The results of the fit are shown in fig. 43, the resulting values are $a = 2.485$, $b = 1.039$ (for p in MeV/c). When this correction is then applied to the higher field measurements (with the values of a and b taken from the low field fits) of ^{20}F it corrects the above mentioned deviations, the fits with *pmin* = channel 30 and *pmin* = channel 50 give the same r_0 (variation < 0.1%) and the same norm (variation < 0.4%); furthermore the *pmin* = channel 30 fit for run 94(138) has a decrease in total χ^2 of 10.4 (5.9), a change in χ^2/dof from 1.0 to 0.87 (0.97 to 0.91) from the same fits with $\varepsilon = 1$ (it was these corrected spectra that were used in section 3.2.2 to find r_0). The low momentum deviations of the corrected fit are shown in fig. 44, once again there is no evidence for curvature at the 0.5%/MeV level.

The situation is not as satisfactory for the ^{90}Sr. When a fit is made to the momentum spectrum (B=0.98 kG) from channel 50 to 99 (the lower limit being roughly the same momentum as the lower limit in the low field ^{20}F) the χ^2/dof actually gets worse when the efficiency correction is applied, going from 1.24 to 1.43. However the deviation plots (fig. 45) show that the difference in χ^2 comes from near the endpoint. Comparison with fig. 41 shows that the deviations from the corrected ^{90}Sr spectrum have the same shape as the deviations from the other spectra and are about twice as large, consistent with the change in the response function shown by

P_A. It appears that the momentum dependent efficiency is compensating for the response function in the uncorrected spectrum (remember that the normalization is a free parameter). If the upper channels are excluded to correct this (upper limit now channel 80) the χ^2/dof is better for the corrected spectrum (0.99 vs. 1.06), but the fit is now over such a small region that this does not mean much (it is an increase in the total χ^2 of 1.9). Clearly the response function of the spectrometer would have to be explicitly included in the calculation to confirm the efficiency correction using the ^{90}Sr. However, as we shall see in the next chapter, we are for the moment primarily concerned with the spectral shape at high p where the relative efficiency is reliably measured to be constant. Thus for the moment we will just assign an error of 20% to the correction, which is shown with its error in fig. 46.

3.3 ^{252}Cf Spectrum

Once the calibration is determined measuring the ^{252}Cf spectrum is relatively straightforward. Momentum spectra were taken at 5 different fields covering the momentum range from 1.64 to 9.3 MeV/c (Table 4) selected so that adjacent spectra would overlap. Several of the field settings were remeasured several times, the spectra were reproduced to within errors (~1%, see fig. 47). Gamma or neutron induced backgrounds were checked by looking for events with the field off and with the electrons blocked with polyethylene, the rates observed were very low even considering the low rates at the high field settings (but see comments on page 36). To check that no source thickness correction was necessary the spectrum with the magnetic field set to 0.98 kG was remeasured with an extra 5 mg/cm^2 of Be on the front of the source, the spectrum was the same within errors. The integrity of the source was checked by looking for fission fragments penetrating the front window, no significant penetration was found.

To combine the different fields into one complete momentum spectrum requires the determination of the their relative normalizations R_j. These were obtained by simultaneously fitting the overlapping regions of each pair of fields to a function of the form:

$$N(p) = \exp\left(\sum_{i=0}^{n} a_i p^i\right) \tag{13}$$

with the R_j as a free parameter and $n = 3$. In this manner the R_j could easily be determined to <1%; keeping track of the counter efficiencies, computer dead times, slit accidentals, etc., to this accuracy with count rates that varied by a factor of >100 would have been much more difficult.

The deviations of the spectra from each pair of fields from their common fit are a measure of some of the systematic errors in the shape determination, these deviations along with straight lines fit to them are shown in fig. 48. If both fields measured the same shape for the overlapping momentum regions the lines should be horizontal at 0%. For the two highest momenta overlap regions (between B=3.39,2.4 and B=2.4,1.7) the best fit straight line shown does not give a statistically significant improvement over a horizontal line at 0%, thus there is no evidence for systematic disagreement at the few percent level. For the overlap between B=1.7 and 1.33 the line shown does represent a 1σ improvement, however the scatter in the data is large and the total effect is only a few percent. The lowest field overlap between B=1.33 and 0.98 does show a definite deviation at the 4% level (this deviation probably arises from a slight position dependence of the efficiency correction ε already discussed). We shall therefore assign errors of 2% to $R_{3.39\leftrightarrow 2.4}$ and $R_{2.4\leftrightarrow 1.7}$, 3% to $R_{1.7\leftrightarrow 1.33}$, and 6% to $R_{1.33\leftrightarrow .98}$ (errors in the shape are already included in the large error assigned to ε).

The different field measurements were then combined and corrected for the spectrometer efficiency. The final spectrum is shown in fig. 49. To facilitate the comparison to theory discussed in the next chapter the spectrum above p = 2.5 MeV was fitted to a function equal to eq. 13 with $n = 4$ plus a small flat background. The fit parameters are a_0 = 9.3964, a_1 = -0.6489, a_2 = -0.0413, and a_3 = -0.00351. The deviations from this fit are shown in fig. 50 along with the total errors in the spectrum discussed below. The fit is a good representation of the data over the range of interest. The fit value of the background, 0.12/channel in the units of fig. 49 (5.7 x 10^{-5} e^-/MeV·fission when normalized to agree with the calculation of Vogel[43] at p = 2.5 MeV/c), translates to about 0.2 $min.^{-1}$ into the whole spectrum over the time measured. This is too high to be given by the measured background (3 counts/hour into the whole spectrum). These events may be caused by large angle scattering in the spectrometer, however it is possible that the spectrum changes shape at ~8 MeV/c. We shall assume that these do represent background, the signal/noise is then ~ 16 at 7.5 MeV/c, ~ 7 at 8 MeV/c, and 2.5 at 8.5 MeV/c. Tabulated values for the spectrum are given along with errors in Table 5. The errors in the spectrum are calculated assuming that the normalization to the theoretical spectrum will be done at 2.5 MeV/c, i.e., at the lower end of the 1.33 kG spectrum. In addition to the error in ϵ already given, we will assume a 1.5% error in the total spectrometer linearity/momentum bite; this should be added for each momentum bite. It is thus 6% for the highest momenta. The errors in the R_j consist of the systematic errors discussed above and a statistical error that is at most ~1.5%. The statistical errors in the counts are ~2% at 3 MeV/c, rising to ~3% at 6 MeV/c, ~6% at 7 MeV/c and 13% and 8 MeV/c. The total error at each momentum is obtained by adding the individual errors in quadrature, the systematic, statistical, and total errors are shown on fig. 50 and in Table 5.

CHAPTER 4

Comparison to Theory and Conclusions

4.1 Comparison to Theory and Earlier Experiments

A theoretical β spectrum for ^{252}Cf was generated by Vogel[43] in 1982 using the same technique as summarized in section 1.4.1 and given in detail in references 14 and 21, the calculation gives a total yield of 6.21 β^-/fission. The resulting spectrum is shown in fig. 51 along with the calculation by Kopeikin[33] discussed in section 1.5. As was the case in the other nuclei discussed in Chapter 1, the former predicts a softer spectrum at all momenta than the latter. Since the experiment described in this thesis measures only the shape of the ^{252}Cf spectrum, the two theoretical and the experimental spectra are normalized to agree at 2.5 MeV/c (this requires a 3% change in Kopeikin's relative to Vogel's calculation). The ratios of the two calculations to the experimental result up to 7.5 MeV/c are shown in fig. 52. As in the other fissioning nuclei measured by Schreckenbach[18,28,29,30], the experiment produces a softer spectrum than these calculations. When making comparisons between the calculations and experiments one should keep in mind that the spectra change by 4 orders of magnitude in the energy interval from 2-8 MeV. That one can explain the data at all is thus a major accomplishment.

4.1.1 Comparison With Other Fission Spectra and Discussion of Deviations

Fig. 53 shows the ratio of the theoretical spectra of Kopeikin[33,17] to the present experiment and the experiments of Schreckenbach et al.[18,28] (all renormalized to agree at 2.5 MeV/c). There is a clear systematic trend in the results; the softer the β spectrum the greater the disagreement. A similar plot for the smaller deviations from the calculations of Vogel[43] and Vogel et al.[21] is shown in fig. 54; a systematic

trend is not as pronounced. The deviations from Vogel's calculation for ^{252}Cf would resemble those for the other nuclei more closely if we had elected to normalize the spectra to agree at 3 MeV/c. This would lower the ratio of Vogel's calculation to the experiment by 0.05 (which is within errors) at all momenta. The deviations for all the nuclei would then be similar up to ~5 MeV/c.

The major reason that Kopeikin's calculations[17,33] deviate from the experiments is almost certainly the simplified scheme used to predict the branching ratios $b_{n,i}(E_o^i)$ for the unknown nuclei (see page 7). In Vogel's calculations[21,43] at 6 MeV the unknown nuclei contribute 23%, 36%, 46%, and 60% of the electrons for ^{235}U, ^{239}Pu, ^{241}Pu, ^{252}Cf. If we assume that roughly the same input data were used we can see from fig. 53 that the overestimation of the β rate by Kopeikin's calculation is approximately proportional to the contribution from unknown nuclei, as would be expected from the underestimation of the branching to highly excited states in his single level scheme for $b_{n,i}(E_o^i)$.

The differences between the calculations of Vogel[21,43] and the experiments are not as easily explained. Possible sources are errors in the input data (fission yields, Q-values, and $b_{n,i}(E_o^i)$) used for the β decays or in the approximation scheme used for $b_{n,i}(E_o^i)$. The higher energy part of the spectrum where the discrepancies become serious is due to a relatively few neutron-rich nuclei with high Q-values. In ^{252}Cf (^{235}U) essentially all the β rate at 6.0 MeV comes from 28 (25) nuclei. Half of the ^{252}Cf rate at 6 MeV comes from just 6 nuclei, 5 of which have unknown decay schemes. If the input data are in error for only a few of these it can have a substantial effect on the spectrum. This can be seen in references 14 and 21, where the difference of 15% at $E_{\bar{\nu}}$ = 5.5 MeV resulted mainly from changes in the ground state branching ratios in only 4 fission fragments. As a demonstration that errors in the values used for $b_{n,i}(E_o^i)$ could produce the observed deviations, the β spectrum

was recalculated using Vogel's code modified in such a way that the 5 nuclei mentioned above (^{102}Nb, ^{104}Nb, ^{106}Tc, ^{108}Tc, and ^{114}Rh) are forced to have β decay only to very highly excited states in the daughter. The deviations for this spectrum are shown in fig. 54; the spectrum reproduces the experimental spectrum to within 5% for $E_\beta < 7.0$ MeV. The Q-values for most of these neutron rich nuclei are obtained from systematics and are poorly known. The values used in the initial calculation (from reference 15) were significantly different than the more recent values[56] for most of the 28 nuclei mentioned above, the average (largest) difference was 390 keV (1.6 MeV). While the initial spectrum and a spectrum calculated with the more recent values agreed to with 5% at all energies (due to a chance cancellation of larger errors), it is still possible that errors in these Q-values could explain part of the deviations. Clearly more work will be necessary to identify the problem.

4.1.2 Comparison to Borovoi et al.[27,35]

There is also a strong disagreement between the results of this work and the experiment of Borovoi et al.[35] discussed in section 1.5. Since their publication does not give tabulated values for the spectrum an exact deviation plot cannot be constructed. However it is clear from inspection of fig. 17 that the experimental deviations will closely follow the deviations from the Kopeikin calculation given above. The ratio of the experimental results of Borovoi et al.[27] for ^{235}U and ^{239}Pu to the results of Schreckenbach et al.[18,28] are shown in fig. 55 along with ratios to Kopeikin's[17,33] calculations for these nuclei and ^{252}Cf from fig. 53. The same systematic trend exists for the experiments of Borovoi et al. as for the calculations of Kopeikin, the softer the spectrum the greater the deviation from the other experiments. The reasons cited on page 12 to explain these differences (error in the energy calibration and detector response function) will cause a greater error in a faster falling spectrum. It is curious, however, that the errors in the theoretical and the

experimental spectra seem to be roughly equal.

4.1.3 Ratios of Spectra from Different Isotopes

It is also interesting to compare the ratios of the spectra from different fissioning nuclei for the different theories and experiments. The ratios of the ^{252}Cf spectra to the ^{235}U spectra are shown in fig. 56, while the ratios of the spectra from the plutonium isotopes to the ^{235}U spectra are shown in fig. 57 (taken from ref. 30). The qualitative shape of the ratio of the present experiment to the experiment of Schreckenbach for ^{235}U matches the shape of the ratios for their measurements of the plutonium isotopes to ^{235}U. Inspection of fig. 56 shows, first of all, that the ^{252}Cf spectrum is much softer than the spectra of the other fissioning nuclei. This fact depends on the fission yields (see fig. 1) and is qualitatively supported by all available calculations and experiments. Figs. 56 and 57 also show that the ratios (^{252}Cf,^{239}Pu,$^{241}Pu/^{235}U$) of the calculated spectra agree with each other and with the ratios of the experimental spectra better than they agree for the individual nuclei. As discussed in the appendix, this fact is exploited by the Gösgen group to minimize the effect of errors in the calculations on the neutrino oscillation experiment. The ratio of this experiment to the Schreckenbach measurement of ^{235}U agrees with the ratio from the calculations, including the calculation by Kopeikin, better than the ratio of this experiment to the measurement of the ^{235}U spectrum by Borovoi.

4.2 Future Plans

The measurement described in this thesis and the previous experiment by Borovoi et al. both determine only the relative shape of the β spectrum from ^{252}Cf. However the absolute normalization of this spectrum is also very important. In fact one of the main advantages of knowing the reactor $\overline{\nu}_e$ spectrum, the ability to exclude neutrino oscillations with large Δm^2 (as discussed in the appendix), depends

on the knowledge of the absolute normalization. We are therefore determining the absolute normalization of the ^{252}Cf spectrum by comparing it to a ^{90}Sr source of known intensity. Unfortunately, while the spectrometer and electronics are optimized to minimize variation of the efficiency with momentum, the overall efficiency of the electronics, computer, and various cuts is not as easily determined, and may vary with time and with count rate. An effort is currently underway to quantify these effects, and it is hoped that the overall normalization can be determined to <8% before these results are published.

We also plan to examine in more detail the branching ratios and Q-values for the decays with non-negligible yield above 5 MeV in the hope of better understanding the deviations of the predictions of the β spectra for the various fissioning isotopes from the experiments. The ^{252}Cf β spectrum has the largest deviations of any of the measured isotopes; it therefore seems to be the strongest test of the various calculations. For this reason it would be very interesting to see a calculation of the ^{252}Cf spectrum using the most recent code of Klapdor et al.[16] which has had success in predicting the spectra for the other isotopes. It is hoped that such a calculation will become available in the near future.

4.3 Conclusions

In conclusion, this experimental determination of the ^{252}Cf spectrum strongly disagrees with the predicted spectra discussed in Chapter 1 and the experimental spectra of Borovoi et al.[27,35] We find a softer spectrum more consistent with the spectra measured by Schreckenbach et al.[18,28,29,30] in other fissioning nuclei. The deviations of the predicted ^{252}Cf spectrum of Kopeikin[33] and the experimental ^{252}Cf spectrum of Borovoi et al. from the results of this work follow the same systematic trend as the deviation of their work in other nuclei from the measurements of

Schreckenbach et al., further supporting these softer spectra. A more quantitative test of this agreement would be a comparison of the spectrum measured for ^{252}Cf in this experiment to a calculation made using the method of Klapdor and Metzinger, or to an improved calculation using Vogel's code which include changes in the input data necessary to reproduce the spectra of the other fissioning nuclei.

APPENDIX

Neutrino Oscillations

A.1 What are Neutrino Oscillations?

Neutrinos as currently observed are characterized by a flavor l (l=e,μ,τ), these neutrinos are weak eigenstates. If there are mass terms in the Lagrangian, and if these mass terms are non-diagonal in l, then the flavor eigenstates are not the same as the mass eigenstates. The mass eigenstates, which we shall denote $\nu_{1,2,3,...}$ are related to the flavor eigenstates by a unitary transformation:

$$\nu_l = \sum_{i=1}^{N} U_{li}\, \nu_i \tag{A1}$$

where N is the number of families. An analogous situation exists in the quark sector, where the weak isospin doublets are:

$$\begin{pmatrix} u \\ d' \end{pmatrix}_L \qquad \begin{pmatrix} c \\ s' \end{pmatrix}_L \qquad \begin{pmatrix} b \\ t' \end{pmatrix}_L$$

where u,b,s,c,b,t are the strong interaction eigenstates and d′,s′,t′ are the states coupled to the weak current. For the case of four quarks, they are related by:

$$\begin{pmatrix} d' \\ s' \end{pmatrix} = \begin{pmatrix} \cos\theta_c & \sin\theta_c \\ -\sin\theta_c & \cos\theta_c \end{pmatrix} \begin{pmatrix} d \\ s \end{pmatrix} \tag{A2}$$

where θ_c is the Cabibbo angle. For the case of two families, a similar matrix could mix the neutrinos:

$$\begin{pmatrix} \nu_e \\ \nu_\mu \end{pmatrix} = \begin{pmatrix} \cos\theta & \sin\theta \\ -\sin\theta & \cos\theta \end{pmatrix} \begin{pmatrix} \nu_1 \\ \nu_2 \end{pmatrix} \tag{A3}$$

where θ is an angle parameterizing the degree of mixing (this is also approximately

valid for more than two families when one neutrino has a mass much larger than the others). For the case of six quarks or three families of leptons the analysis becomes more complicated, the matrix U becomes a Kobayashi-Maskawa matrix with four parameters (three mixing angles and one phase), and the discussion becomes more cumbersome.

If the masses of the neutrinos are small compared to the their energies, the above mixing will lead to neutrino oscillations. Neutrinos emitted in some weak process start in a pure flavor state ν_l, corresponding to a linear superposition of mass states ν_i. The mass states, having different momenta because of their different masses, will propagate with different phases. Therefore the relative amplitudes of the ν_i will change with distance from the source, which leads to an admixture of different flavor neutrinos. For neutrinos with momentum p the probability of finding a neutrino of flavor l' from a source of flavor l after a time t is given by[3]:

$$P(\nu_l \rightarrow \nu_{l'}) = \sum_{i=1}^{N} \left[|U_{li}|^2 |U_{l'i}|^2 + \sum_{j \neq i} U_{li} U_{lj} U_{l'i}^* U_{l'j}^* \exp\left(-i \frac{m_i^2 - m_j^2}{2p}\right) t \right] \qquad (A4)$$

From this one can obtain the following useful expression for the two flavor case[4]:

$$P(\nu_l \rightarrow \nu_{l'}) = \sin^2 2\frac{\theta}{2} \left[1 - \cos\left(\frac{2.53\,\Delta m^2 L}{E_\nu}\right) \right] \qquad (A5)$$

and

$$P(\nu_l \rightarrow \nu_l) = 1 - P(\nu_l \rightarrow \nu_{l'}) \qquad (A6)$$

where L is the distance from the source in meters, E_ν is the neutrino energy in MeV, $\Delta m^2 = |m_1^2 - m_2^2|$ is the mass squared difference in $(eV)^2$, and θ is the angle in eq. A3. This equation is only valid for sources small compared to the wavelength of

oscillations and within a certain coherence length of the source[1], at greater distances or for larger sources the oscillations wash out leaving some constant fraction of ν_l in the ν_l flux. Analogous equations for the three flavor case have been derived[5], and a quantitative analysis assuming six leptons of the experiments described below has been done[44]. To keep the discussion tractable we will consider the two flavor case, keeping in mind that nature may be more complicated.

From eq. A5 we see that in the two flavor case there are two parameters that can be measured in a neutrino oscillation experiment; $\sin^2 2\theta$, which gives the amplitude of the oscillations, and Δm^2, which determines their wavelength. The ratio L/E_ν varies with the type of experiment being considered, the larger it is the more sensitive the experiment is to small Δm^2. The Davis experiment could be considered a neutrino oscillation experiment with $L/E_\nu \approx 10^{11}$, but uncertainties about the initial flux make the interpretation difficult. Tests have been done using neutrinos from high energy cosmic ray interactions in the atmosphere ($L/E_\nu \approx 100$-1000), but uncertainties about the initial flux and limited statistics prevent good limits from being set. The terrestrial experiments with the largest values of L/E_ν are done at nuclear reactors, here $L/E_\nu \approx 1$-10. Neutrinos from particle accelerators give less sensitivity for Δm^2, with $L/E_\nu \approx 0.1$-0.01, but as we will discuss next, they can test for much smaller values of $\sin^2 2\theta$.

A.2 ACCELERATOR BASED NEUTRINO OSCILLATION EXPERIMENTS

There were a large number of searches at accelerators in the late 70's and early 80's, most of these were done by analyzing the data from other neutrino experiments that were not necessarily optimized for looking for oscillations. These experiments[5] produced conflicting results which have been largely supplanted by more recent experiments. We shall confine our discussion to the newer experiments, descriptions

of the older ones can be found in the literature.[2,5]

Accelerator neutrinos originate from the decay of secondary particles created by beam interactions. Most experiments with these neutrinos naturally divide into two classes; disappearance experiments and appearance experiments. In the first type one looks for $P(\nu_l \rightarrow \nu_l) < 1$, either by measuring the flux of a given type of neutrino at two places in the beam or by knowing the initial flux. In the second type one samples a particular channel $P(\nu_l \rightarrow \nu_{l'})$ by looking for the appearance of neutrinos of the "wrong" flavor l' in a beam of type l. This last type of experiment, at least in principle, has the ability to measure very small values of $\sin^2 2\theta$, as the appearance of a single $\nu_{l'}$ in a pure beam of ν_l would signal oscillations. In practice contamination of the beam by $\nu_{l'}$ and background events reduce the sensitivity somewhat, but these experiments still give the best limits on $\sin^2 2\theta$.

Two recent CERN disappearance experiments[45] have used charged current events induced by ν_μ's from decay of secondary π's and K's to look for $\nu_\mu \rightarrow$ anything. Each placed a small detector near the target and a larger one farther down the beam, thus reducing systematic errors associated with beam flux. The CDHS collaboration measured 22,000(near detector)/3300(far detector) events from ν_μ with $E_\nu \approx 3$ GeV, while the CHARM collaboration observed 2043/270 events with $E_\nu \approx 1.3$ GeV. When scaled for detector efficiency and cross sections these fluxes agree, providing no evidence for neutrino oscillations. Limits on oscillation parameters provided by these experiments are shown in fig. 58.

Appearance experiments have also been done using the ν_μ beam from the decay of secondaries by looking for more ν_e induced events than would be caused by the few percent admixture of ν_e's from $K^+ \rightarrow \pi^0 e^+ \nu_e$ and $\pi^+ \rightarrow \nu_\mu \mu^+ \rightarrow e^+ \nu_e \overline{\nu}_\mu$. An experiment at CERN using the BEBC Detector[4] looked at the ratio of the number of events from $\nu_e N \rightarrow e^- X$ to the number of events from $\nu_\mu N \rightarrow \mu^- X$ by identifying the lepton in

the final state. After applying cuts and correcting for detector response they found 2 events of the first type and 344 of the second, in good agreement with the ratio expected from beam contamination. The best limits from this type of experiment have been obtained by a group from BNL using the fine grain calorimeter from the E734 experiment[46]. They measure the ratio of the number of $\nu_e n \rightarrow p e^-$ events to $\nu_\mu n \rightarrow p \mu^-$ events as a function of energy. Their detector is larger and closer to the target than the BEBC detector, giving them higher count rates. In addition, they have a larger acceptance for ν_e events than ν_μ events, and they used a larger data sample for the ν_e events, thus giving them a larger fraction of ν_e events and therefore smaller statistical errors. Figure 2 shows their data (points) plotted against the expected yield from contaminant ν_e's, the agreement is quite good. The limits on oscillation parameters from this experiment and from the BEBC experiment are shown in fig. 59.

Also shown in fig. 59 are the results of a similar experiment with the PS-191 detector at CERN[4]. This detector is a fine grain calorimeter of a different type than the BNL detector, and was illuminated by the same beam as the BEBC detector. However, in this case positive evidence for neutrino oscillations was found. After cuts and corrections they see 24 ν_e and 593 ν_μ events. They expect 709 ν_μ events, so they adopt the figure 650 ± 65, and from this get a value of (0.037 ± 0.009) for the ratio of ν_e events to ν_μ events, whereas they expect to see 0.008. The range of oscillation parameters which could cause this discrepancy are enclosed in the contour in fig. 59, they are clearly in conflict with the other experiments. The cause of this disagreement is not known. The detector has been moved to BNL in the hope that better statistics will shed light on the problem, but as of yet no new data have been published.

Neutrinos from the LAMPF beam stop offer the possibility of probing still smaller values of $\sin^2 2\theta$ for the channels $\nu_x \rightarrow \overline{\nu}_e$. The primary proton beam energy of 800 MeV is below kaon production threshold, while π^- and μ^- are strongly absorbed by the nuclei in the beam stop. Thus the dominant sources of neutrinos, $\pi^+ \rightarrow \mu^+ \nu_\mu$ and $\mu^+ \rightarrow e^+ \nu_e \overline{\nu}_\mu$, produce nearly equal numbers of ν_e, ν_μ, and $\overline{\nu}_\mu$, with very little contamination of $\overline{\nu}_e$ ($\lesssim 10^{-4}$). The reaction $\overline{\nu}_e p \rightarrow e^+ n$ can then serve as a test for neutrino oscillations. Several experiments have or are going to attempt this[45]. E225 has looked for $\overline{\nu}_e$ induced events in their 14 ton scintillator-flashtube sandwich detector as a by-product of their search for ν_e-e elastic scattering. After cuts they see -1.3 ± 7.9 events where they expect 930 ± 162 events if all $\overline{\nu}_\mu$ oscillated into $\overline{\nu}_e$. Their limits on oscillation parameters are shown in fig. 59. A large, portable H_2O/D_2O Cerenkov/drift chamber detector has been constructed specifically to look for oscillations (E645) and should begin taking data soon. Its sensitivity should rival the BNL experiment mentioned above. Even more ambitious experiments are planned for the future which could eventually reach $\Delta m^2 \approx 0.001$ eV^2 and $\sin^2 2\theta \approx 10^{-6}$.

A.3 REACTOR BASED NEUTRINO OSCILLATION EXPERIMENTS

Nuclear reactors are a powerful source of $\overline{\nu}_e$, with total outputs of $\approx 10^{20}$ $\overline{\nu}_e$/sec from the β decays of fission fragments. The $\overline{\nu}_e$ energy is $\approx$ 0-8 MeV, which is below μ-production threshold, thus only disappearance tests of the type $\overline{\nu}_e \rightarrow \nu_x$ are possible. This limits the sensitivity of reactor experiments to $\sin^2 2\theta$, however the high value of L/E_ν (and the high fluxes necessary because of the low cross-section at low E_ν) allow greater sensitivity to Δm^2. With the exception of the first experiment mentioned below, all the reactor oscillation experiments which have been done have looked at the inverse β decay reaction:

$$\overline{\nu}_e + p \rightarrow e^+ + n \qquad \text{(A6)}$$

The low value of the cross section for this reaction ($\sigma_t = 64.2\times10^{-44}\,cm^2$/fission when averaged over the $\overline{\nu}_e$ spectrum from ^{235}U)[21] limits the values of L which are practical. As the detector is moved farther from the reactor the signal is eventually swamped by background from cosmic ray induced events and natural radioactivity in the detector and in the shielding, thus limiting the the values of Δm^2 which can be tested.

There are two basic ways to look for oscillations at a reactor using reaction A6. The first requires that one know the energy spectrum of $\overline{\nu}_e$ (denoted $N_{\overline{\nu}_e}(E_{\overline{\nu}})$) coming from the reactor. This can be compared to a measured value for $N_{\overline{\nu}_e}(E_{\overline{\nu}})$ obtained by measuring the energy spectrum of positrons from A6, correcting for detector efficiency, background, cross sections, etc., and using the relation:[47]

$$E_{\overline{\nu}} = E_{e^+} + 1.804\,MeV + E_r \qquad \text{(A7)}$$

where E_r is a correction for neutron recoil of the order of 10 keV. Any deviation where there were fewer $\overline{\nu}_e$ measured than expected would then be a signal for neutrino oscillations. The second way requires the measurement of $N_{\overline{\nu}_e}(E_{\overline{\nu}})$ at two or more different distances from the reactor. After correcting for different solid angles and perhaps different backgrounds the spectra are compared, any differences once again signal oscillations.

The disadvantage of the first method is the necessity of knowing $N_{\overline{\nu}_e}(E_{\overline{\nu}})$ in advance. The second method in principle avoids this difficulty, however, in practice some ability to predict $N_{\overline{\nu}_e}(E_{\overline{\nu}})$ is still necessary. This is due to the mix of fissioning isotopes present in a reactor. Each different fissioning isotope produces a different $\overline{\nu}_e$ spectrum, and during the fuel cycle of the reactor the mix of isotopes

changes. Thus the total $\overline{\nu}_e$ spectrum of a reactor is to some extent time-dependent. A measurement made by moving a single detector to two positions must be corrected for this effect, and this requires knowledge of $N_{\overline{\nu}_e}(E_{\overline{\nu}})$ for each isotope. The first method is also the only way to test for large values of Δm^2, where the mixing length becomes comparable to the size of the reactor core and detector. For these conditions $N_{\overline{\nu}_e}(E_{\overline{\nu}})$ will be the same for any detector distance. Only the overall normalization will change, which is only detectable by the first method. For these reasons it is desirable to predict $N_{\overline{\nu}_e}(E_{\overline{\nu}})$. We will discuss these predictions after a brief survey of the experiments to date.

A.3.1 The Deuteron Experiment

One oscillation experiment has been done at reactor which does not use reaction A6. This is the experiment of Reines et al[48] at the Savannah River reactor which instead looks at the relative rates of the deuteron reactions:

$$\begin{aligned} \overline{\nu}_e + d &\rightarrow n + n + e^+ \quad \text{(ccd)} \\ \overline{\nu}_e + d &\rightarrow n + p + \overline{\nu}_e \quad \text{(ncd)} \end{aligned} \tag{A8}$$

where ccd indicates a charged-current deuteron reaction and ncd a neutral current deuteron reaction (reaction A6 is often indicated as ccp). The advantage of using these reactions is that the ncd reaction will go independent of the flavor of the neutrino, thus it does not depend on oscillations. It can therefore be used to monitor the flux, helping to control systematic errors and making the experiment less dependent on predictions of the reactor spectrum. This independence is lessened by the fact that these reactions have different thresholds (E_T(ccd)= 4.0 MeV, E_T(ncd)= 2.3 MeV). These reactions also have low cross sections relative to reaction A6($\sigma_{ccd} \approx 0.02\,\sigma_{ccp}$, $\sigma_{ncd} \approx 0.05\,\sigma_{ccp}$). The experiment measured the relative rates of the ncd and ccd processes by observing neutrons produced in 268 kg. of D_2O with ^3He

counters surrounded by a liquid scintillator anti-coincidence shield. After correcting for backgrounds and inefficiences the experimental rates gave $r_{exp} = <\sigma_{ccd}> / <\sigma_{ncd}> = 0.167 \pm 0.093$, where the predicted value assuming the standard model and using the reactor $\overline{\nu}_e$ spectra discussed below is $r_{theor} = 0.42 - 0.44$. The initial explanation of this result in terms of neutrino oscillations has been questioned by many authors[5] and to some degree retracted[48], and is in any case difficult to reconcile with the ccp results discussed below. It is therefore hard to consider this experiment to be evidence for oscillations.

A.3.2 Inverse β Decay Experiments

To date there have been 7 reactor experiments looking for oscillations using reaction A6. Results at more than one position have been reported by a Caltech-SIN-TUM collaboration using the power reactor at Gösgen in Switzerland[47] and by a group using the Bugey reactor in France[49]. These experiments will be discussed in more detail below. Two experiments are currently in progress using gadolinium doped liquid scintillator detectors. The gadolinium serves to capture the neutron produced in reaction A6, the event signature is then a prompt pulse from the e^+ followed by a delayed pulse from the capture γ rays. The mobile neutrino oscillation experiment at Savannah River has reported results[50] at a distance of 18.3 m from the reactor core but has not yet analyzed them in terms of neutrino oscillations. An experiment at Rovno in the Soviet Union has measured the rate at a distance of 18 m[51], however their derived limits on oscillation parameters are poor compared to those of the Gösgen experiment. This is in part due to the confusion concerning $N_{\overline{\nu}_e}(E_{\overline{\nu}})$ which is discussed in section 1.4.

A forerunner of the current Gösgen and Bugey experiments was performed at the Institut Laue-Langevin (ILL) high-flux reactor[52] using the same type of detector as will be described in section A.3.3. They observed 4890 ± 180 events at a distance

of 8.76 m from the reactor core. The observed positron spectrum produces no statistically significant evidence for oscillations when compared to the predicted spectrum based on the measurement by Schreckenbach[18] which is discussed in section 1.4. The values of Δm^2 and $\sin^2 2\theta$ excluded by this experiment are shown in fig. 60. They are consistent with the Gösgen limits but not as stringent. The other two experiments were performed at the Savannah River reactor and do not produce much in the way of useful limits. The early experiment of Nezrick and Reines[53] has poor statistics and a uncertain background. The other data come as a byproduct of a search for neutrino-electron scattering and are poorly documented[54].

A.3.3 The Gösgen *Experiment*

The Gösgen experiment[47] measured the rate for reaction A6 at distances of 37.9, 45.9, and 64.7 m from the core of the 2800-MW (thermal) reactor. The detector (fig. 61) was $\approx 1\ m^3$ in size and consisted of alternating layers of liquid scintillator cells and ^{3}He wire chambers. The liquid scintillator served both as the target and as the detector for the emitted positrons. The scintillator was subdivided into 30 cells, 6 to a layer, with phototubes at each end. The positron's position along the cell was determined with a resolution of about 6 cm. by the time difference between the phototube pulses. The target cell energy resolution was 18% FWHM at $E_e^+ = .91$ MeV. Energy calibration was done using the Compton edges from the 4.44 MeV γ from $^{12}C^*$, the 2.22 MeV γ from neutron capture on protons, and the 1.16 MeV γ from ^{65}Zn. The wire chambers were multi-wire proportional counters filled with 95% ^{3}He - 5% CO_2. After a mean diffusion time of $\approx 150\ \mu$sec the neutrons from A6 capture by the reaction $n + {}^3He \rightarrow p + t$. This produced a count in the chamber whose horizontal position was determined by charge division and whose vertical position was determined by comparing adjacent wires. The efficiency of the wire chambers for neutrons was determined using an internal neutron source.

The entire detector was surrounded by passive shielding of concrete, iron, water, and B_4C and a 12-cm-thick liquid scintillator active anti-coincidence veto. Fast neutron backgrounds were rejected by using pulse-shape discrimination on the target cell output, and reactor associated background was shown to be negligible. Besides the PSD cut, cuts were made on the wire-chamber energy, various timing conditions to ensure a correlated positron and neutron without a cosmic ray, and a requirement that the target cell and wire chamber counts be within a specified distance of each other. The total efficiency was measured and shown to be stable over the 4 year measurement period. A reactor off spectrum was taken at each distance and subtracted. Figure 62 shows the reactor on and reactor off spectra at each position. A total of 10,909 ± 220 events were observed at position I, 10,605 ± 190 at position II, and 8787 ± 325 at position III. The reactor on - reactor off spectra are shown in fig. 63.

Also shown in fig. 63 are the results of two different analysis of the data. Analysis A relied almost solely on the measured spectra, with only small corrections applied for changes due to reactor composition (as discussed above, these require knowledge of $N_{\bar{\nu}_e}(E_{\bar{\nu}})$, but these corrections are $\lesssim$ 5%) and detector efficiency. The neutrino spectrum was parameterized as an exponential of a power series, and a fit was made to see if a single spectrum could fit all three positions. The solid line in fig. 63 shows the results of this fit, the agreement is quite good and no evidence is seen for oscillations. For analysis B the spectra which should be measured at the three positions were predicted based on the reactor neutrino spectrum derived from the work of Schreckenbach[18] and then compared to the experimental results. The dotted lines in fig. 63 show the predicted spectra, once again agreement is excellent and no evidence is seen for oscillations. The limits on oscillation parameters derived from these two analyses are shown in fig. 64, the solid line is the result of analysis

A, the dotted line the result of analysis B. This shows the need for a reliable prediction of $N_{\bar{\nu}_e}(E_{\bar{\nu}})$, the best limits for all parameters and the only limits for large Δm^2 are produced by analysis B.

A.3.4 The Bugey Experiment

A similar experiment was carried out using a somewhat simplified version of the Gösgen detector (no position information from the wire chambers) at distances of 13.6 and 18.3 m from the core of the 2800-MW power reactor at Bugey in France. Here the spectrum was first measured at position 1 (13.6 m), then at position 2, then again at position 1. While the two position 1 measurements agree, the measured flux scaled for solid angle at position 2 does not. Fig. 65 shows the measured spectra for the two positions and the spectra predicted as for Gösgen. There is a clear discrepancy in the position 2 spectrum. The ratio of position 1 to position 2 corrected for solid angle and core composition is shown in fig. 66. The Bugey collaboration interprets this as evidence for neutrino oscillations. The allowed oscillation parameters are shown in fig. 64 along with the limits from Gösgen. The Bugey result is obviously in conflict with the Gösgen result, especially when the predicted reactor spectrum is used. In fact, there does not seem to be any reactor neutrino spectrum which is simultaneously consistent with both experiments[24]. A simple demonstration of this can be seen in fig. 65. If sufficient neutrinos oscillated away between the two positions to explain the discrepancy, still more must have oscillated away between the core and position 1. However the position 1 measurement is in agreement with the predictions, so the spectrum leaving the core must have had more neutrinos than predicted.

In conclusion, there exists an unsettled discrepancy between the major reactor neutrino oscillation studies. The Gösgen and ILL results agree with each other and with the theoretical prediction of the reactor spectrum for the case of no oscillations.

The Bugey data disagree, and no explanation other than neutrino oscillations has been found. However, for the Bugey data to be correct the predicted reactor spectrum would have to have serious errors. Thus, any information about the predicted spectrum has a direct bearing on this conflict, and independent confirmation of the predictions would go far towards clarifying the situation.

REFERENCES

1. P.H. Frampton and P. Vogel, Phys. Rep. **82**, No. 6 (1982) 339-388
2. S.M. Bilenky and B. Pontecorvo, Phys. Lett. **95B** (1980) 233
3. F. Boehm and P. Vogel, Ann. Rev. Nucl. Part. Sci. **34** (1984) 125-153
4. J.L. Vuilleumier, to be published in Rev. Prog. Phys.
5. F.W. Bullock and R.C.E. Devenish, Rep. Prog. Phys. **46** (1983) 1029-1191
6. H. Fritzsch and P.Minkowski, Phys. Rep. **73**, No. 2 (1981) 67-173
7. G. Blewitt et al., Phys. Rev. Lett. **54** (1985) 22
8. S.M. Faber and J.S. Gallagher, Ann. Rev. Astron. Astrophys. **17** (1979) 135
9. R.G.H. Robertson, LANL Preprint LA-UR-86-1828, (1986)
10. J.K. Rowley et al., AIP Conf. Proc. **126** (1985) 1
11. J. Bahcall et al., Astrophys. Jour. Lett., **292** (1985) L79
12. S.P. Mikheev and A. Yu. Smirnov, Sov. Jour. Nucl. Phys. **42**(6) (1985) 913
    (Yad. Fiz. **42** (1985) 1441-1448
    H. A. Bethe, Phys. Rev. Lett. **56** (1986) 1305
13. K. Schreckenbach, Institut Laue-Langevin Technical Report 84SC26T, Nov. (1984)
14. B.R. Davis et al., Phys. Rev. C **19** (1979) 2259
15. Fission Product Library of the Evaluated Nuclear Data File, Version V. Available from, and maintained by, the National Nuclear Data Center at the Brookhaven National Laboratory.
16. H.V. Klapdor and J. Metzinger, Phys. Lett. **112B** (1982) 22
    H.V. Klapdor and J. Metzinger, Phys. Rev. Lett. **48** (1982) 127
17. V.I. Kopeikin, Sov. Jour. Nucl. Phys. **32**(6), (1980) 780
    (Yad. Fiz. **32** (1980) 1507-1513)
18. K. Shreckenbach et al., Phys. Lett. **160B** (1985) 325
19. F.T. Avignone, Phys. Rev. D **2** (1970) 2609
20. F.T. Avignone and Z.D. Greenwood, Phys. Rev. C **22** (1980) 594

21. P. Vogel et al., Phys. Rev. C **24** (1981) 1543

22. K. Aleklett and G. Nyman, Nucl. Phys. **A246** (1975) 424-444

23. C.O. Muehlhause and S. Oleksa, Phys. Rev. **105** (1957) 1332

24. R.E. Carter et al., Phys. Rev. **113** (1959) 280

25. J.W. Kutcher and M.E. Wyman, Nucl. Sci. and Eng. **26** (1966) 435

26. N. Tsoulfanidis et al., Nucl. Sci. and Eng. **43** (1971) 42

27. A.A. Borovoi et al., Sov. J. Nucl. Phys. **37**(6), (1983) 801
(Yad. Fiz. **37** (1983) 1345-1350
available in more complete form as ORNL reprint ORNL-tr-4842

28. F. von Feilitzsch et al., Phys. Lett. **118B** (1982) 162

29. K. Shreckenbach et al., Phys. Lett. **99B** (1981) 251

30. K. Shreckenbach et al. at the Int. Symposium on Weak and Electromagnetic Interactions in Nuclei, Heidleberg, 1-5 July 1986. Available as ILL preprint SP.86SC5056

31. W. Mampe et al., Nucl. Inst. and Meth. **154** (1978) 127

32. U. Kayser, Z. Phys. A - Atoms and Nuclei **322** (1985) 529-530

33. V.I. Kopeikin, Sov. Jour. Nucl. Phys. **32**(1) (1980) 33
(Yad. Fiz. **32** (1980) 62-29)

34. R.A Knief, B.W. Wehring, and M.E. Wyman, Nucl. Sci. and Eng. **53** (1974) 47

35. A.A. Borovoi et al., Sov. Jour. Nucl. Phys. **32**(5) (1980) 621
(Yad. Fiz. **32** (1980) 1203)

36. A. Heath and G.T.Garvey, Phys. Rev. C **31** (1985) 2190

37. J.D. Jackson, Classical Electrodynamics, second edition, John Wiley and Sons, Inc., New York (1975)

38. Tatsuo Tabata, Phys. Rev. **162** (1967) 336

39. H.Behrens and J.Janecke, Numerical Tables for Beta-Decay and Electron Capture, edited by H.Schopper, Springer-Verlag, New York (1969)

40. D.H.Wilkinson and B.E.F.Macefield, Nucl. Phys. **A158** (1970) 110

41. F.P.Calaprice and B.R.Holstein, Nucl. Phys. **A273** (1976) 301

42. H.Behrens and L.Szybisz, Physics Data **6-1** (1976)

43. P. Vogel, private communication

44. H. Blümer and K. Kleinknecht, Phys. Lett. **161B** 407

45. J. Wotschack, in *Neutrino '84*, proceedings of the 11th Inter. Conf. on Neutrino Phys. and Astrophys., Dortmund, 1984, edited by K. Kleinknecht and E.A. Paschos (World Scientific, Singapore, 1984) 117

46. L.A. Ahrens et al., Phys. Rev. D **31** (1985) 2732

47. G. Zacek et al., Phys. Rev. D **34** (1986)

48. F. Reines, Nucl. Phys. **A396** (1983) 469c

49. J.F. Cavaignac et al., Phys. Lett. **148B** (1984) 387

50. N. Baumann et al., in *Neutrino '84*, proceedings of the 11th Inter. Conf. on Neutrino Phys. and Astrophys., Dortmund, 1984, edited by K. Kleinknecht and E.A. Paschos (World Scientific, Singapore, 1984) 110

51. A.I. Afonin et al., JETP Lett. **42**, No. 5, (1985) 285
(Pis'ma Zh. Eksp. Teor. Fiz. **42**, No. 5, 230)

52. H. Kwon et al., Phys. Rev. D **24** (1981) 1097

53. F.A. Nezrick and F. Reines, Phys. Rev. **142** (1966) 852

54. F. Reines et al., Phys. Rev. Lett. **37** (1976) 315

55. V. Zacek et al., Phys. Lett. **164B (1985) 193**

56. A.H. Wapstra et al., Nucl. Phys. **A432** (1985) 1

57. Table of Isotopes, seventh edition, edited by C. Lederer and V. Shirley, John Wiley and Sons, Inc., New York (1978)

Table 1. Integers written to tape for each event.

Integer	Description
E1L	Pulse height from the low momentum end of wire 1
E1H	Pulse height from the high momentum end of wire 1
E2L	Pulse height from the low momentum end of wire 2
E2H	Pulse height from the high momentum end of wire 2
E3L	Pulse height from the low momentum end of wire 3
E3H	Pulse height from the high momentum end of wire 3
T1	Time delay between wire 1 and the backing scint.
T2	Time delay between wire 2 and the backing scint.
T3	Time delay between wire 3 and the backing scint.
TCO	Time delay between the coin. counter and the backing scint.
SLIT	Pulse height in the slit scintillator
COIN	Pulse height in the coin. counter
TIME	Time delay between the event and the end of the beam pulse
TAG	TAG > 0 indicates a pulser event
SCNT	Pulse height in the backing scintillator
TSL	Time delay between slit scint. and the backing scint.

Table 2. Spectral Shape Factors used in the analysis. E is the electron total energy and E_0 the electron total endpoint energy in MeV[57].

Nucleus	Shape Factor	E_0 (MeV)
^{12}B	$1 + 0.00524E$	13.884
^{20}F	$1 + 0.0126E$	5.909
^{90}Sr	$(p^2+(E-E_0)^2)(1-0.00978E)$	2.799

Table 3. Values of r_0 Derived From Various Runs

Nucleus	Run Number	r_0
^{12}B	94	4.014 ± .015
^{12}B	116	4.002 ± .015
^{20}F	98	4.000 ± .015
^{20}F	138	4.010 ± .015

Table 4. Different magnetic field settings used for ^{252}Cf. $p_{30(90)}$ is the momentum in channel 30 (90) with the wire positions P_i from eq. 7 rebinned into 128 channels.

Magnetic Field (kG)	p_{30}	p_{90}
0.98	1.64	2.69
1.33	2.22	3.64
1.70	2.84	4.66
2.40	4.01	6.58
3.39	5.67	9.29

Table 5. Experimental values and errors for the β spectrum of ^{252}Cf. The values of N_β are obtained from the fit discussed in section 3.3 with the background subtracted[+] normalized to agree with the calculation of Vogel[43] at p = 2.5 MeV/c. The systematic error is found by adding the errors in the relative efficiency, the spectrometer linearity/momentum bite, and the relative normalizations R_j in quadrature. The statistical error given is roughly the square root of the number of counts/bin at a given energy, it is thus a very conservative estimate of the error. The total error is just the systematic and the statistical errors added in quadrature.

$E_\beta^{K.E.}$	N_β/Mev·fission	$\Delta N_\beta^{syst.}$ (%)	$\Delta N_\beta^{stat.}$ (%)	$\Delta N_\beta^{tot.}$ (%)
2.0	8.63(-1)	3.9	2.0	4.4
2.5	5.32(-1)	2.5	2.0	3.2
3.0	3.17(-1)			
3.5	1.82(-1)	4.4	2.0	4.8
4.0	9.99(-2)			
4.5	5.26(-2)	5.9	3.0	6.6
5.0	2.64(-2)			
5.5	1.26(-2)	5.9	3.0	6.6
6.0	5.73(-3)			
6.5	2.46(-3)	7.5	6.0	9.6
7.0	1.00(-3)			
7.5	3.82(-4)	7.5	13	15
8.0	1.37(-4)	7.5	20	21
8.5	4.61(-5)	7.5	30	31

[+]The fitted background is 5.8(-5) N_β/MeV·fission when normalized as column 2. If this is a change in slope in the spectrum rather than a flat background it will raise N_β by 6% at $E_\beta^{K.E.}$ = 7.0 MeV, 15% at 7.5 MeV, and 40% at 8.0 MeV.

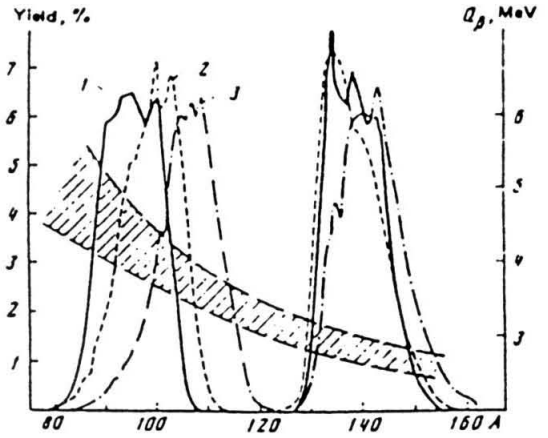

Fig. 1. Mass distribution of fragments for ^{235}U (curve 1) and ^{239}P (curve 2) for thermal-neutron fission, and for the spontaneous fission of ^{252}Cf (curve 3). The shaded region denotes the averaged energies for transitions between ground states of the isobaric nuclei. (from reference 17).

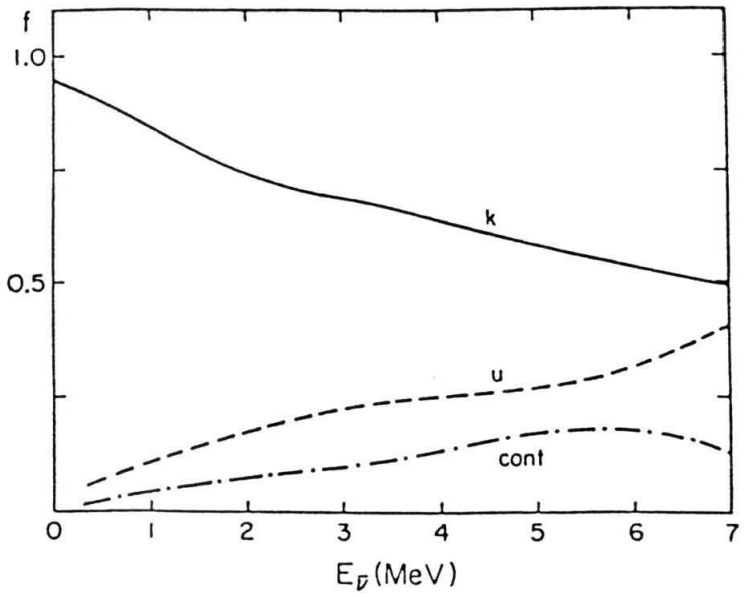

Fig. 2. Relative contribution of the known nuclei (k), unknown nuclei (u), and nuclei for which continous β-feed distributions were available (cont) to the $\bar{\nu}_e$ spectrum from ^{235}U (from reference 21).

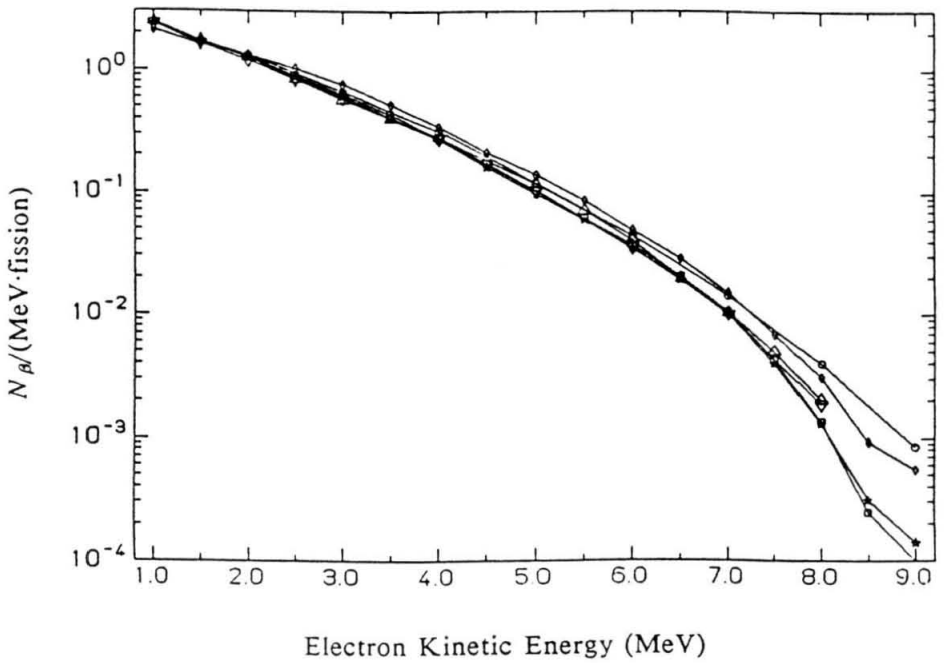

Fig. 3. Calculated $\overline{\nu}_e$ spectra from ^{235}U. (∇) - Davis et al. (ref. 14), (Δ) - Vogel et al. (ref. 21), (stars) - Klapdor and Metzinger (ref. 16), (○) - Kopeikin (ref. 17), (diamonds) - Avingnone and Greenwood (ref. 20). Also shown (□) is the $\overline{\nu}_e$ spectrum converted from the experimental β spectrum by Schreckenbach et al. (ref. 18).

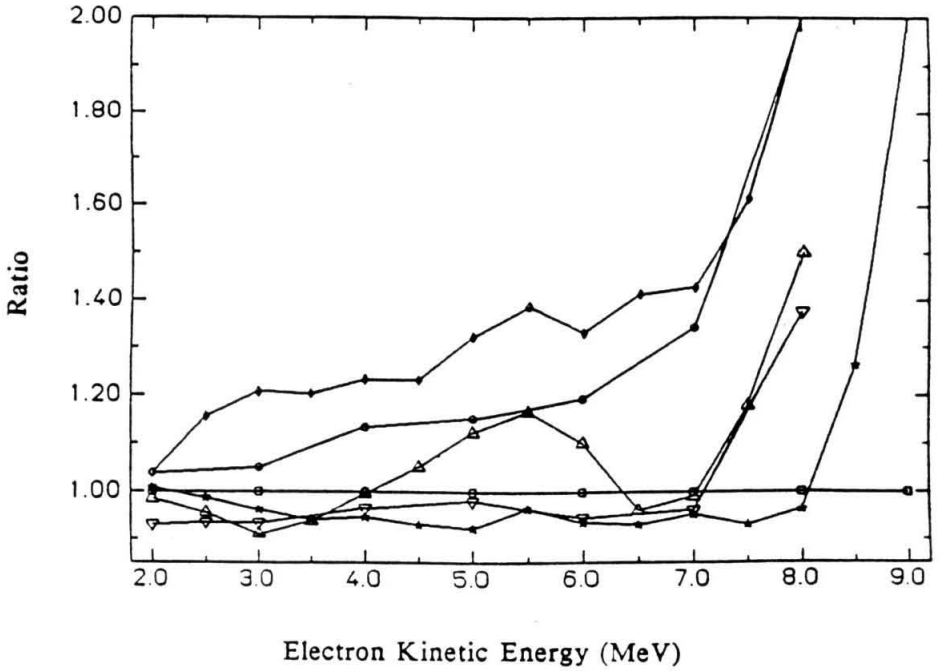

Fig. 4. Ratio of the spectra shown in fig. 3 to the $\overline{\nu}_e$ spectrum converted from the measured β spectrum by Schreckenbach et al. (ref. 18)

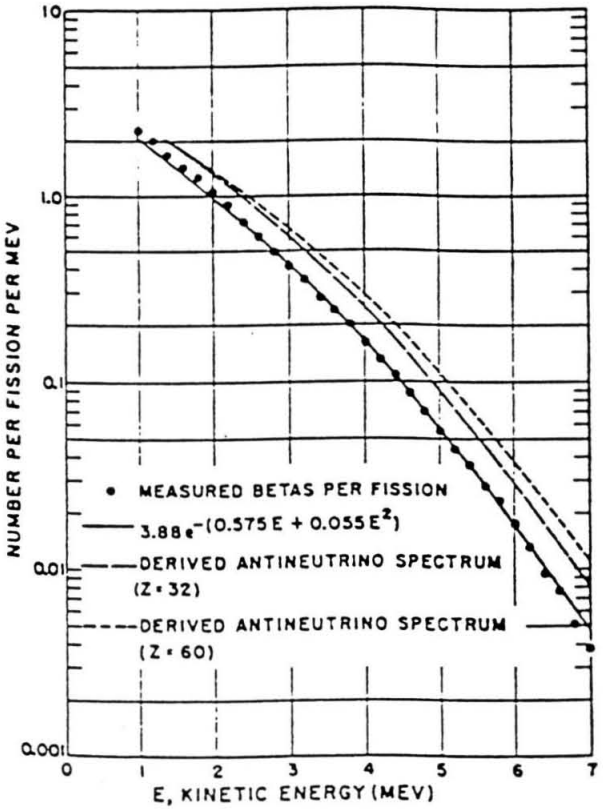

Fig. 5. β spectrum (corrected for detector response) from ^{235}U measured by Carter et al. (from reference 24).

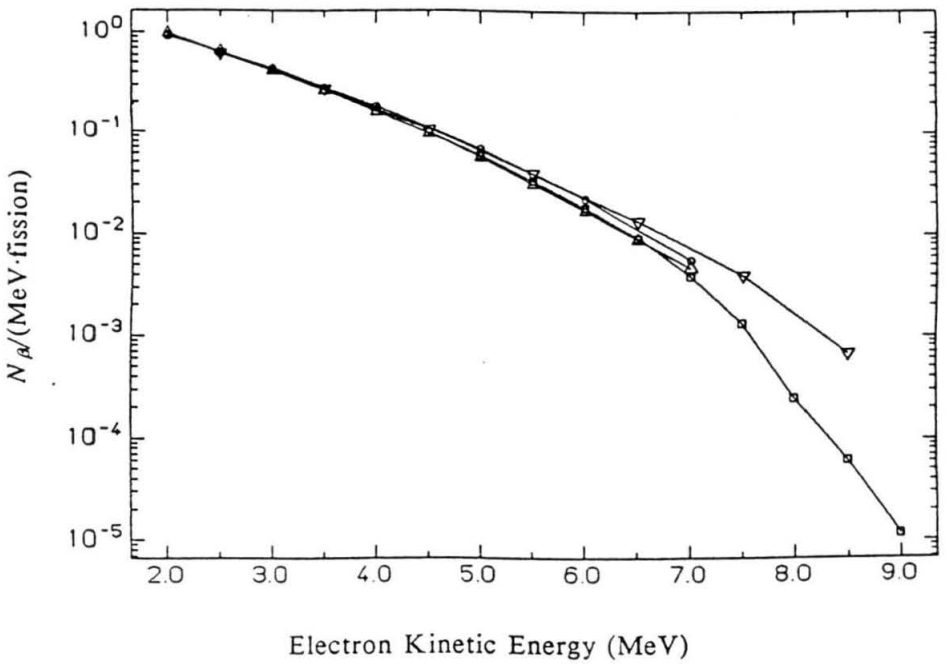

Fig. 6. Measured β spectra from ^{235}U. (□) - Schreckenbach et al. (ref. 18), (○) - Borovoi et al. (ref. 27), (Δ) - Carter et al. (ref. 24), (∇) - Tsoulfanidis (ref. 26). The Carter et al. spectrum is derived from the empirical fit given in their paper.

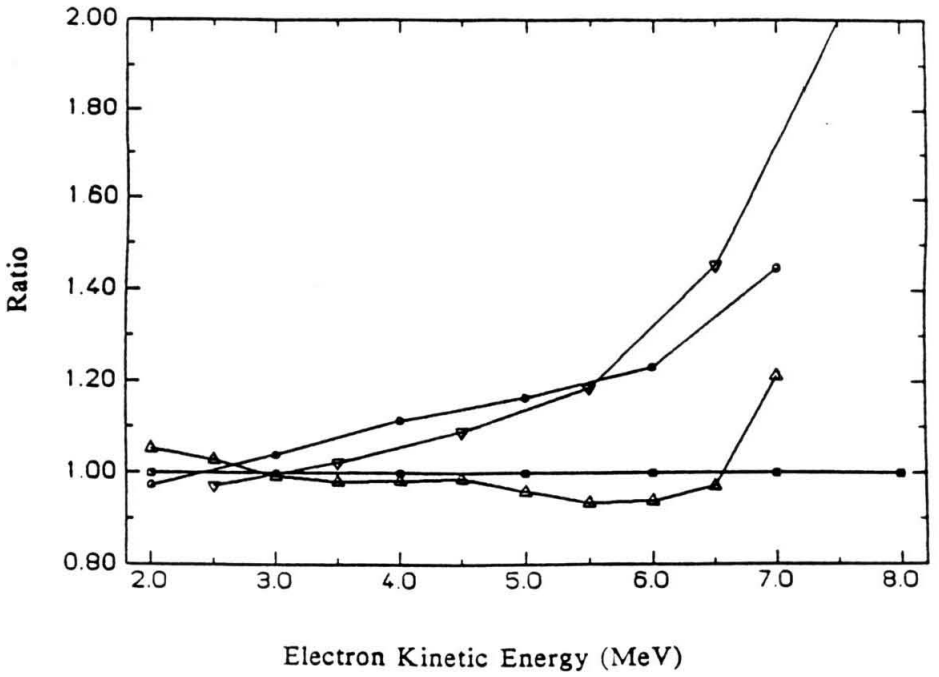

Fig. 7. Ratio of the spectra shown in fig. 6 to the β spectrum measured by Schreckenbach et al. (ref. 18)

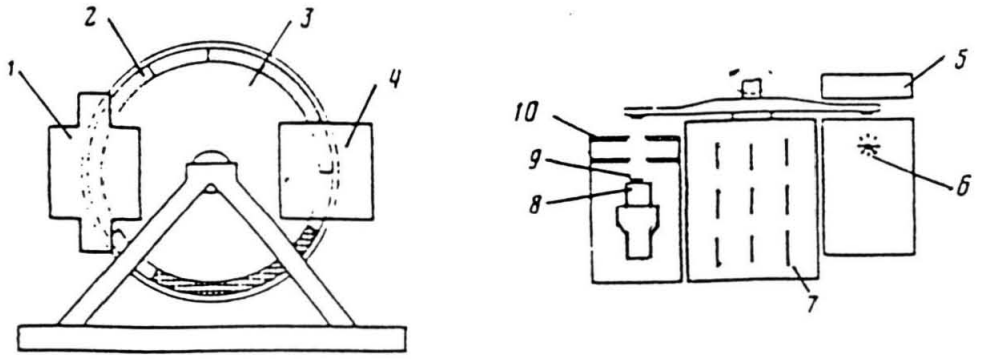

Fig. 8. Diagram of the apparatus of Borovoi et al. 1- β spectrometer, 2- targets, 3- disk of Plexiglas, 4- paraffin block moderator, 5- reflector of paraffin, 6- ^{252}Cf neutron source, 7- combination shielding, 8- main detector, 9- transmission detector, 10- diaphragms. (from reference 27).

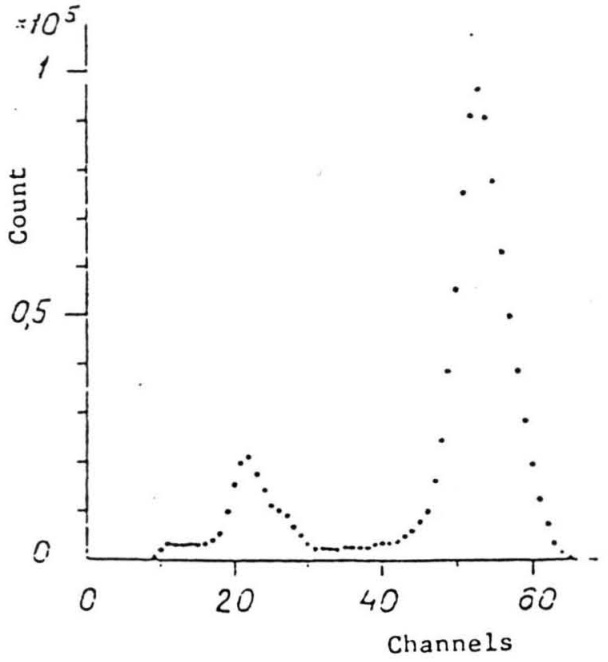

Fig. 9. Response of the detector of Borovoi et al. to conversion electrons from ^{207}Bi. (from reference 27).

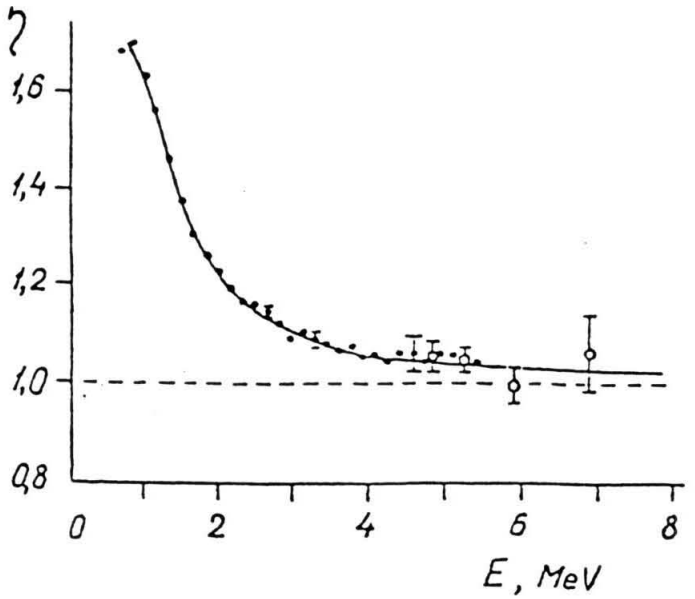

Fig. 10. Relation between the electron spectrum from thick (20mg/cm^2 Pb) and thin ^{252}Cf sources (unspecified thickness) used to correct for source effects by Borovoi et al. (from reference 27).

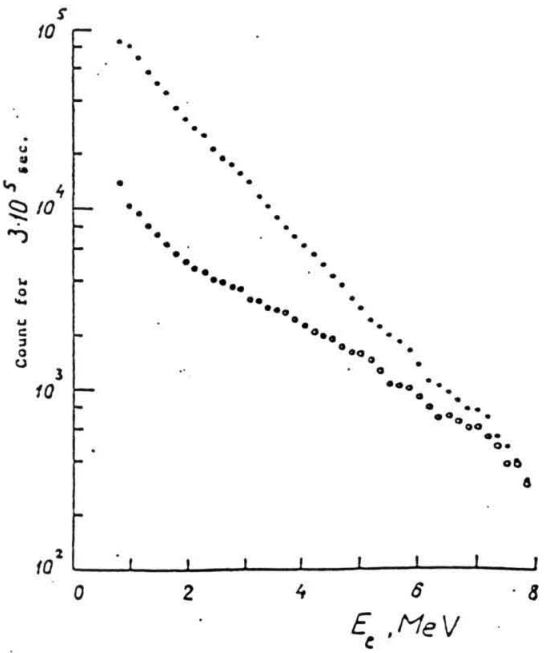

Fig. 11. Measured spectrum and background for one ^{235}U run by Borovoi et al. • - measured spectrum o - measured background. (from reference 27).

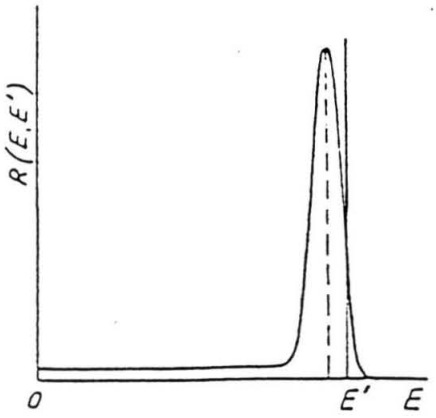

Fig. 12. Spectrometer response function adopted by Borovoi et al. (from reference 27).

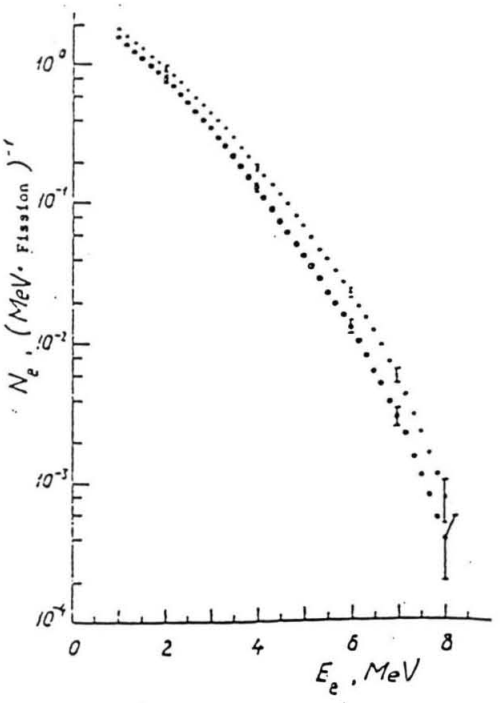

Fig. 13. β spectra and errors from thermal neutron fission of ^{235}U (•) and ^{239}P (o) measured by Borovoi et al. (from reference 27).

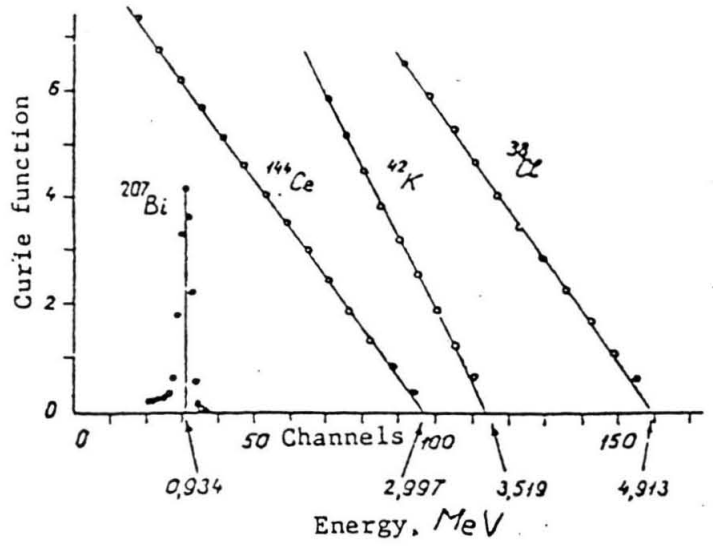

Fig. 14. Kurie plots used as energy calibration by Borovoi et al. (from reference 27).

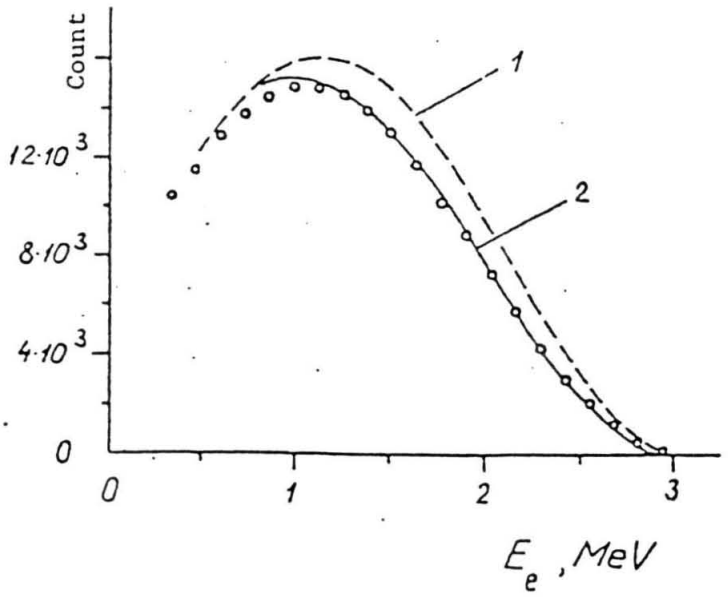

Fig. 15. Measurement of the β spectrum from ^{144}Pr by Borovoi et al. o - measured points, 1 - theoretical spectrum, 2 - theoretical spectrum transformed to account for detector response. (from reference 27).

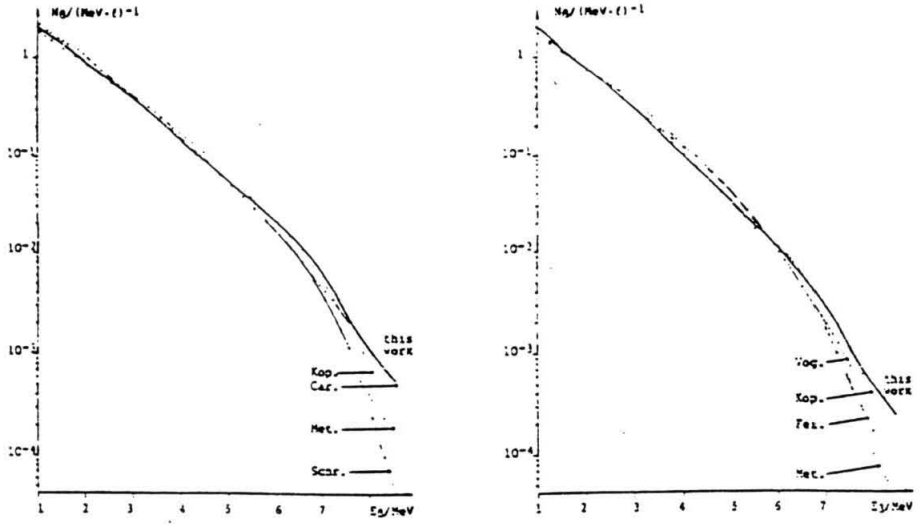

Fig. 16. β spectra measured by Kayser from thermal neutron fission of ^{235}U (left) and ^{239}P (right). The other spectra are taken from: Schr. (reference 29), Car. (reference 24), Kop. (reference 17), Fei. (reference 28), Vog. (reference 21), and Met. (reference 16). (this fig. from reference 32).

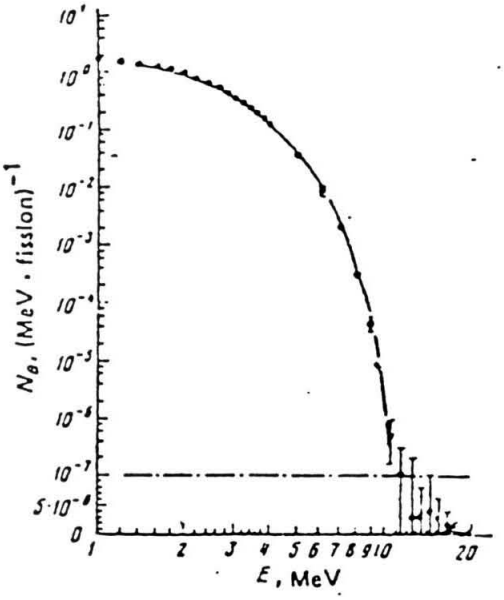

Fig. 17. The measurement of Borovoi et al. of the β spectrum from the spontaneous fission products of ^{252}Cf (points) and the calculation of Kopeikin[33] (solid line), the vertical scale below the dotted line is linear. (from reference 35).

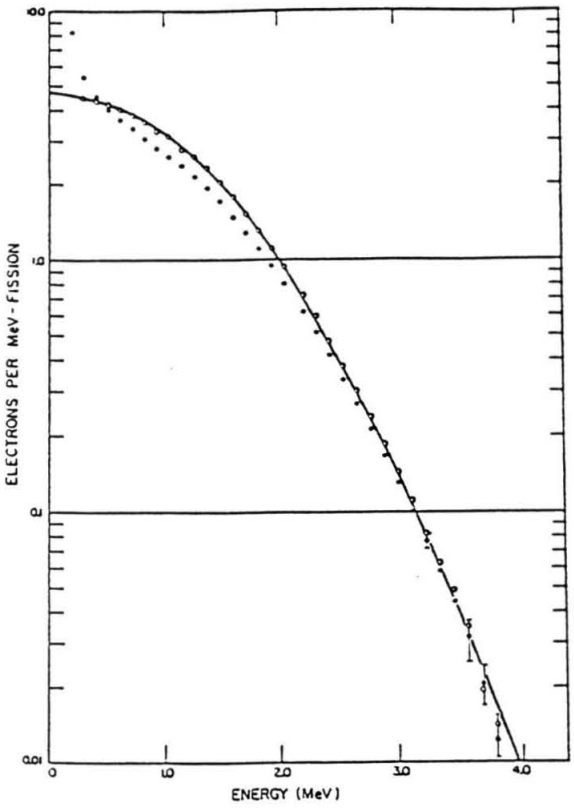

Fig. 18. The measurement of Knief et al. of the low energy part of the β spectrum from the spontaneous fission products of ^{252}Cf. Measured spectrum (•), compensated for detector response (∘) and empirical fit (solid line). (from reference 34).

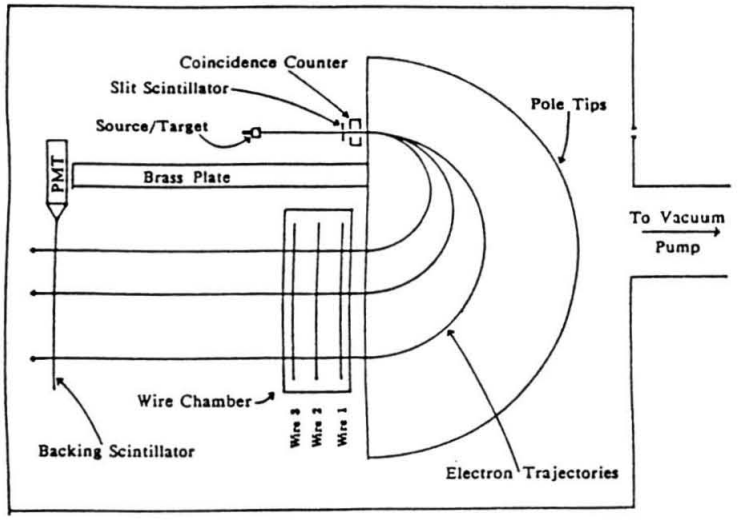

Fig. 19. Side view of the experiment showing relative positioning of the source/target, detectors, and magnet. To set the scale wires 1, 2 and 3 are 13.4 cm. long.

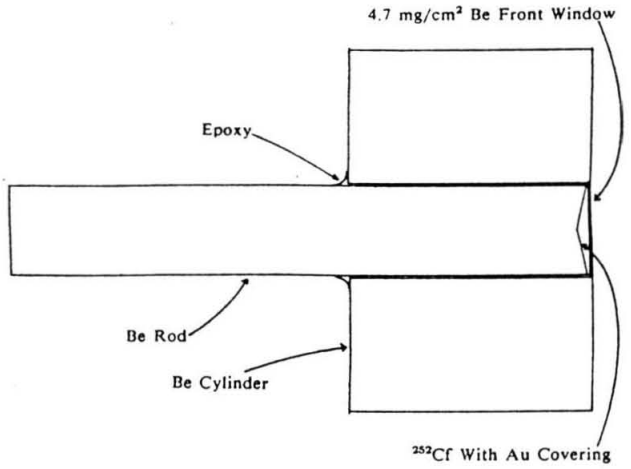

Fig. 20. Cross section of the ^{252}Cf source. The rod fits tightly into the cylinder, the gap is exaggerated in the drawing.

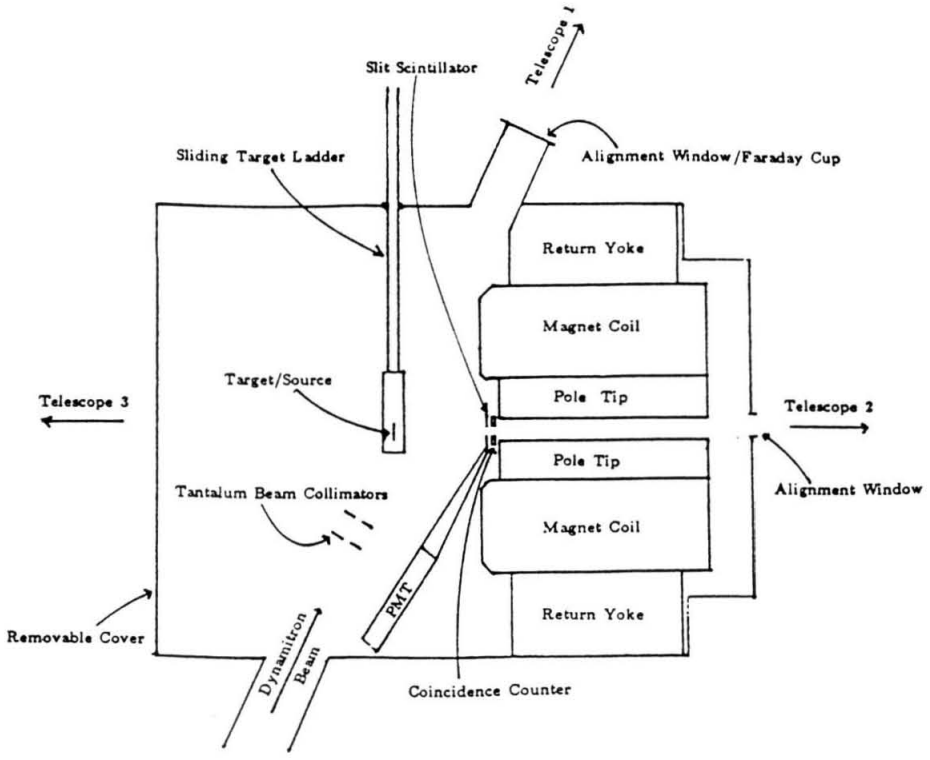

Fig. 21. Top view of the spectrometer to show positioning and alignment of the source/target and detectors.

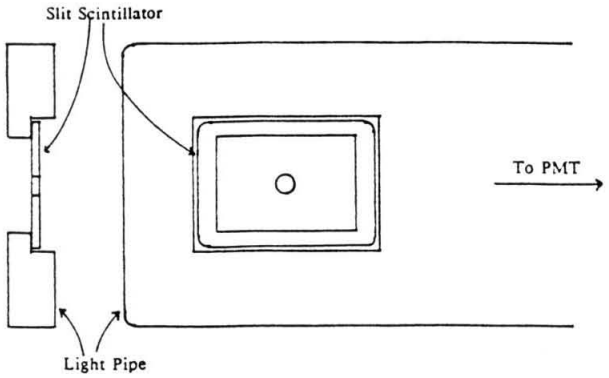

Fig. 22. Detail of the slit scintillator. The scintillator was held in place with optical grease to assure good light coupling between the scintillator and the light pipe.

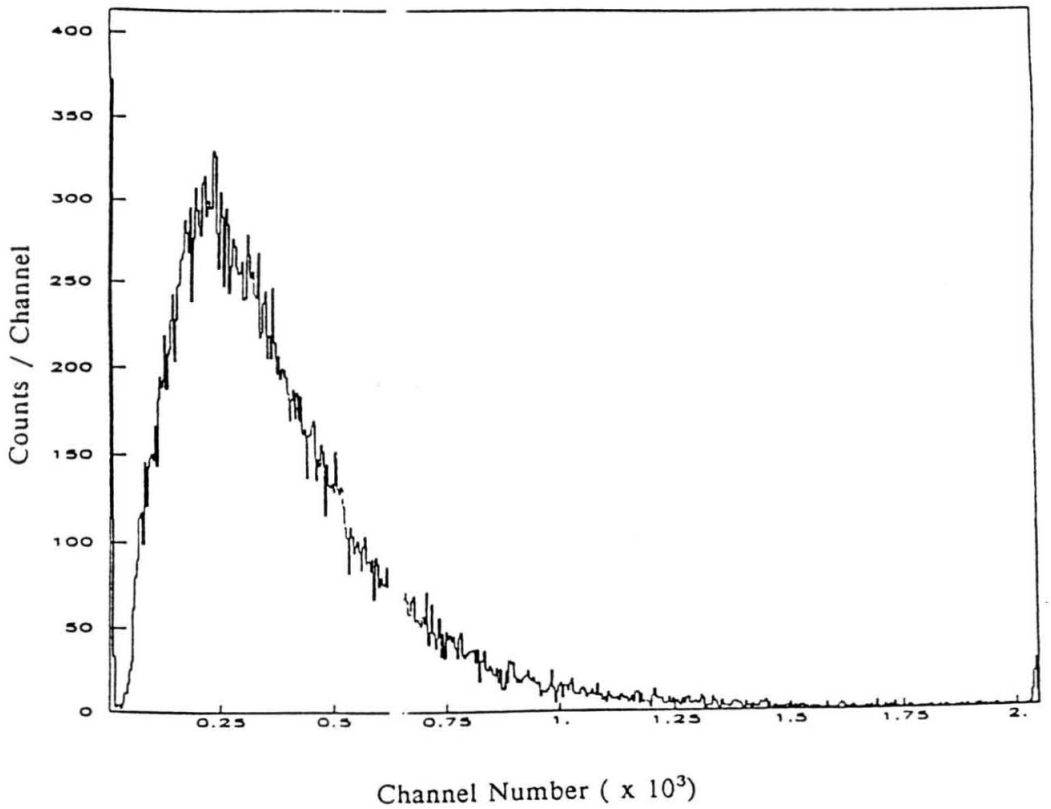

Fig. 23. Pulse height spectrum in the slit signal for events in time coincidence with the backing scintillator (the discriminator that produces the slit timing signal is set at channel ~30). The events in channels 0-30 come from partially read events as discussed in section 3.1.1. The peak of the distribution corresponds to an energy loss in the scintillator of ~150 keV. Any event which has a pulse height in the slit < channel 30 is considered good, this plot shows that virtually all the electrons which deposit energy in the slit will be vetoed by this condition. This plot and the subsequent plots from LISA (figs. 25, 27, 28, 32-37) are from electrons from ^{252}Cf with a field setting of 1.7 kG (2.6 < p_e < 5.0 MeV/c). Note also that for these plots the histograms displayed are rebinned by a factor of 4 (4 channels → 1) with respect to the labeling on the x-axis.

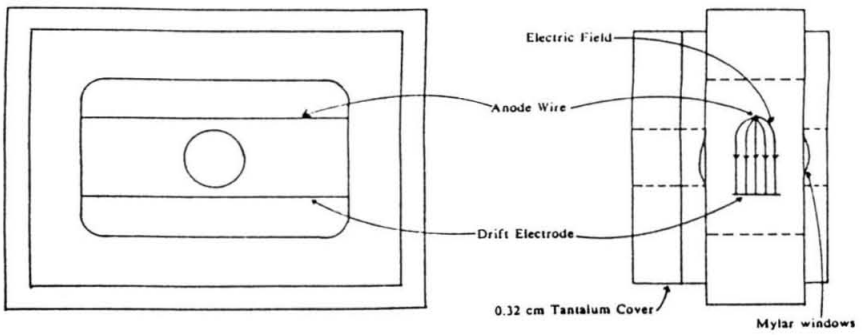

Fig. 24. Simplified diagram of the coincidence counter. For clarity the electrical and gas connections have been omitted. With the exception of the labeled parts the counter is made of aluminum.

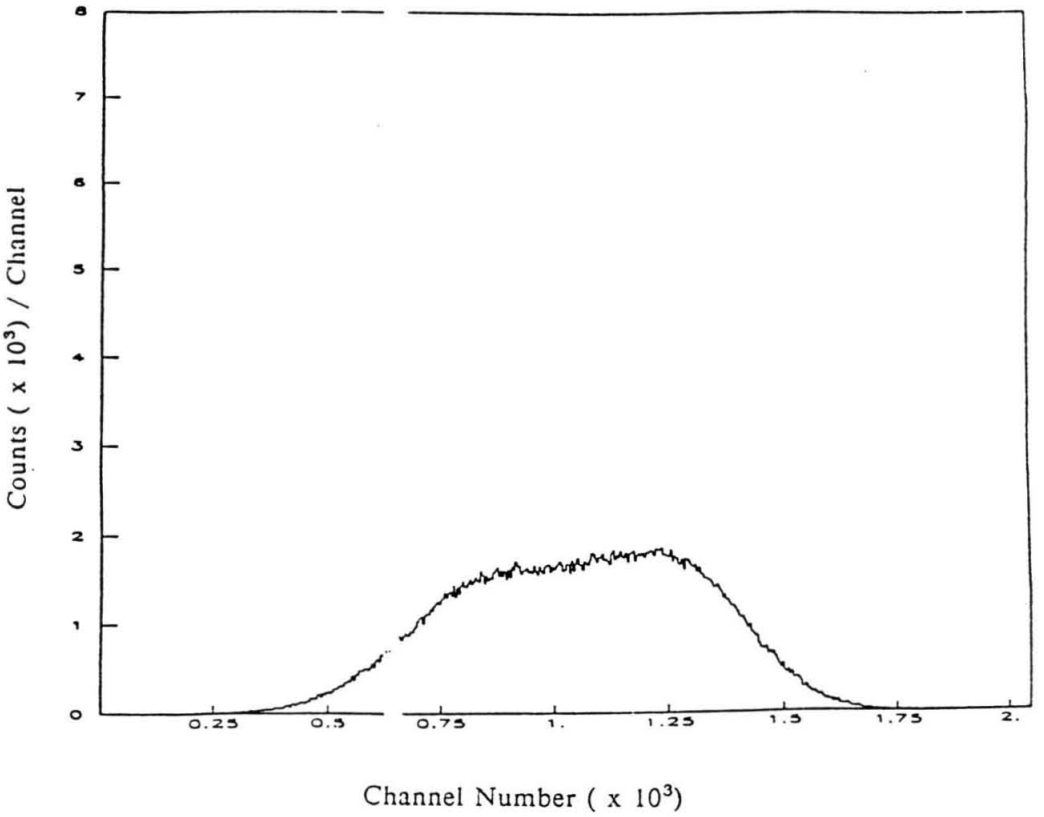

Fig. 25 Pulse height spectrum from the coincidence counter. The signal is well separated from the noise. The irregular shape is caused by the gain drifting during the run.

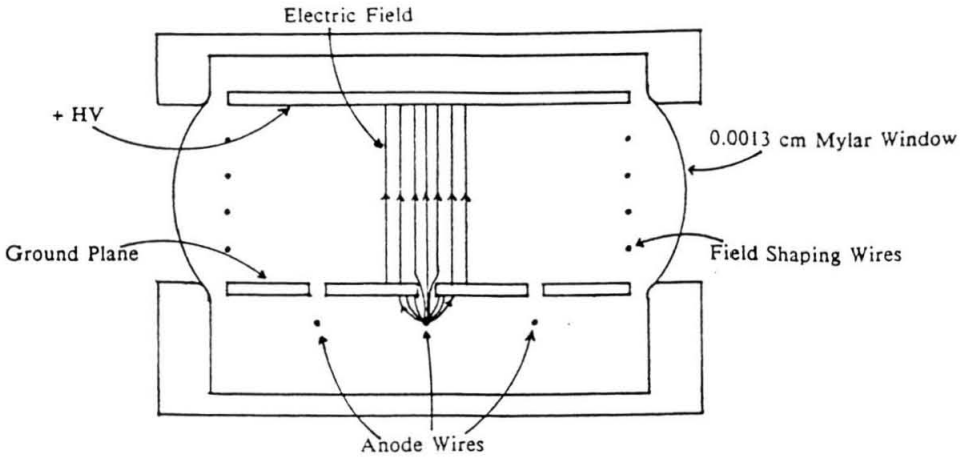

Fig. 26. Cross section of the position sensitive wire chamber.

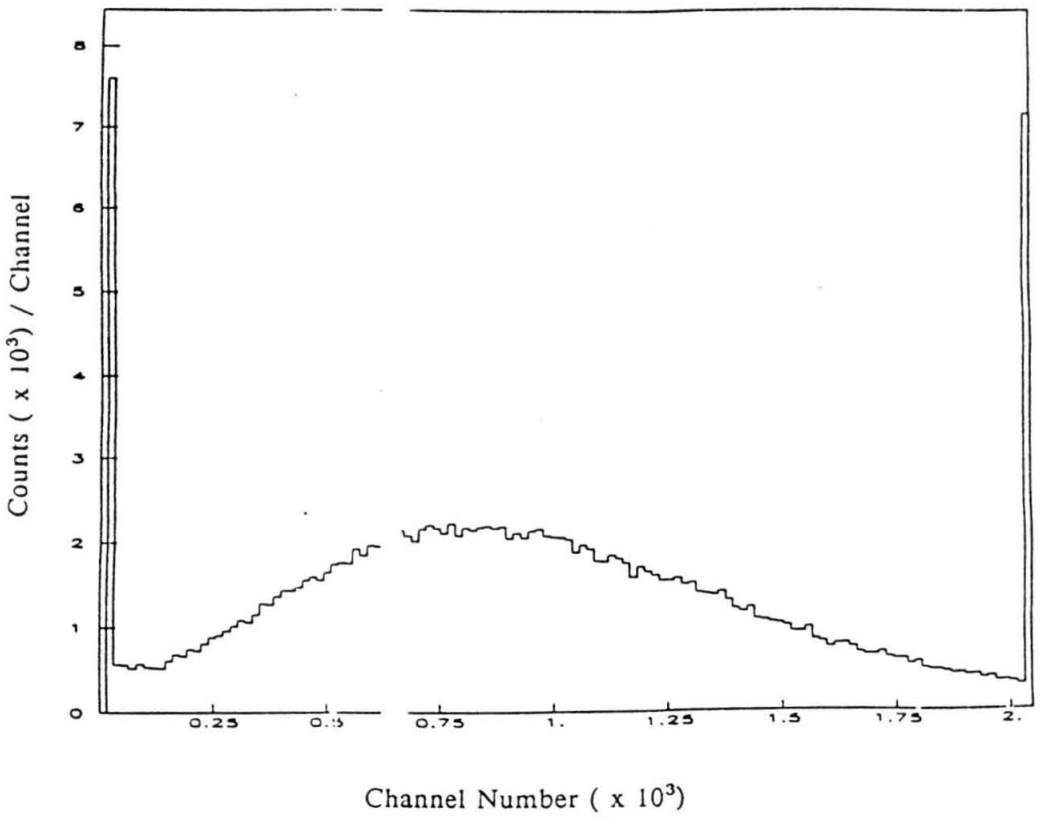

Fig. 27 Pulse height spectrum (sum of both wire ends) from wire 1 of the position sensitive wire chamber. Good events have pulse heights in the range 100-2046.

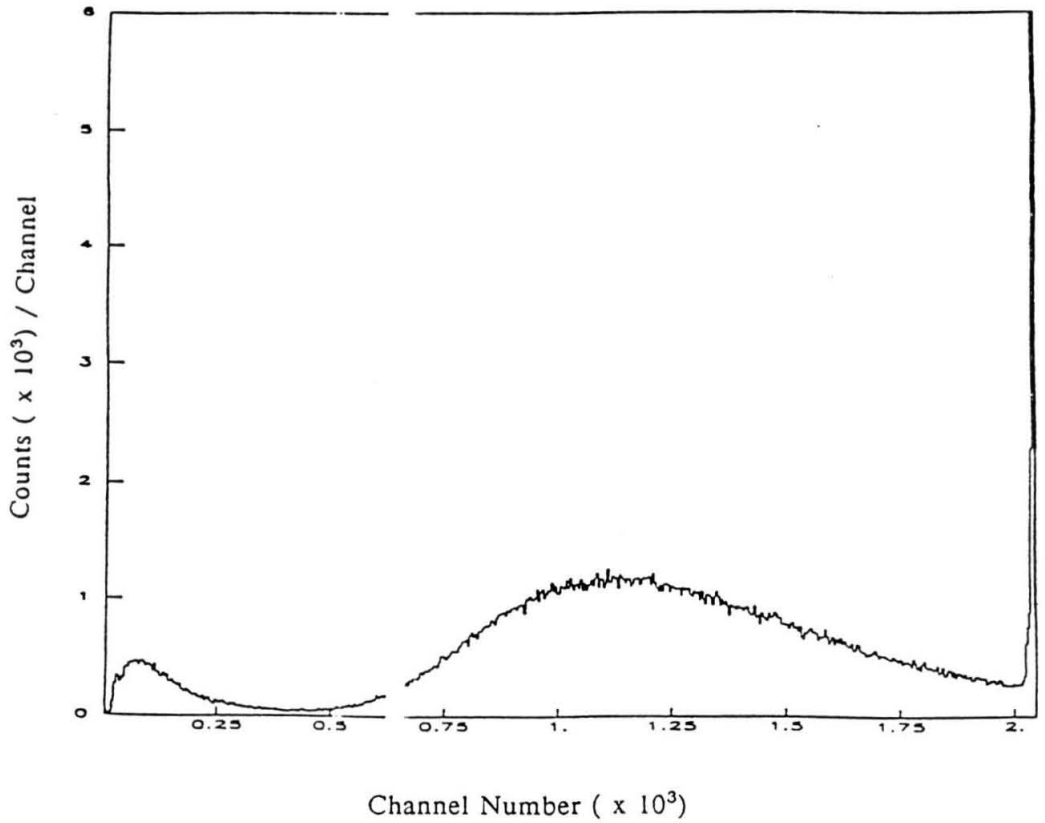

Fig. 28. Pulse height spectrum from the backing scintillator. The cut was placed at channel 300 for an efficiency of ~96%.

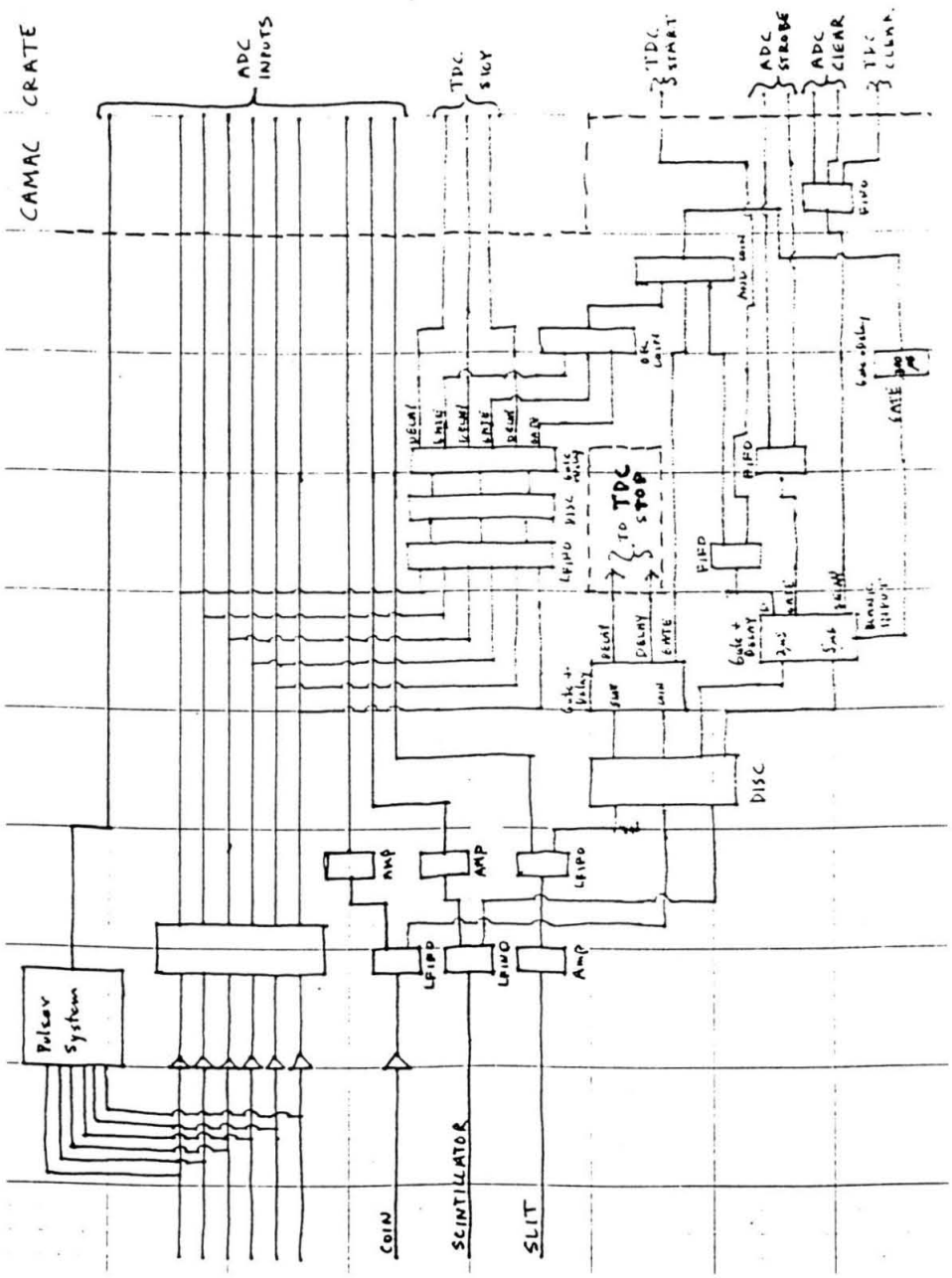

Fig. 29. Block diagram of the electronics.

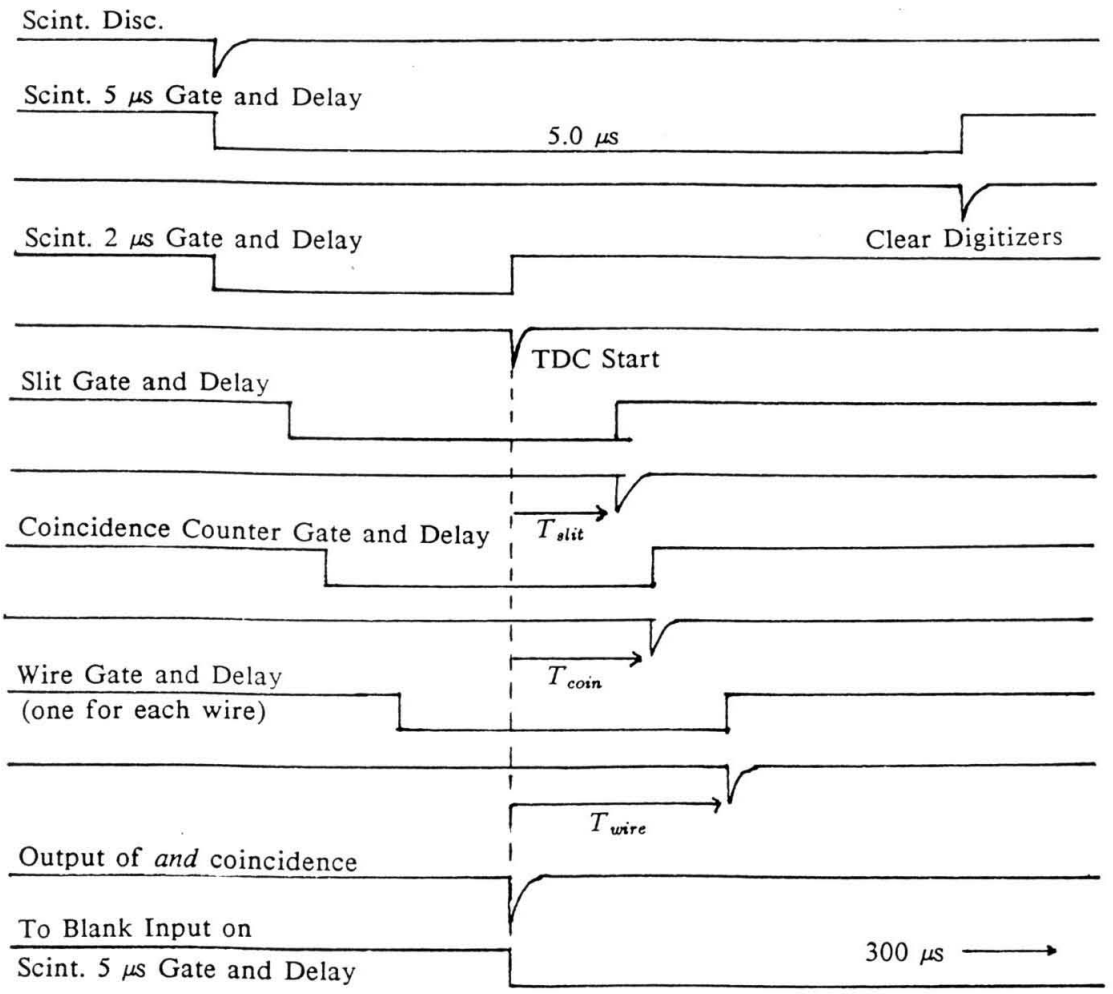

Fig. 30. Relative timing of the various electronic signals.

	Beam On Electronics Off	Beam Off Electronics Off	Beam Off Electronics On	Beam Off Electronics Off
^{12}B	30 ms	1 ms	30 ms	1 ms
^{20}F	10 s	1 ms	10 s	1 ms

Fig. 31. Time cycle used to control the beam and electronics for the accelerator runs on ^{12}B and ^{20}F.

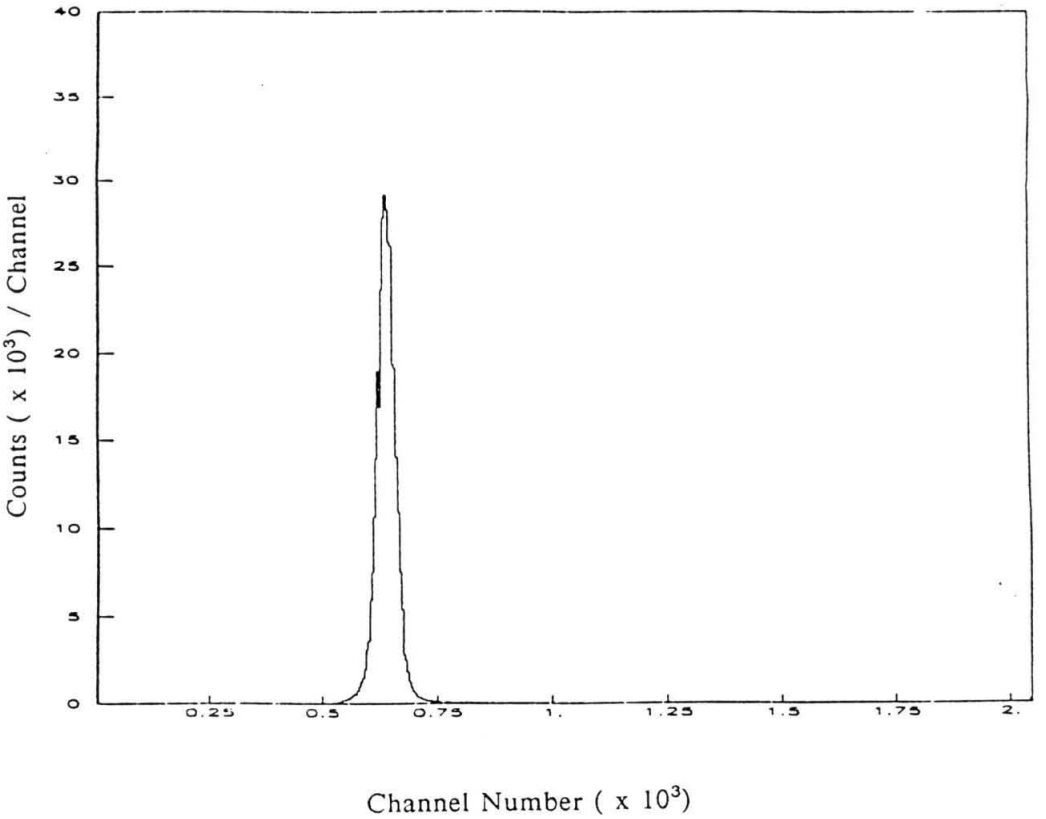

Fig. 32. Relative timing between the coincidence counter and the backing scintillator. Full scale (2048 channels as the x-axis is labeled or 512 as the histogram is binned) corresponds to 2 μs. Good events were those in channels 595-725 (so as to agree with the calibration runs were a tight window was needed due to accidentals).

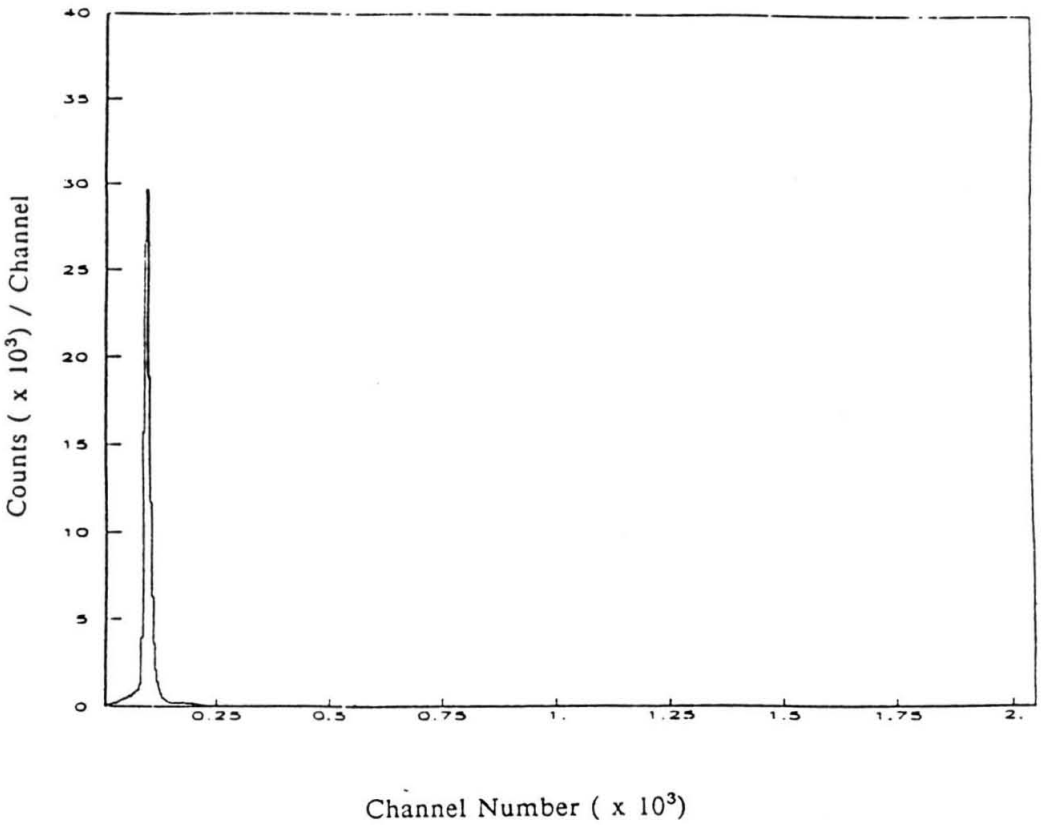

Fig. 33 Relative timing between the slit and the backing scintillator. Full scale corresponds to 2 μs.

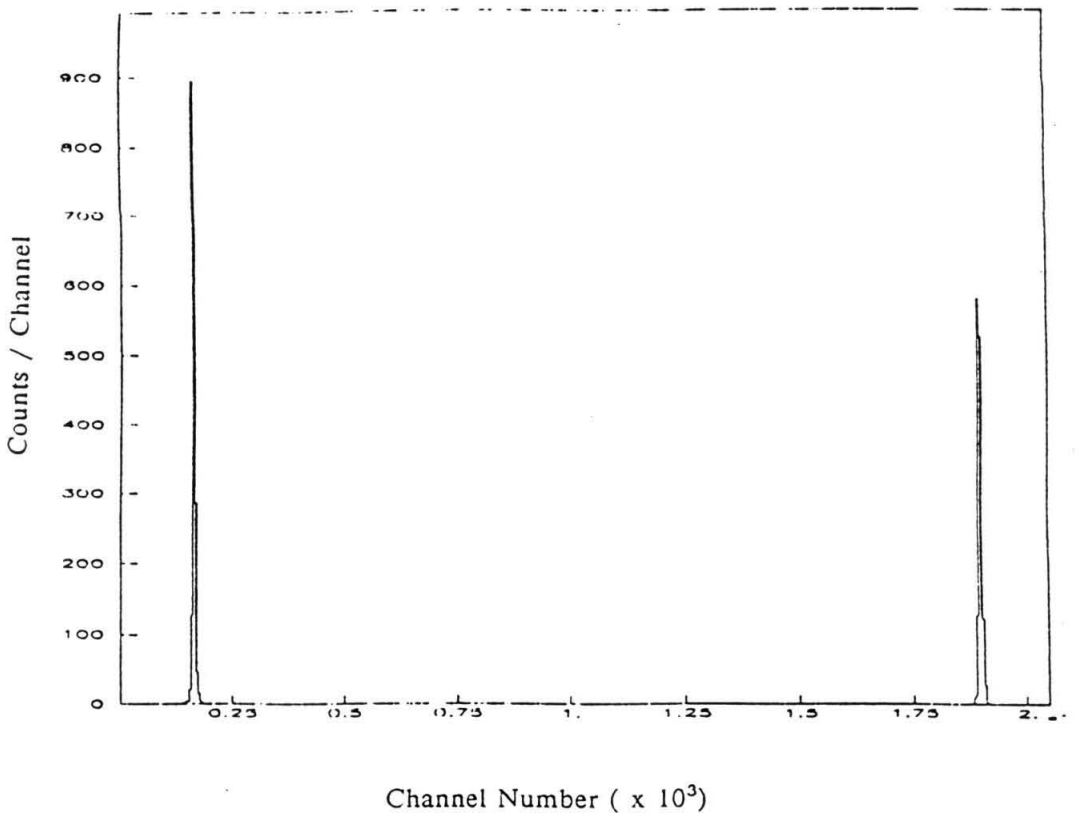

Fig. 34. Pulser position spectrum. Obviously there is only slight gain drift for this run, it is greater in the longer runs. These peaks mark the pulse height ratio for the ends of the wires.

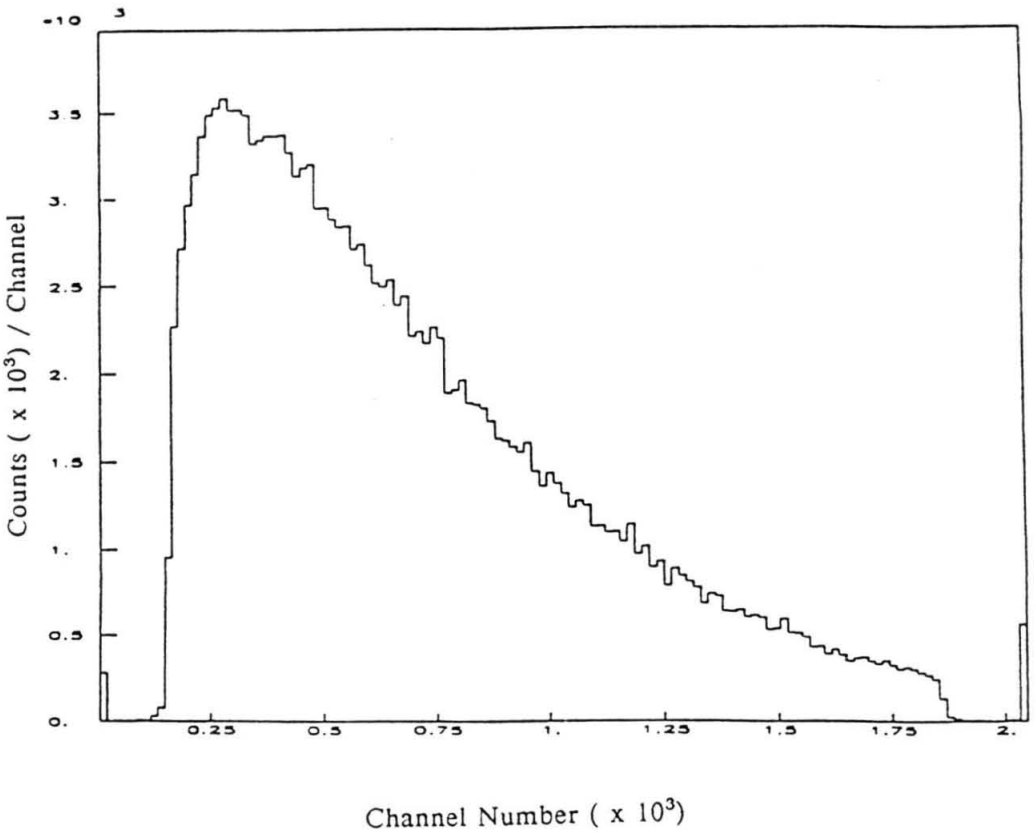

Fig. 35. Position spectrum from wire 1 (for events with a good pulse height in wire 1) and wire 3 otherwise. The overflow and underflow events are from partially read events as discussed in section 3.1.1. This spectrum has been rebinned into 128 channels.

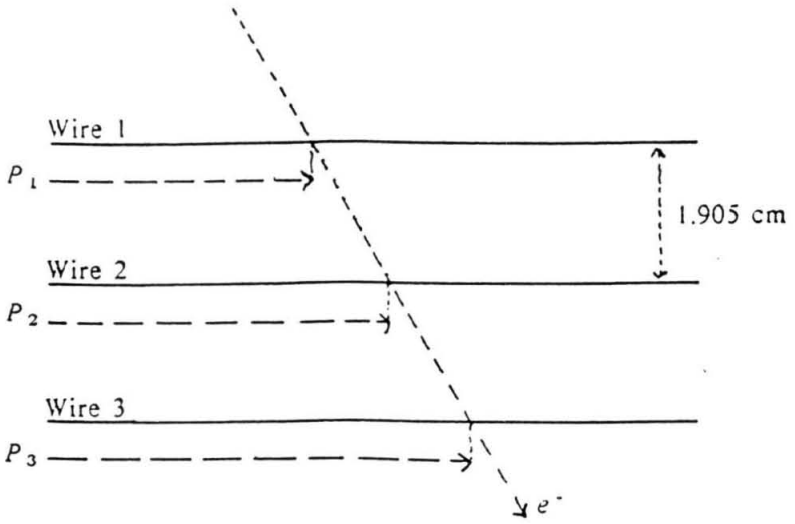

Fig. 36. Inspection of this fig. shows that for perfect position resolution an electron traveling in a straight path through the wire chamber will have $P_R = 2P_2 - P_1 - P_3 = 0$. The angle θ is given by $\theta = \tan^{-1}(P_A/3.81)$ where $P_A = P_3 - P_1$ (here in cm) as defined in eq. 9.

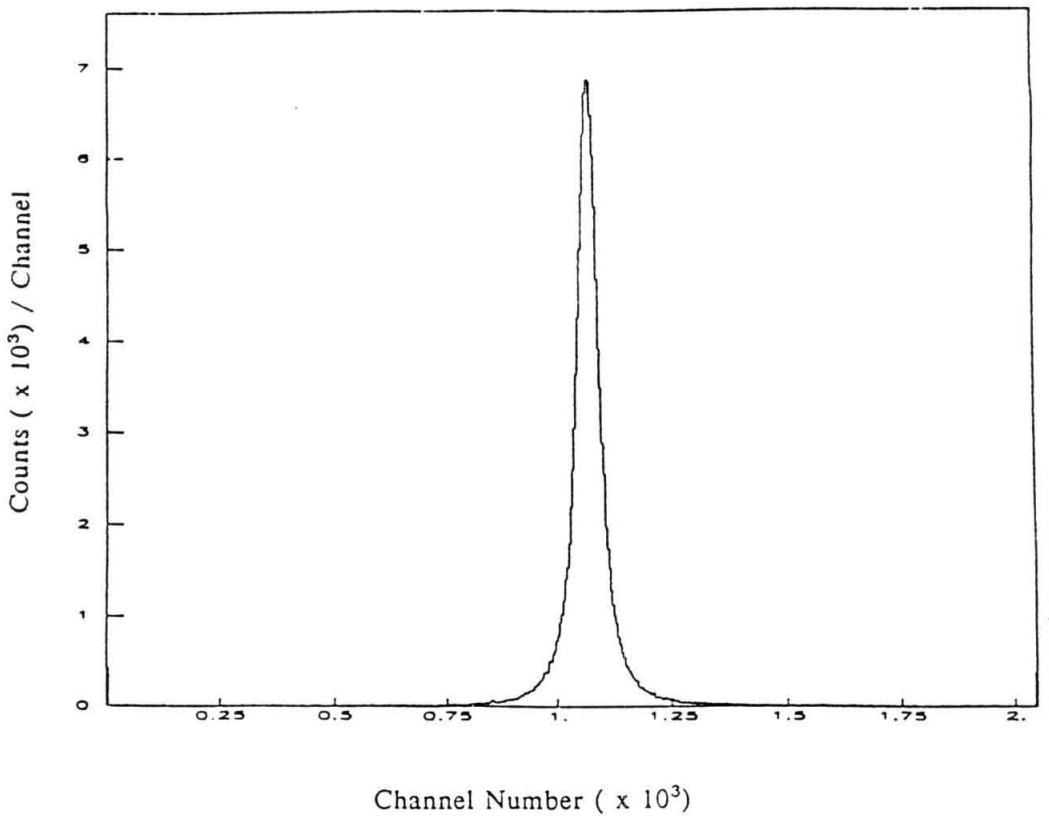

Fig. 37. P_R as defined in eq. 15 and fig. 36, the FWHM seen here (13/512 channels) corresponds to a per wire electronic resolution of 1.5 mm.

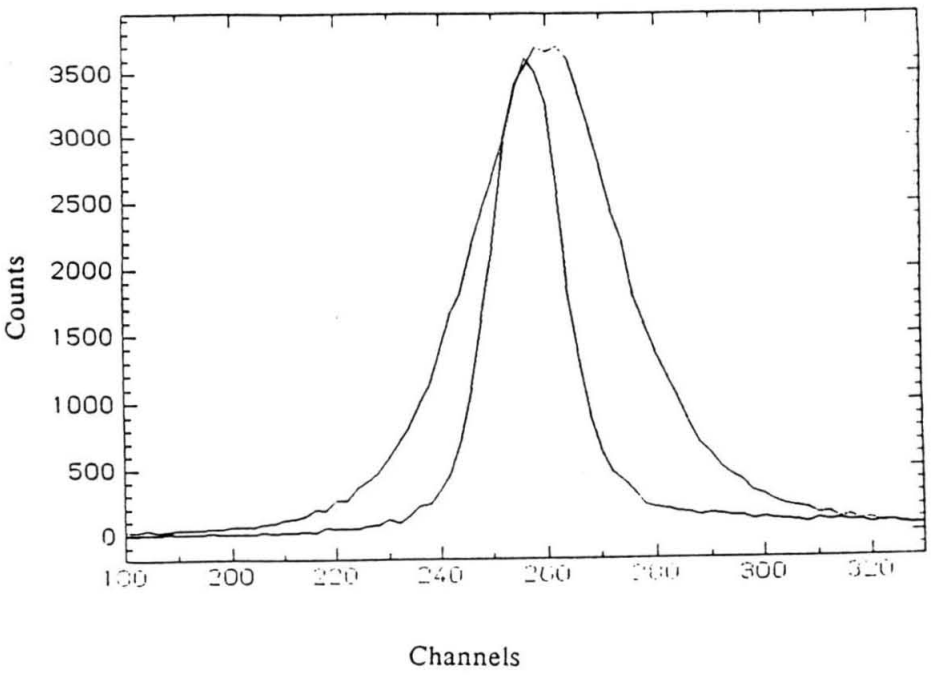

Fig. 38. Plot of P_Λ (offset from zero by 256 channels) for runs of ^{252}Cf with magnetic field = 0.98 kG (wide peak) and 3.39 kG (narrow peak), for electron momenta see Table 4. The peak widths (HWHM) correspond to a scattering angle θ (see fig. 36) of 2.5° for the 3.39 kG and 5.8° for 0.98 kG. Half this scattering occurs in the front window of the detector, it therefore adds 0.8 mm to the per wire resolution in wire 1 for 3.39 kG and 1.9 mm for 0.98 kG. Added in quadrature to the electronic resolution this produces a resolution of 1.7 mm at 3.39 kG and 2.4 mm at 0.98.

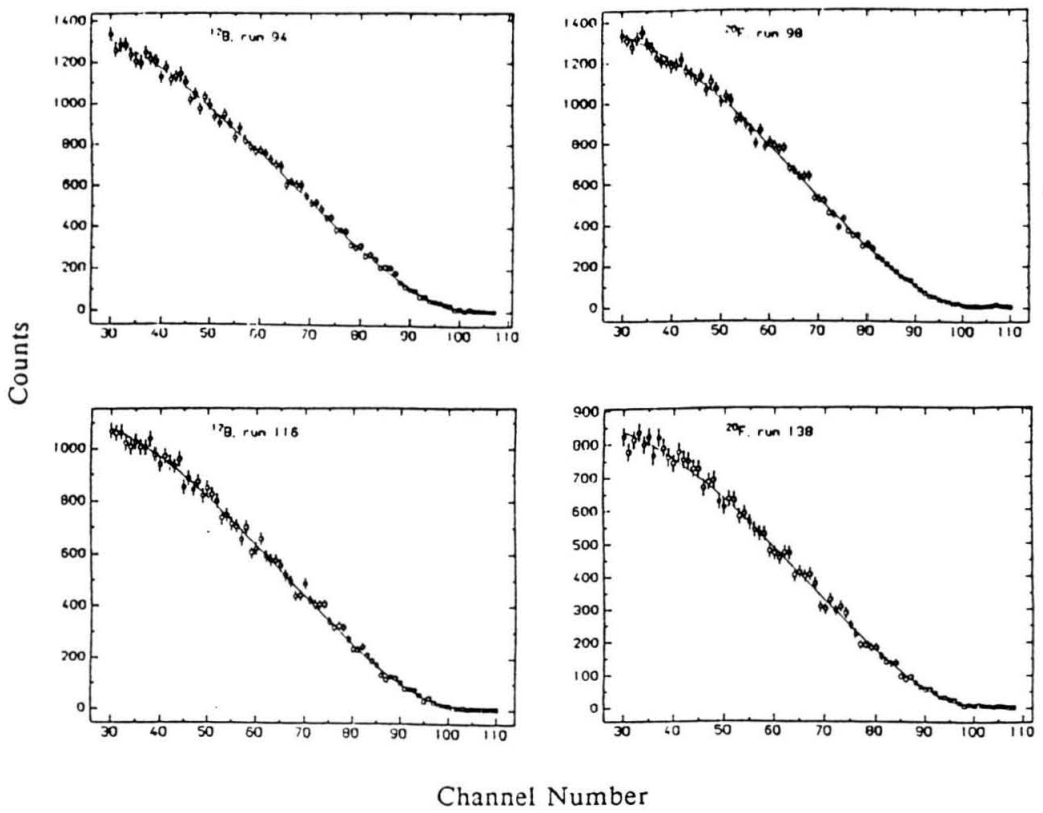

Fig. 39. Fits to ^{12}B and ^{20}F spectra from two accelerator runs (the ^{20}F spectra are corrected for the relative spectrometer efficiency by ~5% at low momenta as discussed in section 3.2.3).

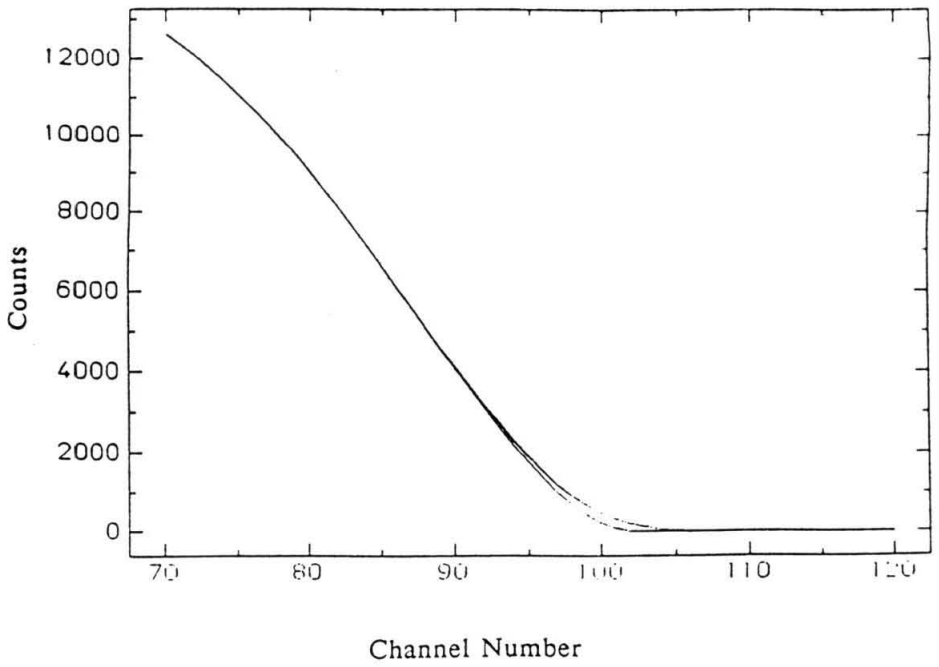

Fig. 40. Measured spectral shape near the endpoint for perfect resolution (bottom curve) and 1.5% resolution (top curve). Compare to fig. 41.

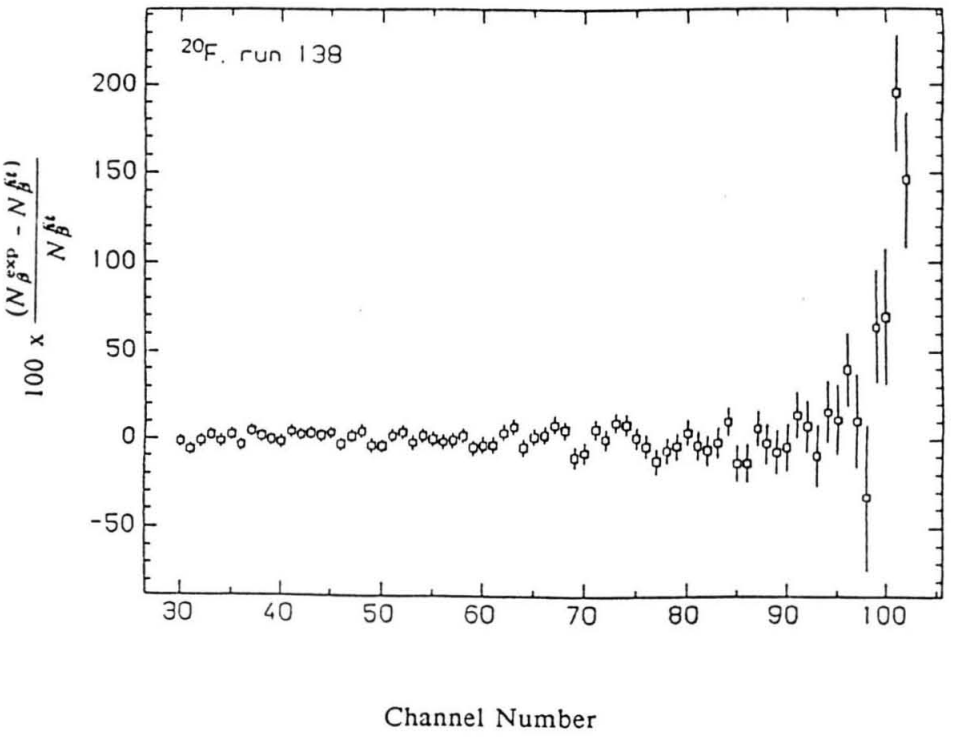

Fig. 41. Deviations from the fit demonstrating the effect of finite spectrometer resolution near the endpoint. Compare fig. 40.

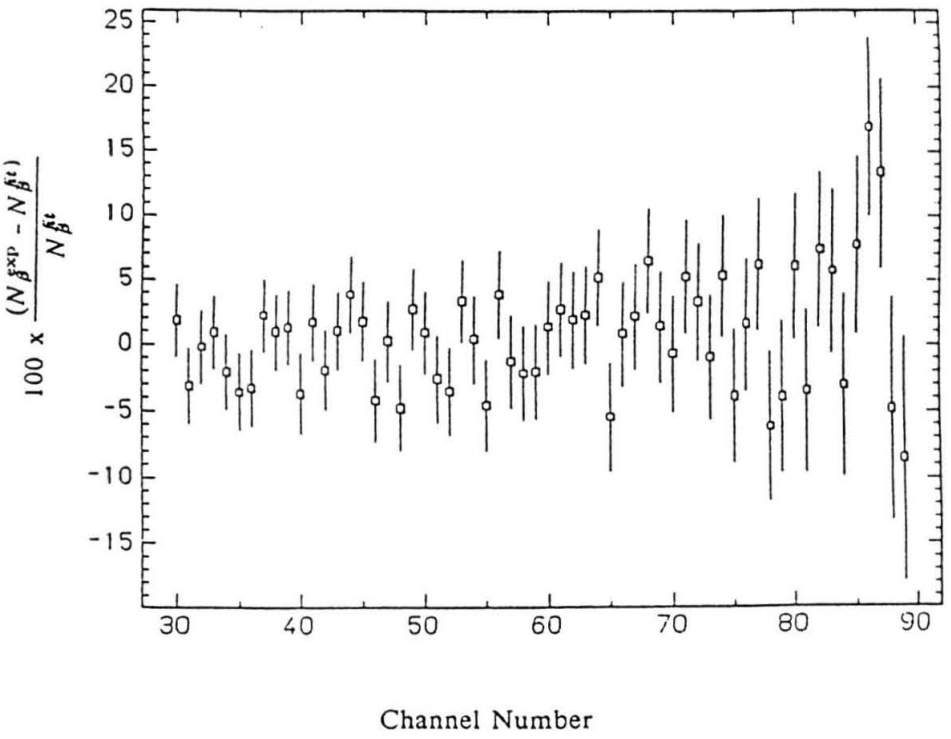

Fig. 42. Deviations from fit for ^{12}B run 94. The fit was done to channels 50-90, there is no statistically significant evidence for a systematic curvature in these residuals. (B = 4.9 kG, $p_{channel=30} = 8.2$, $p_{90} = 12.8$ MeV/c)

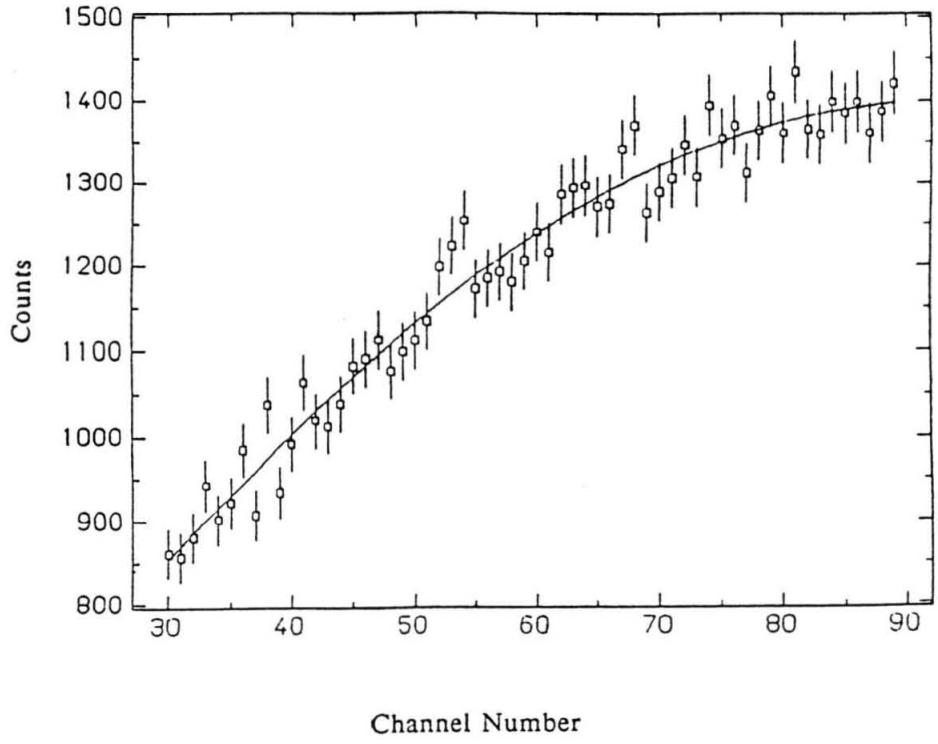

Fig. 43 Measured spectrum and fit for low field ^{20}F measurement. The fit has three free parameters, the overall norm and the two parameters in the parameterization of the efficiency given in eq. 12. r_0 is fixed at 4.006 cm. (B = 1.19 kG, $p_{30} = 2.0$, $p_{90} = 3.1$ MeV/c)

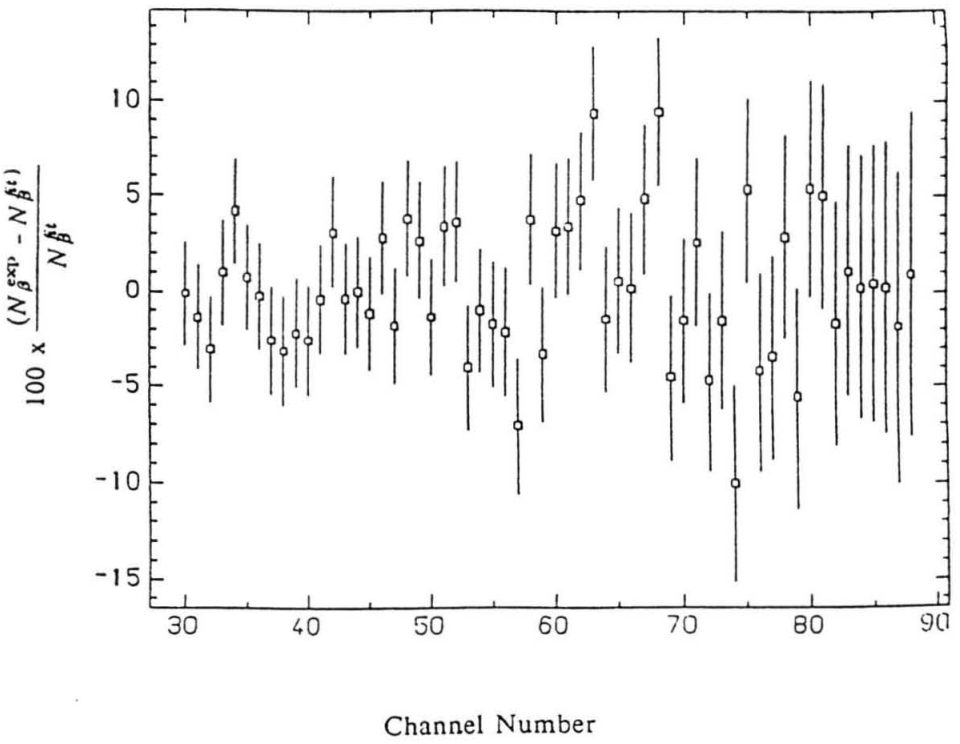

Fig. 44 Same as fig. 42 but for ^{20}F run 98. (B = 2.1 kG, $p_{30} = 3.5$, $p_{90} = 5.5$ MeV/c)

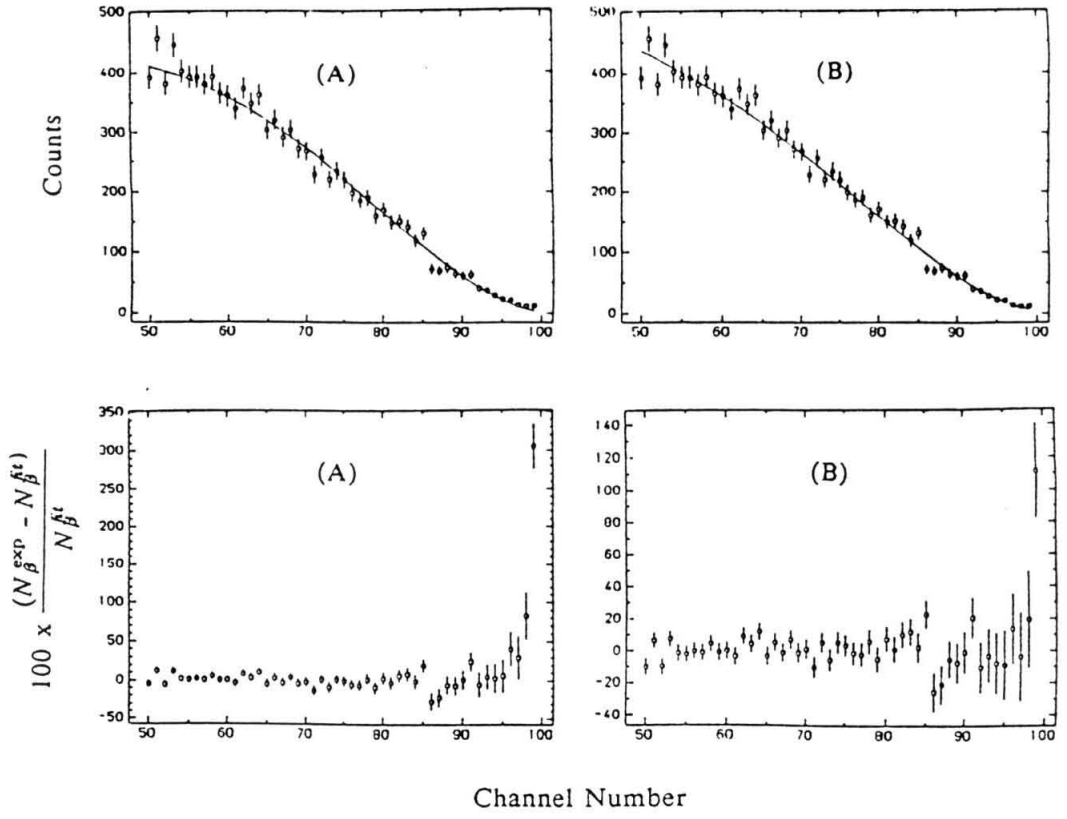

Fig. 45. Fits and deviations for ^{90}Sr spectra with (A) and without (B) efficiency correction.

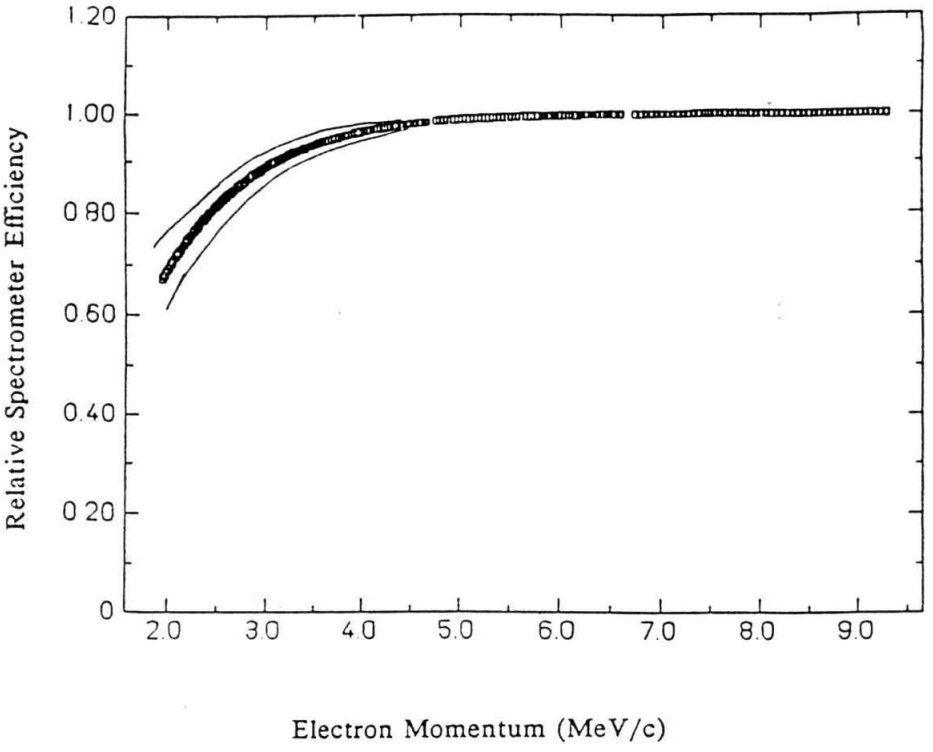

Fig. 46. Adopted relative spectrometer efficiency (squares) and error (solid lines).

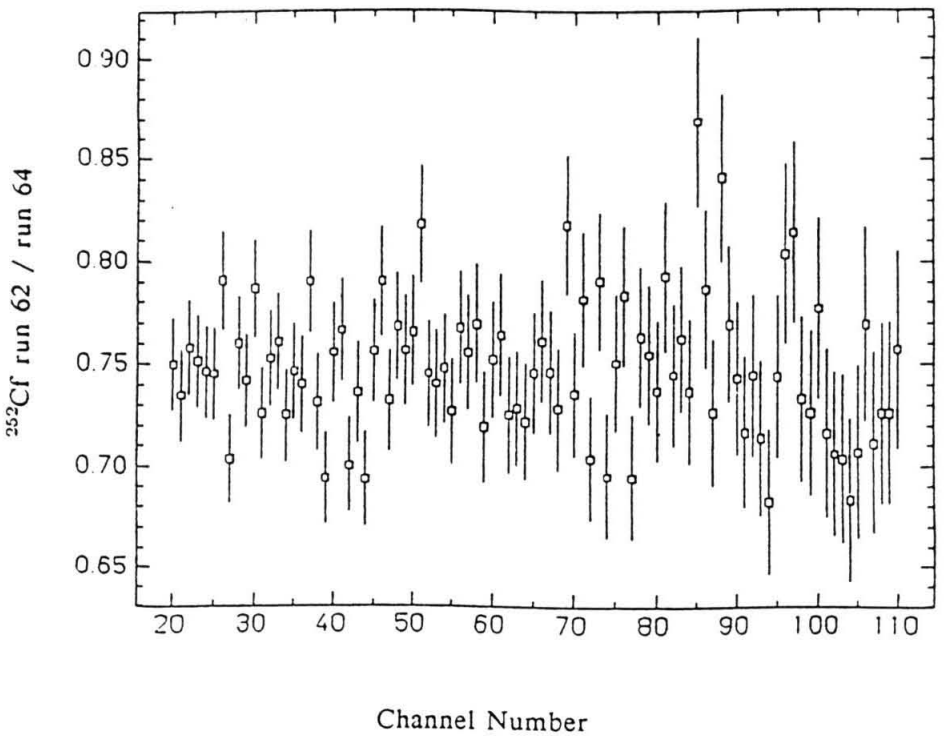

Fig. 47. Ratio of two different runs at the same magnetic field (1.33 kG).

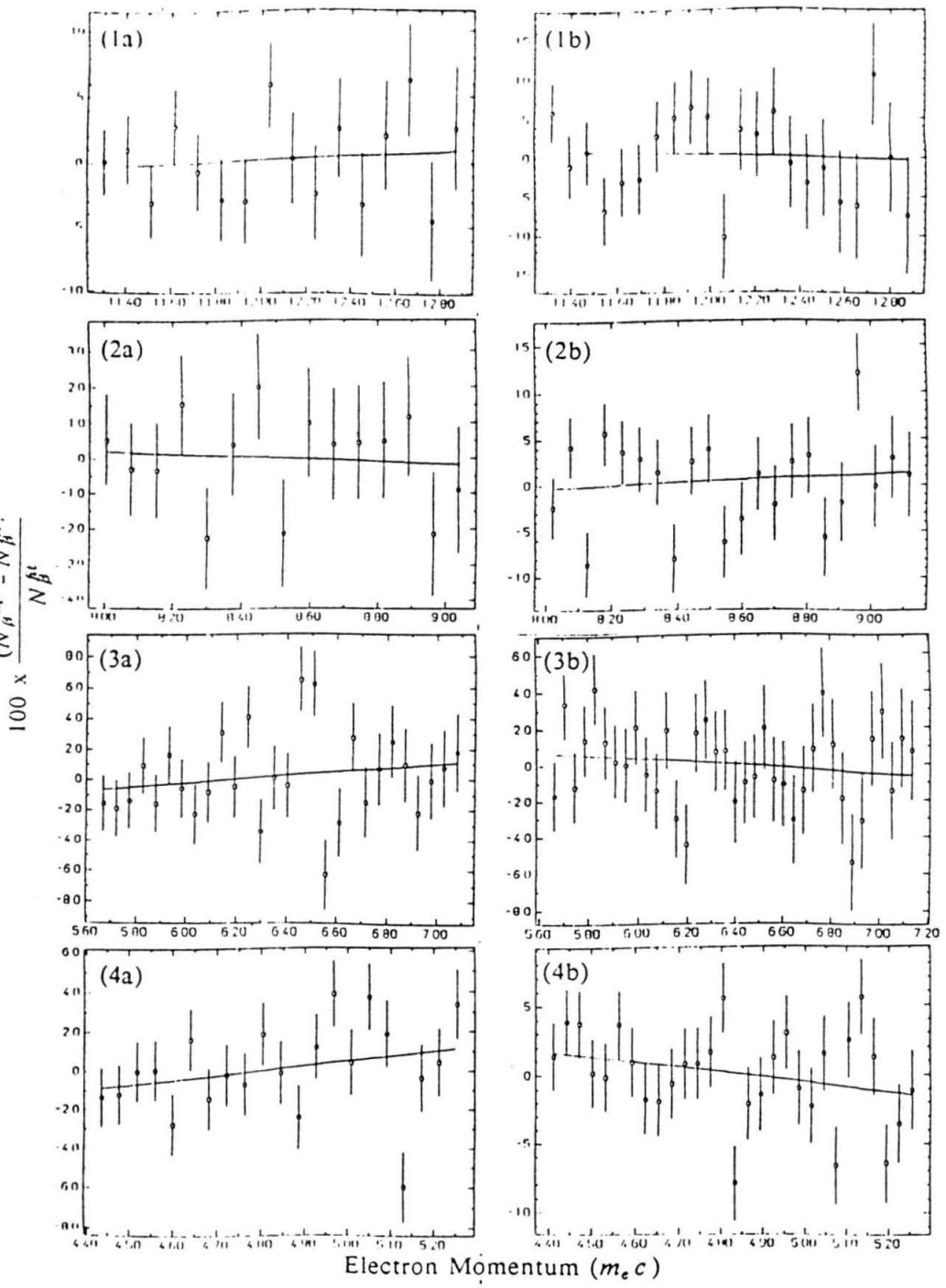

Fig. 48. Deviations from the fits to the overlapping regions from measurements of ^{252}Cf at different magnetic fields (as discussed in section 3.3) 1. Deviations from the overlap of 3.39 kG (1a) and 2.4 kG (1b). 2. Overlap of 2.4 (2a) and 1.7 (2b). 3. Overlap of 1.7 (3a) and 1.33 (3b). 4. Overlap of 1.33 (4a) and 0.98 (4b). The lines are best fits to the deviations (note that here the electron momentum is in units of $m_e c$).

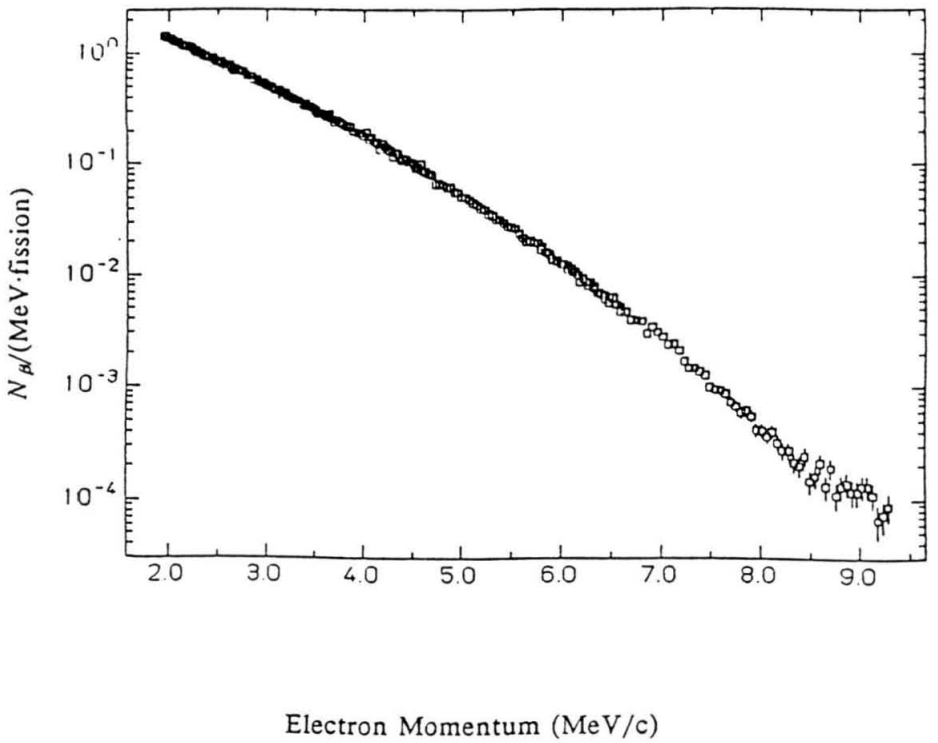

Fig. 49. Measured ^{252}Cf spectrum corrected for relative spectrometer efficiency (no background subtraction). The spectrum has been normalized to agree with the calculation of Vogel[43] at 2.5 MeV/c.

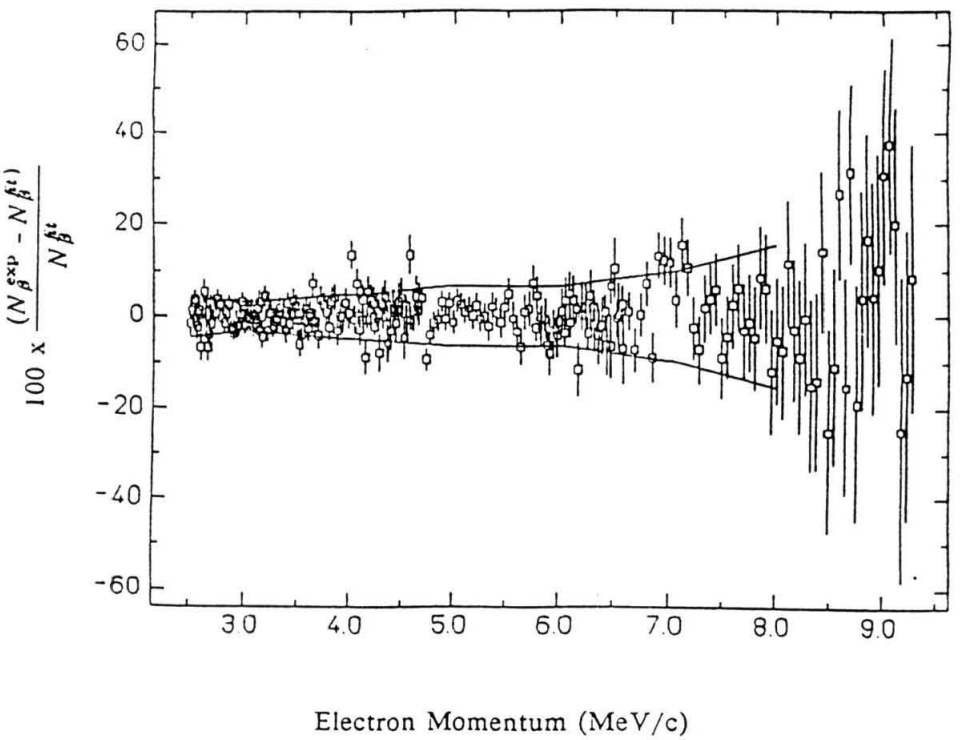

Fig. 50. Deviations from the fit to the ^{252}Cf spectrum discussed in section 3.3. The solid lines show the total error on the measurement.

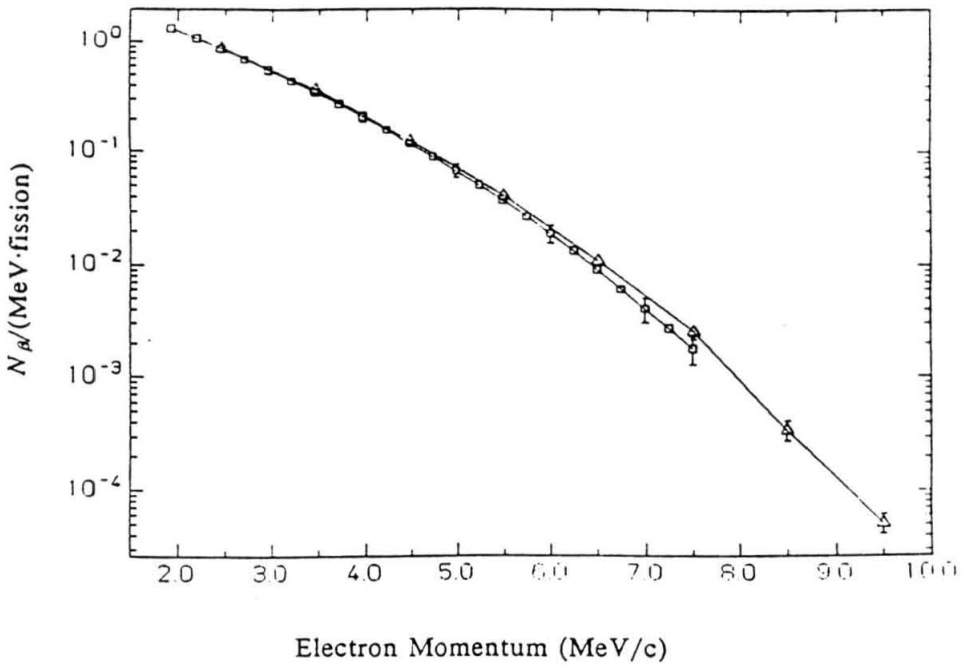

Fig. 51. Calculated β spectra from the fission products of ^{252}Cf. □ - Vogel[43], Δ - Kopeikin[33].

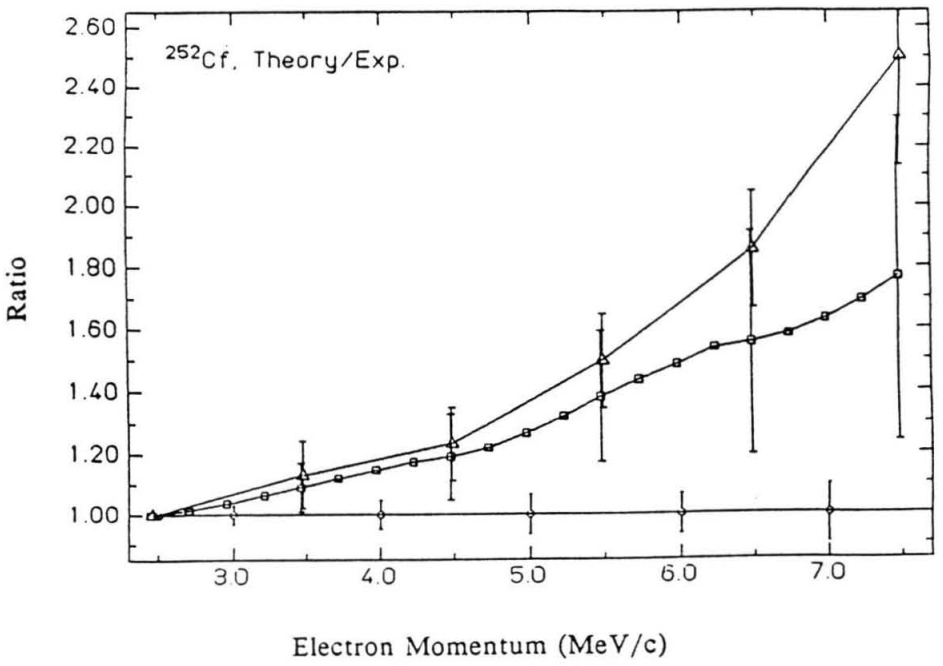

Fig. 52. Ratio of the calculations to the present experiment. □ - Vogel[43], △ - Kopeikin[33], ○ - errors in the experiment. Error bars on the calculations represent their only total errors, they do not include the experimental errors. Since we have normalized all spectra at 2.5 MeV/c, the errors on the calculations should be smaller than shown by the overall error in the normalization (claimed as 2% for Kopeikin, not given for Vogel).

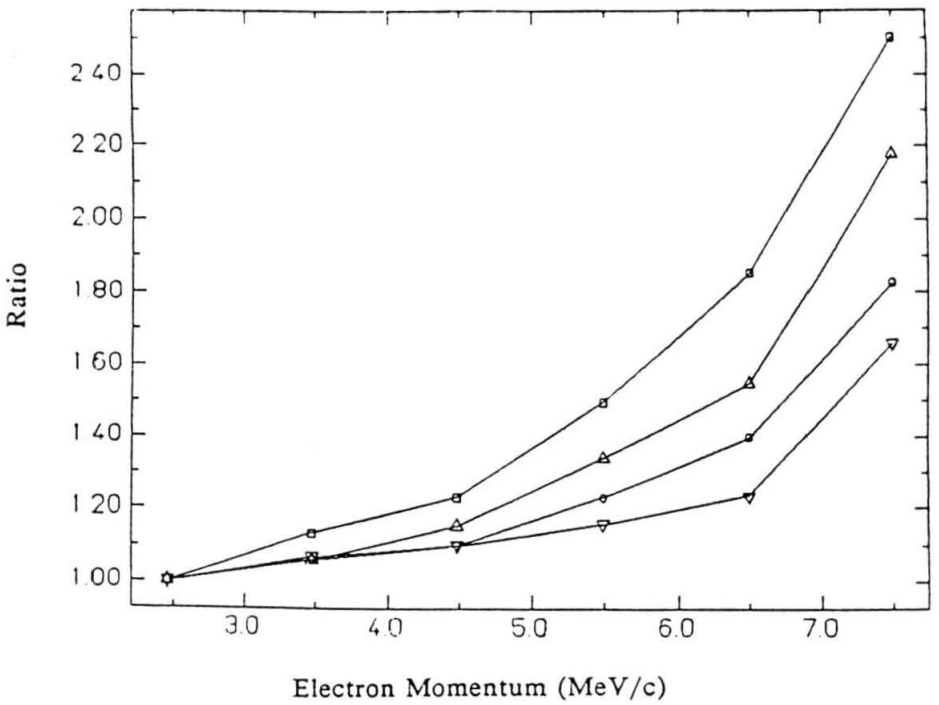

Fig. 53. Ratio of the calculations of Kopeikin[17,33] to the current experiment (□) and the experiments of Schreckenbach et al. for ^{235}U (▽)[18], ^{239}Pu (○)[28], and ^{241}Pu (△)[30]. Errors are omitted for clarity, they are 10% up to 6 MeV/c and ~20% at 7.5 MeV/c (see fig. 52).

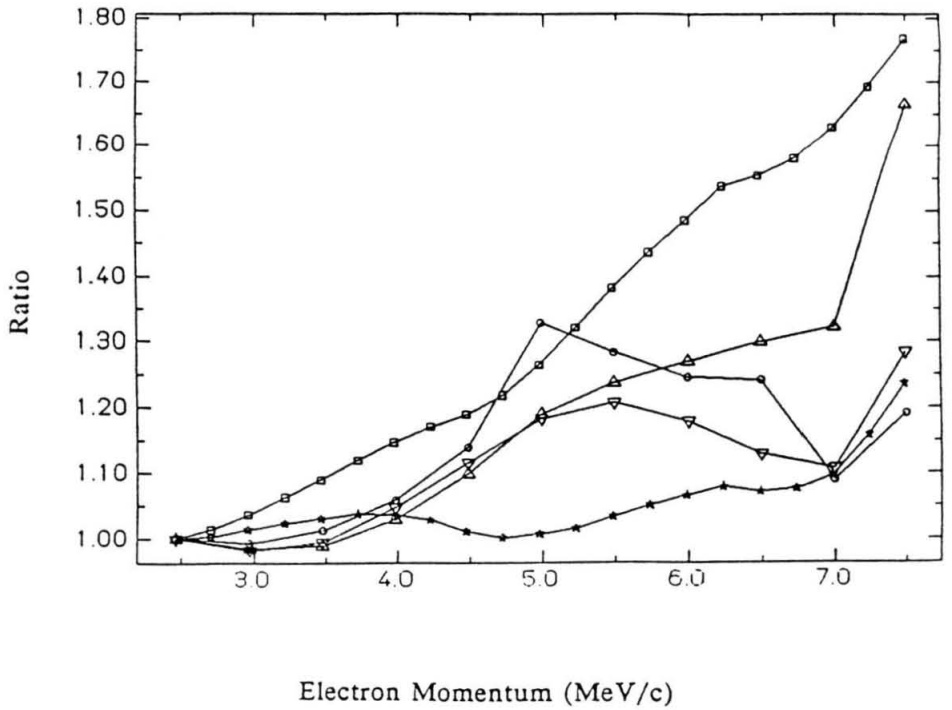

Fig. 54. Same as fig. 53 for the calculations of Vogel et al.[21,43] (for errors see fig. 52). The bottom curve (stars) is the ratio of the calculation with branching ratios altered for 5 nuclei to the experiment (see page 38-39).

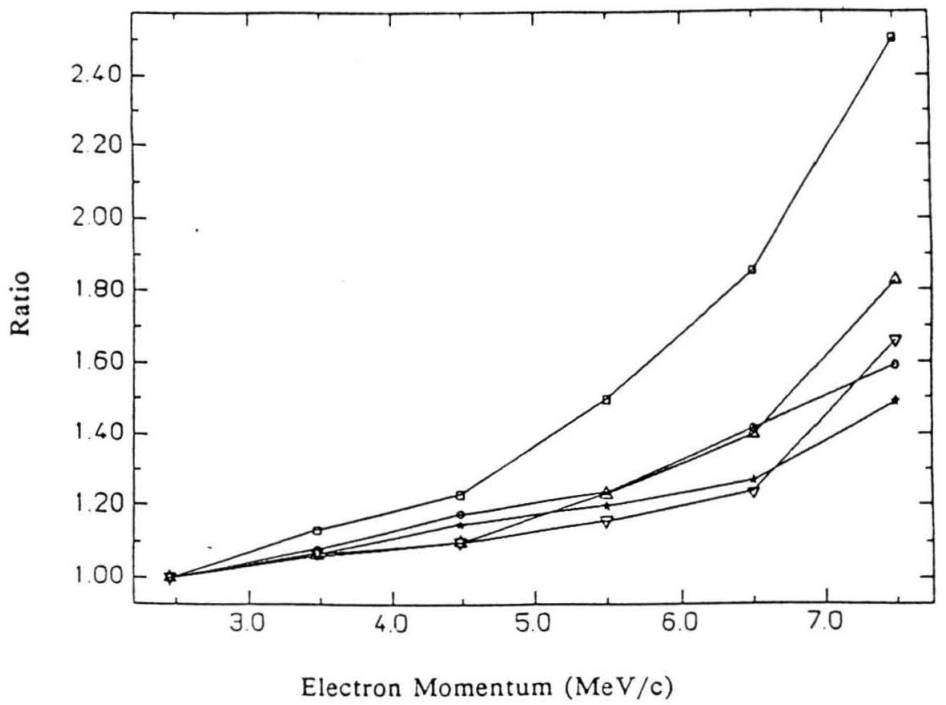

Fig. 55. Same as fig. 53 but with the ratios of the experiments of Borovoi et al.[27] on ^{235}U (stars) and ^{239}Pu (circles) to the experiments of Schreckenbach et al. added. The errors cited for the Borovoi et al. experiments are <10% up to 6.5 MeV/c and 15% at 7.5 MeV/c.

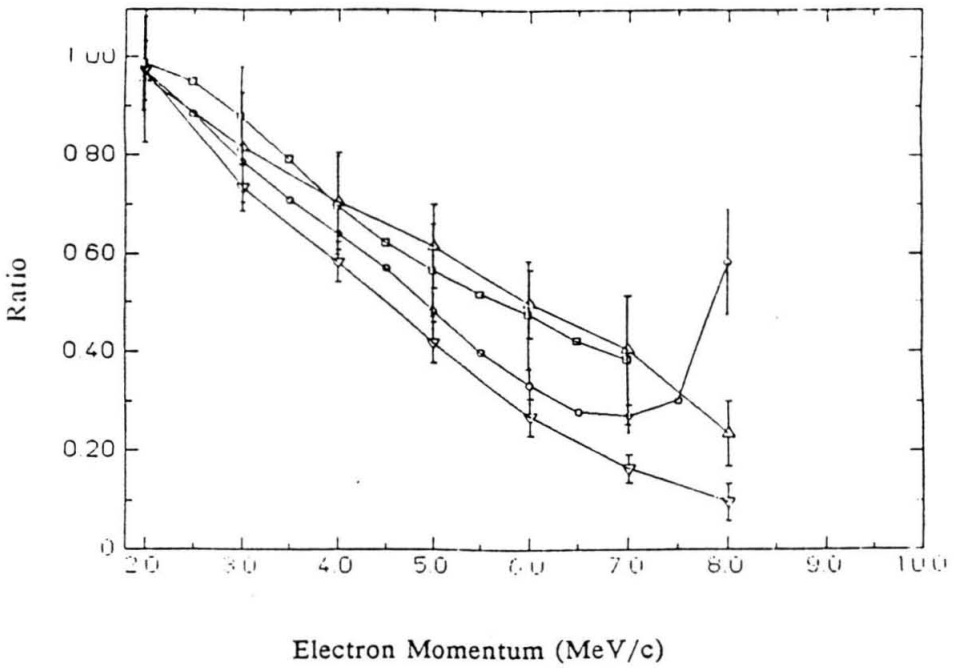

Fig. 56. Ratios of the β spectra from the fission products of ^{252}Cf to the β spectra from the fission products of ^{235}U for the various calculations and experiments. □ - Vogel, Δ - Kopeikin, ○ - ratio of the present experiment to the measurement of Schreckenbach et al., ∇ - ratio of the present experiment to the measurement of Borovoi et al.

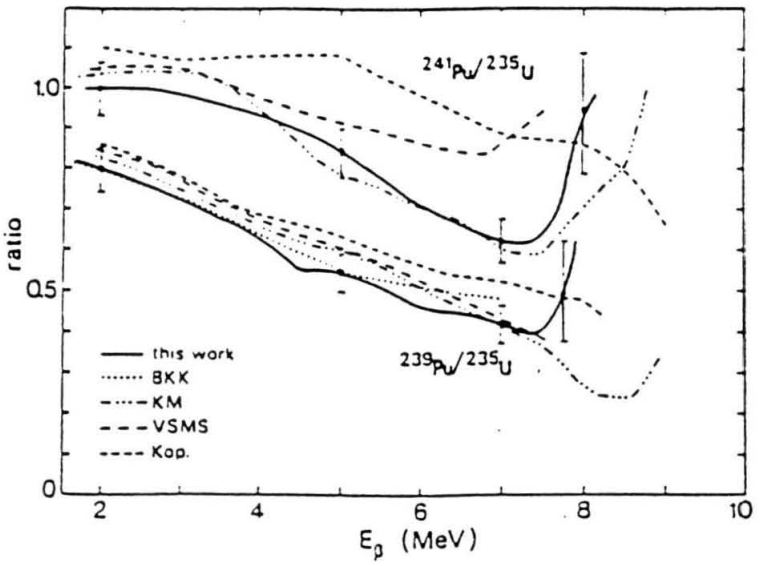

Fig. 57. Ratios of the β spectra for ^{239}Pu and ^{241}Pu to ^{235}U as in fig. 56. References for the various curves are BKK (ref. 27), KM (ref. 16), VSMS (ref. 21), Kop. (ref. 17), and the solid curves (ref. 30). (this fig. from ref. 30).

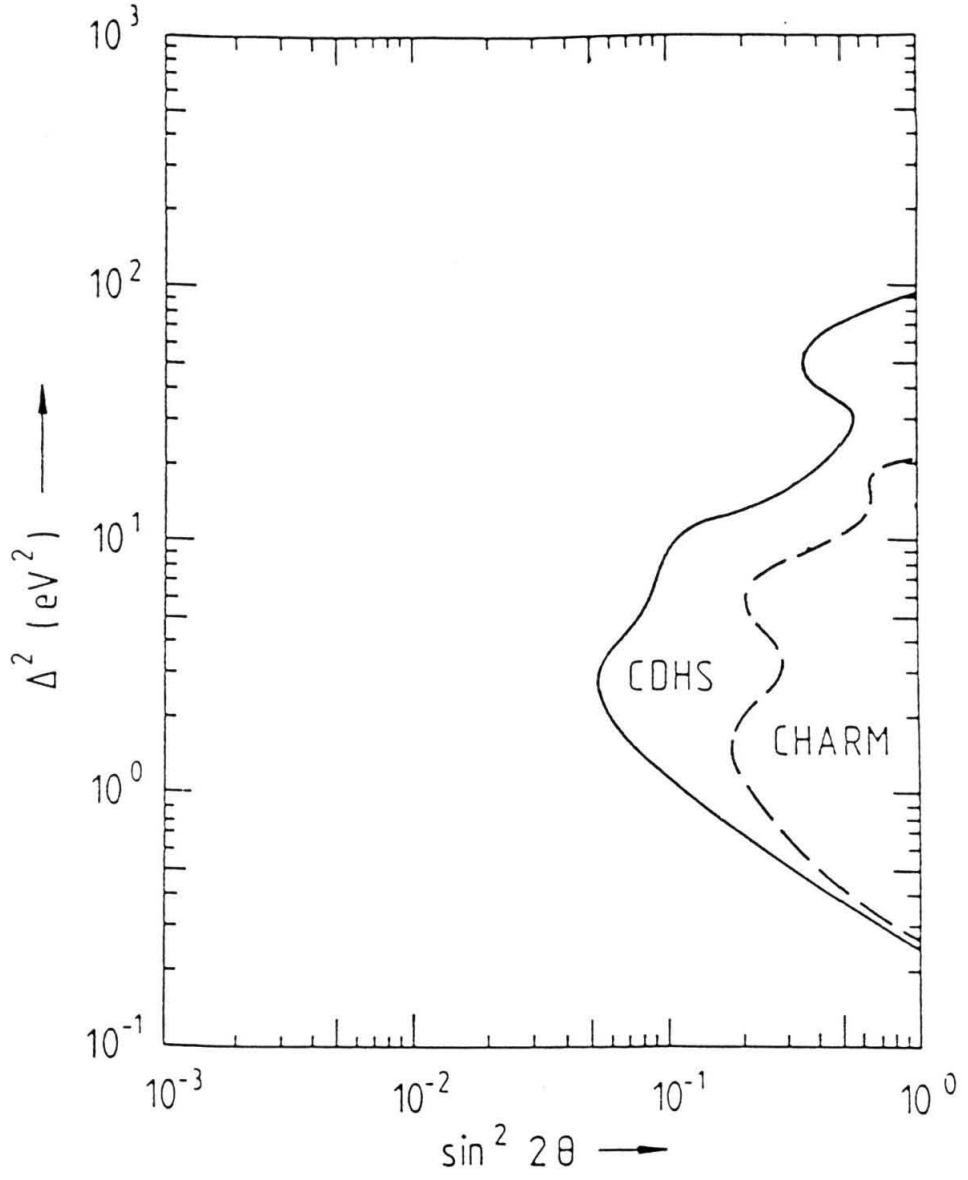

Fig. 58. Exclusion plot from the CDHS and CHARM experiments at CERN. Neutrino oscillations with parameters which lie in the region to the right of the curves are excluded.

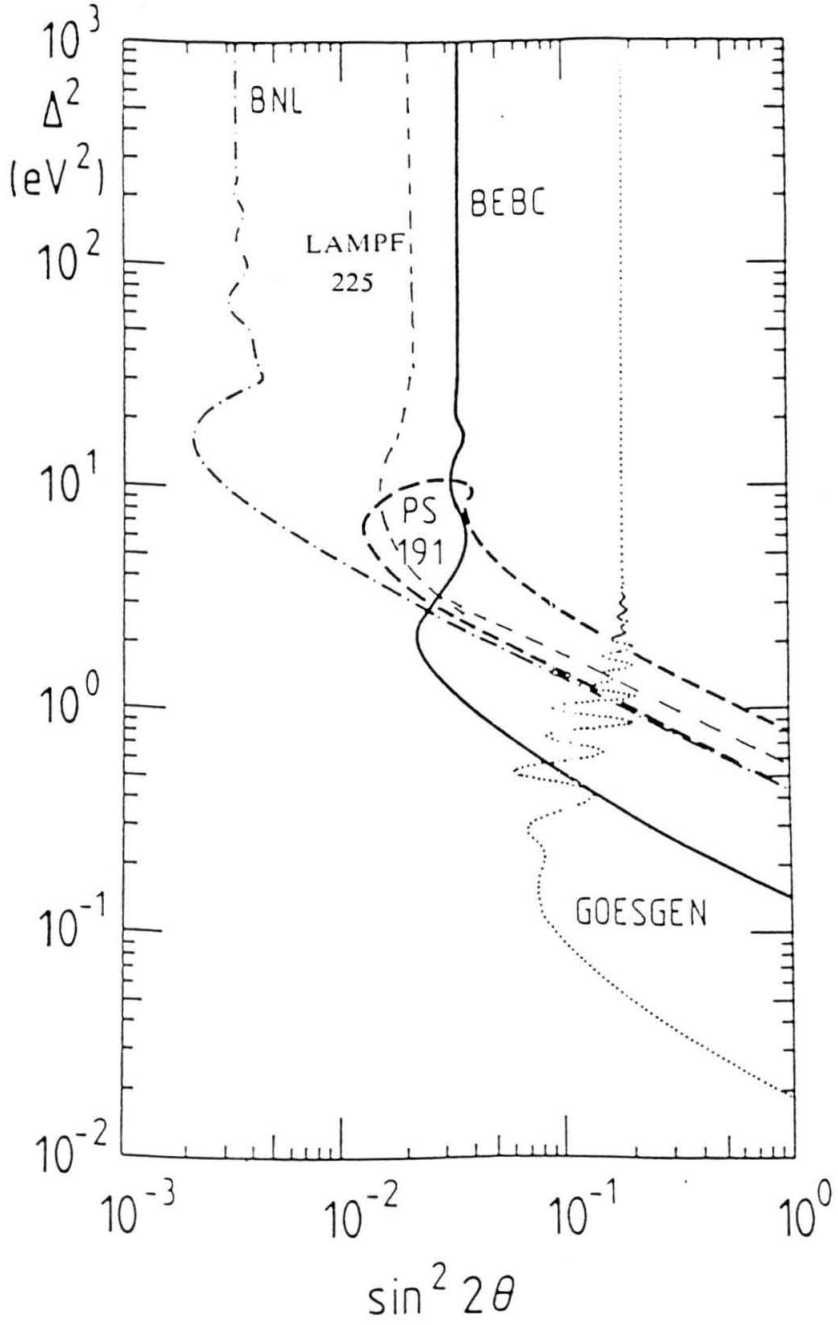

Fig. 59. Results of several neutrino oscillation experiments. PS-191 finds evidence for oscillations with parameters within the curve shown. For the other experiments oscillations are excluded for parameters above and to the right of the curves. The results of the Gösgen reactor experiment discussed in section A.3.3 are included for comparison.

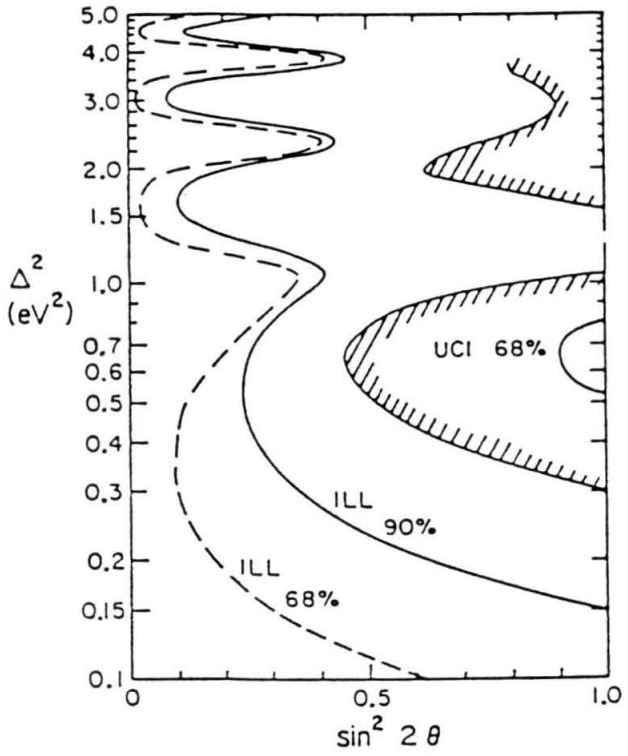

Fig. 60. Exclusion plot from the ILL reactor experiment. The region to the right and above the curves is excluded. The deuteron experiment described in section A.3.1 found evidence for oscillations with parameters within the contours labeled UCI; these clearly conflict with the other experiments. (from ref. 52).

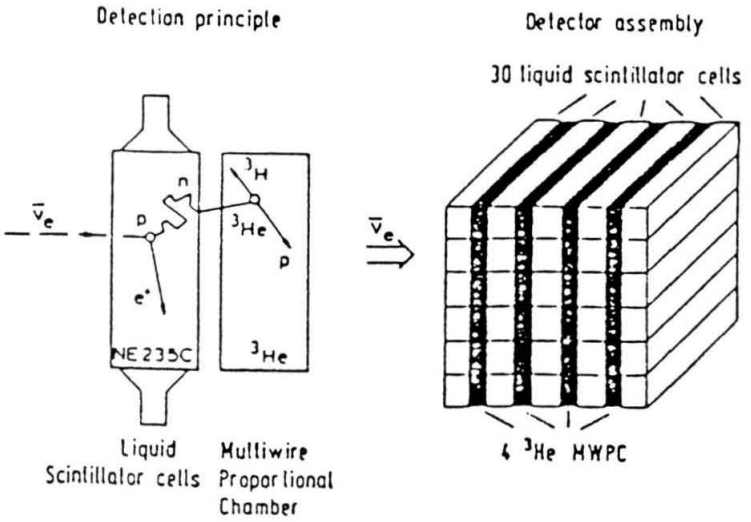

Fig. 61. Schematic of the detectors used in the Gösgen experiment. (from ref. 47)

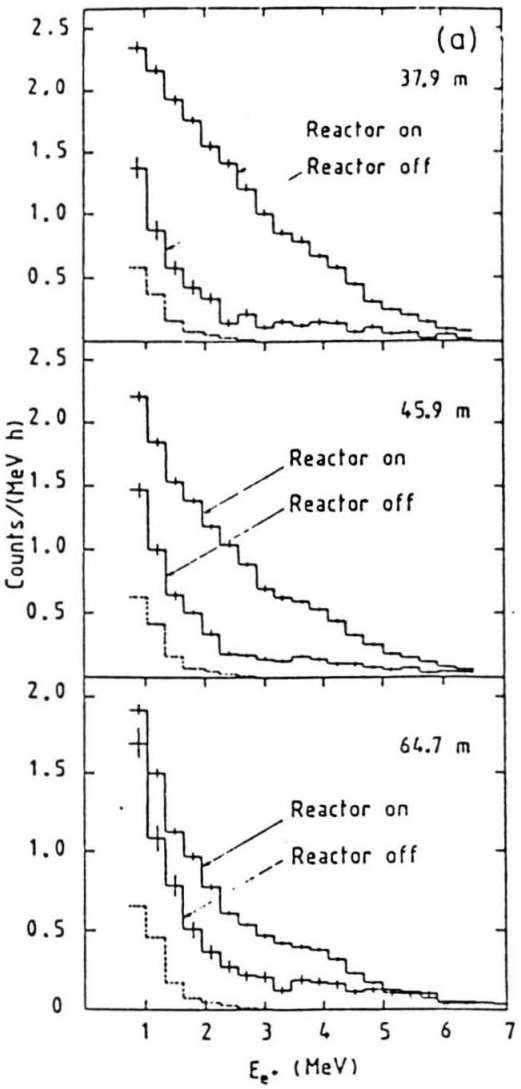

Fig. 62. Reactor On, Reactor Off, and spectrum from accidentals for the Gösgen experiment. (from ref. 47).

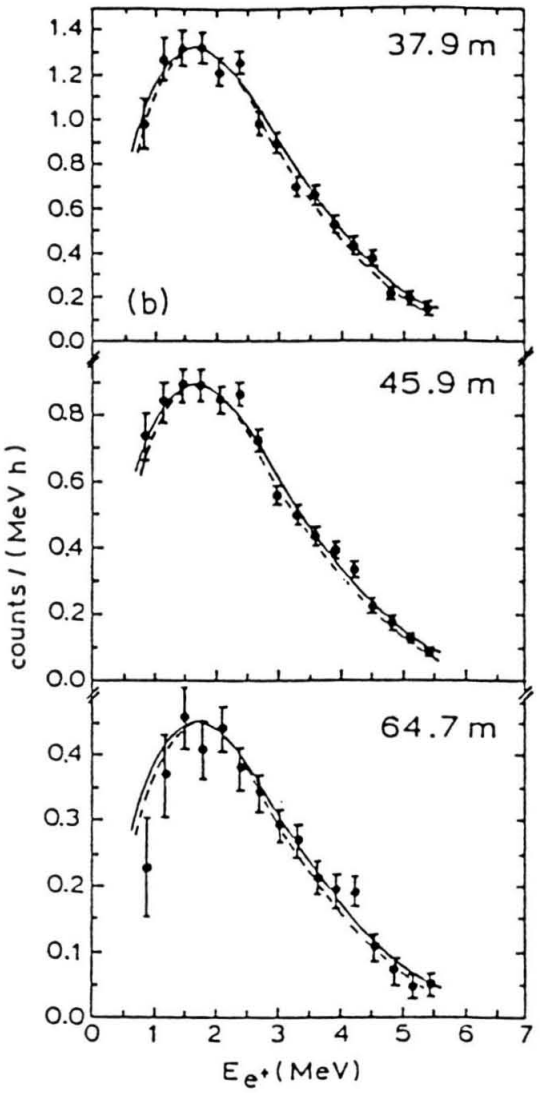

Fig. 63. Reactor On - Reactor Off spectra at three positions for the Gösgen experiment, the solid curves are the result of analysis A, the dotted curves of analysis B, clearly no evidence is seen for oscillations. (from ref. 47).

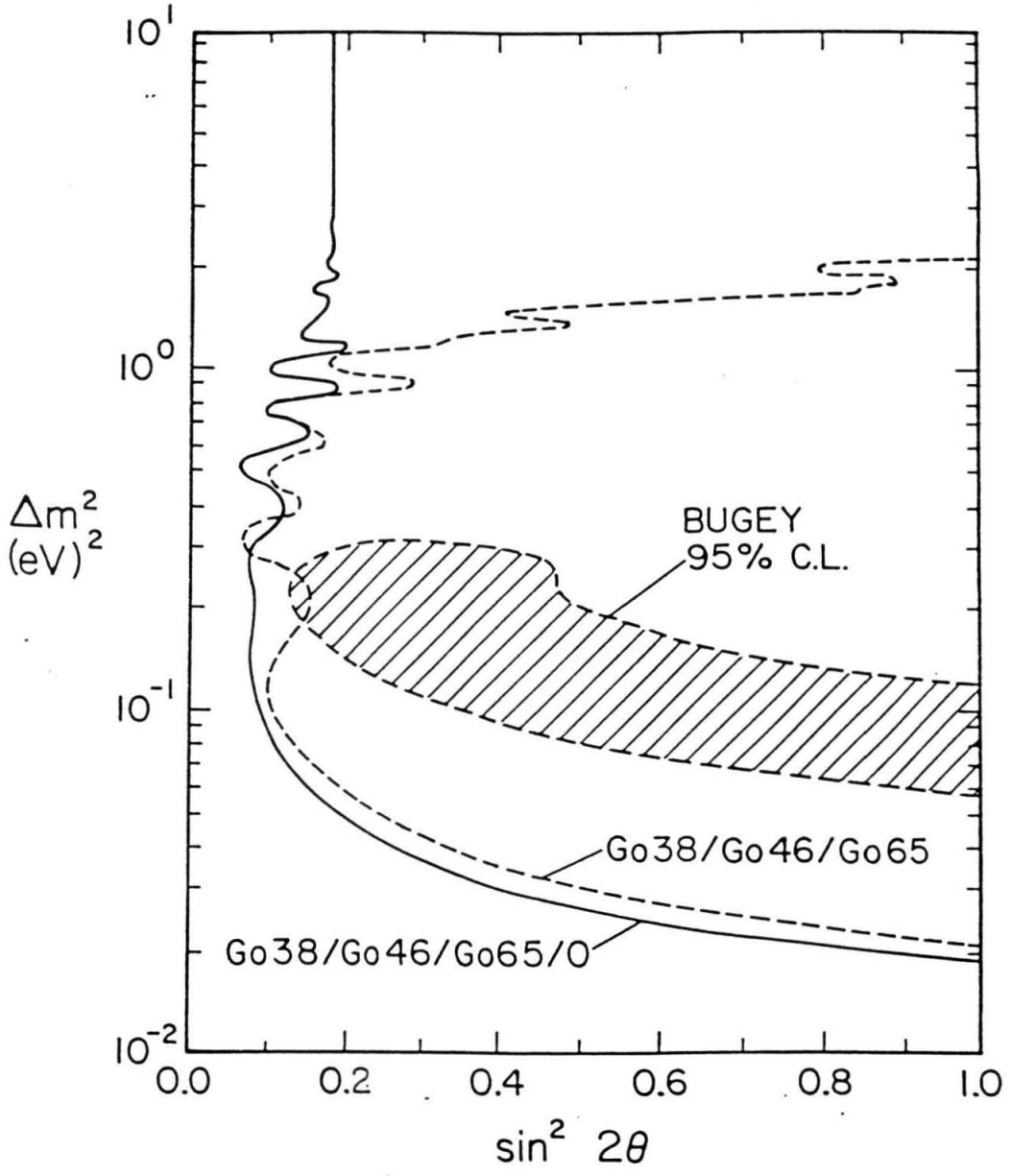

Fig. 64. Results of the Gösgen and Bugey experiments. The Gösgen experiment excludes oscillations with parameters above and to the right of the curves. The dotted line is from analysis A (no assumptions about the $\overline{\nu}_e$ spectrum from the reactor); the solid line from analysis B (reactor $\overline{\nu}_e$ spectrum assumed). The Bugey experiment finds evidence for oscillations with parameters within the shaded region.

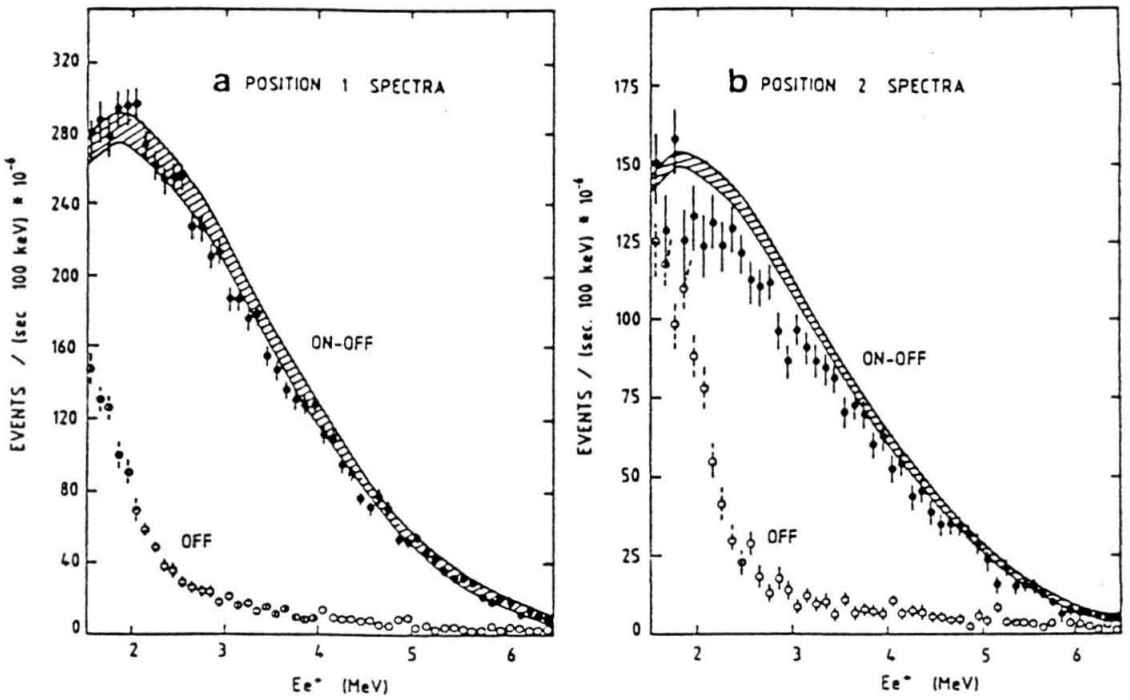

Fig. 65. Reactor On - Reactor Off spectra from 2 positions for the Bugey experiment. The shaded areas represent the expected spectra. The deviations at position 2 are interpreted as evidence for neutrino oscillations. (from ref. 49).

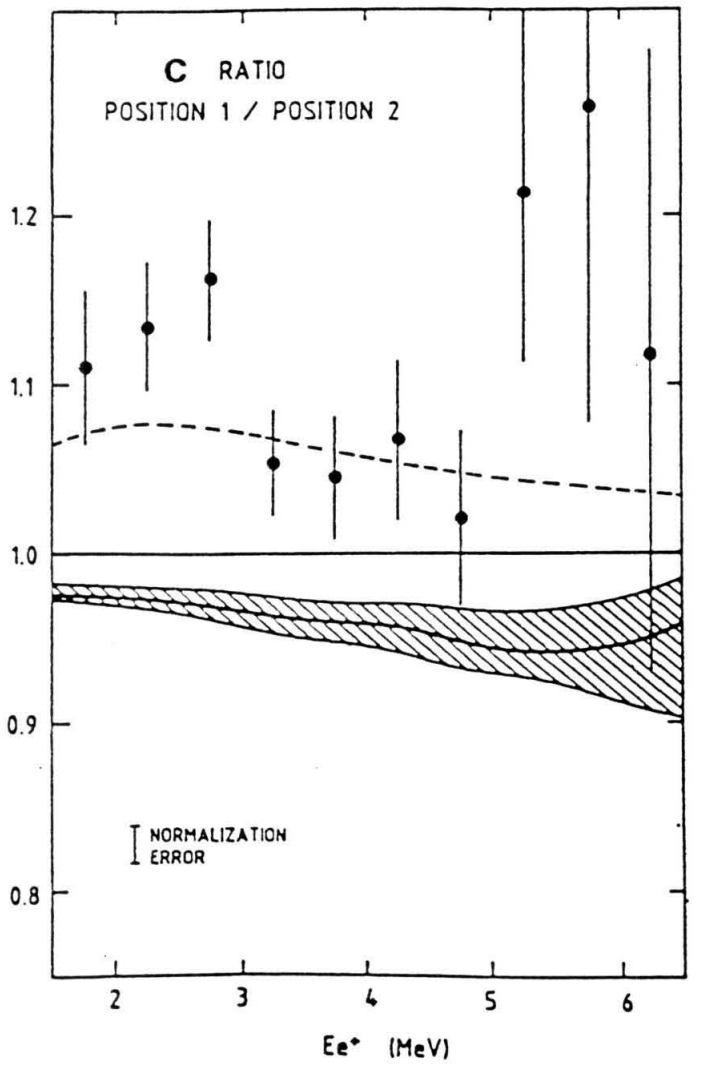

Fig. 66. Ratio of the positron spectra at position 1 and position 2 for the Bugey experiment. The shaded region is the expected result with fuel burn-up corrections; the dotted curve is the result for oscillations with parameters $\Delta m^2 = 0.2\ eV^2$, $\sin^2 2\theta = 0.25$. (from ref. 49).